공학박사학위논문

Monitoring of off-grid renewable energy systems and a load oriented model for energy production and consumption

독립 신재생 전력망의 에너지 모니터링 및 부하 고려 모델 개발

2017년 8월

서울대학교 대학원
기계항공공학부
이 장 엽

독립 신재생 전력망의 에너지 모니터링 및 부하 고려 모델 개발

Monitoring of off-grid renewable energy systems and a load oriented model for energy production and consumption

지도교수 안 성 훈

이 논문을 공학박사 학위논문으로 제출함

2017년 8월

서울대학교 대학원
기계항공공학부
이 장 엽

이장엽의 공학박사 학위논문을 인준함

2017년 8월

위 원 장 : 주 종 남

부위원장 : 안 성 훈

위 원 : 차 석 원

위 원 : 박 용 래

위 원 : Binayak Bhandari

Abstract

Demand for renewable energy sources has increased rapidly due to global warming. Since 1990, the renewable energy consumption ratio has increased among developed countries and the OECD average reached over 10% in 2015. Even in developing countries, an off-grid renewable power system has been implemented in rural areas to provide electricity. However, the power generation characteristics of renewable energy sources are so random that power outages occur frequently.

In this research, an off-grid monitoring platform was developed and applied to an off-grid renewable energy system to overcome the instability of a renewable power system in rural areas. Our monitoring platform contains a customized real-time operating system with low-cost hardware for task management. The monitoring platform was capable of bidirectionally transmitting a data set via short message service or the internet. The transmitted data set was uploaded to a cloud system so that the off-grid system could be monitored with any platform.

The energy consumption of manufacturing systems and

renewable energy systems were modeled, and the operating conditions were simulated. The simulation results provided 1) the design guide for an off-grid system, 2) the failure rate with various scales of off-grid systems, and 3) the calculation method of operation times. Furthermore, the modeling method could be applied to various types of electric load conditions.

Finally, an off-grid test bed was installed with our developed monitoring platform and four case studies were conducted: 1) a three dimensional printer, 2) a turning machine, 3) a band saw, and 4) a vaccine carrier, to verify the stability of the off-grid energy system with manufacturing processes. Comparison with previous research was also conducted, and the proposed simulation method provided a smaller scale of off-grid systems with stable operation.

Key words: renewable energy, energy consumption, modeling, monitoring, off-grid

Student Number: 2012-20692

Table of Contents

List of Tables

Table of Figures

1 Introduction

1.1 Overview

Since the industrial revolution, the amount of CO_2 emissions worldwide has increased dramatically. Consequently, global warming is now a problem, due to greenhouse gases generated by fossil-fuel energy generation systems. Since 1970, the global mean temperature has increased gradually and CO_2 emissions have accelerated the effects of global warming [1]. As one effort to slow down global warming, the PBL Netherlands Environmental Assessment Agency's 2016 report was published [2]. There are two major solutions to the global warming problem: 1) energy consumption and 2) energy generation.

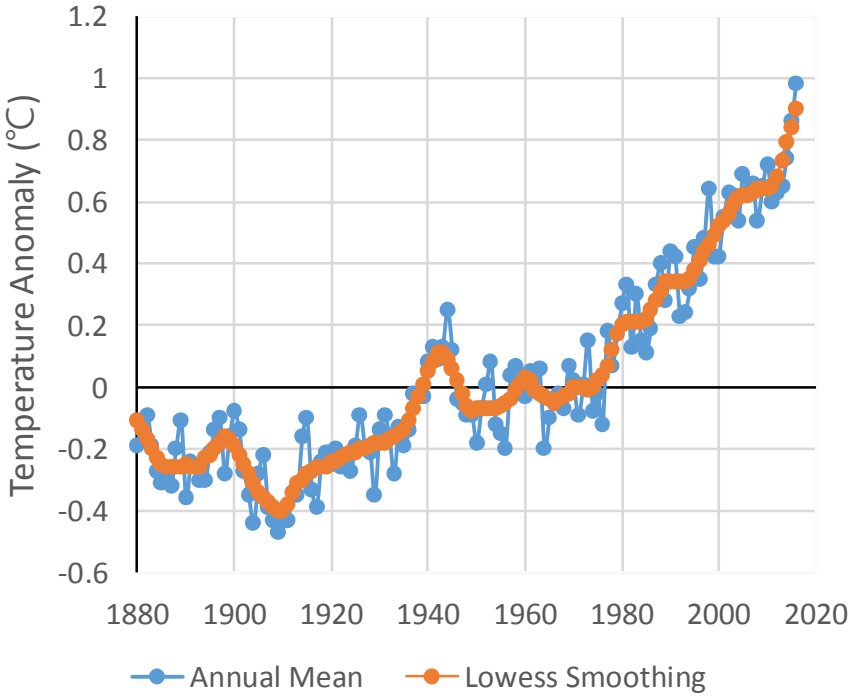

Figure 1. Global mean estimates based on land and ocean data [1]

The International Organization for Standardization (ISO) published the ISO 50001:2011 Energy management system for managing energy consumption [3] (Figure 2). ISO also published another standard, the ISO 14955 series for increasing energy consumption efficiency in manufacturing industries [4].

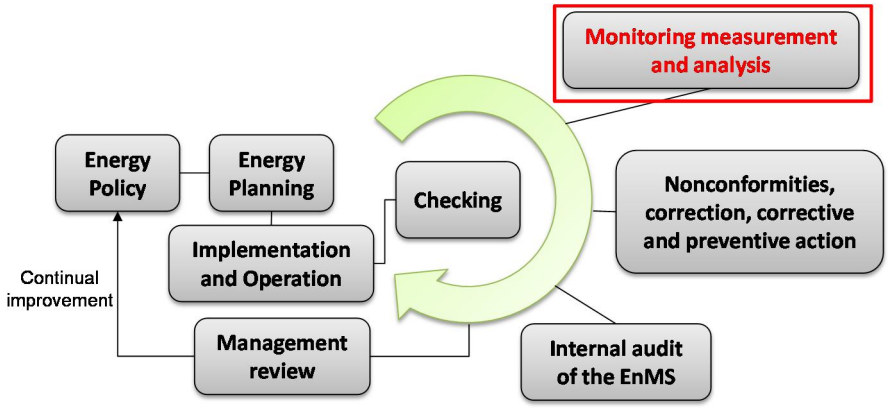

Figure 2. Energy management system model (ISO 50001) [3]

At Stanford University, the Global Climate & Energy Project (GCEP) was initiated [5]. Main research topics of the GCEP are focused on CO_2 emissions, energy generation, and storage from renewable energy sources (Figure 3).

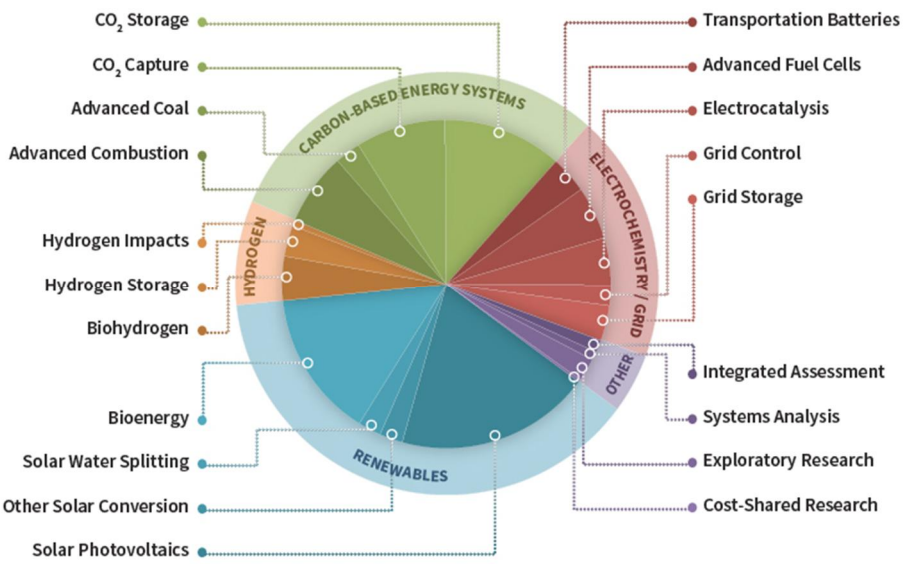

Figure 3. Cumulative research areas in the Global Climate & Energy Project (GCEP; image generated from Ref. [5])

As a result of these efforts, renewable energy consumption as a percentage of total energy consumption has increased (Figure 5) and the trends of CO_2 emission have decreased gradually [2]. As shown in Figure 5, global trends in energy consumption are headed to the replacement of conventional energy sources with renewable energy sources. In South Korea, the energy usage ratio has increased rapidly from 48.1% in 1990 to 63.8% in 2014 [6]. Renewable energy consumption as a percentage of total energy consumption has increased gradually since 1990. Regarding the OECD average, the ratio of energy consumption with renewable energy increased from 7%

to 11% from 1990 to 2016 [7].

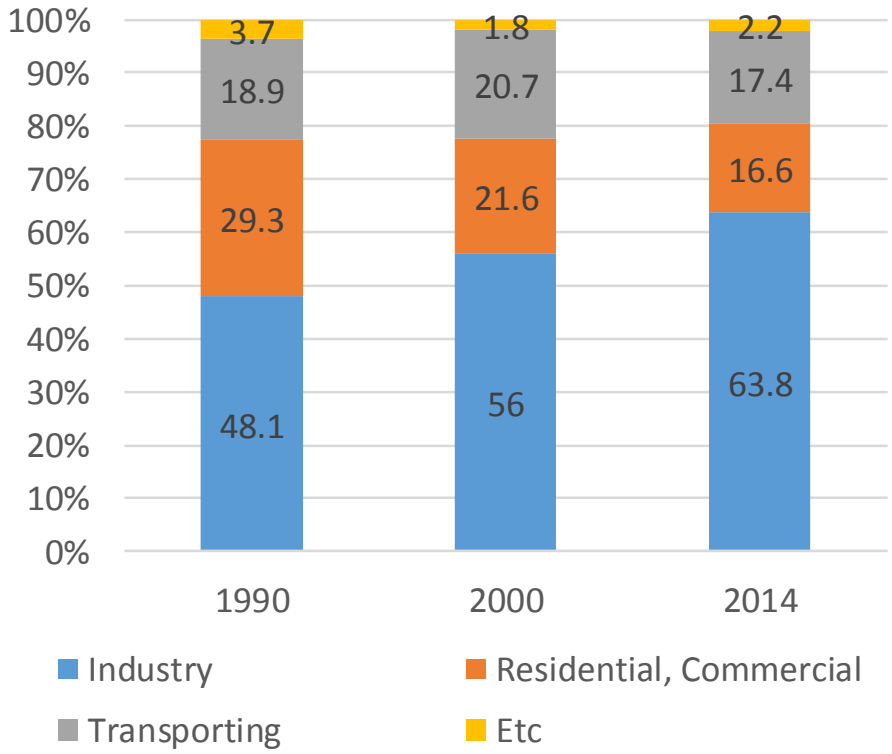

Figure 4. Energy consumption ratio in South Korea [6]

For developed countries, electricity energy can boost their gross domestic product (GDP) regarding primary energy supply versus GDP trends[8]. Binayak Bhandari *et al.* investigated the socio-economic impact of renewable energy-based power systems in small villages [9]. A survey was conducted among villages in mountainous areas. An off-grid power system is required because villages in mountainous areas are far from the

main grid and the cost of installing a system tied to the main grid is extremely high. Nepal Solar Corps have visited Nepal since 2011 and several off-grid renewable energy systems were installed. A photovoltaic (PV)-wind hybrid system (PV 5 kW and wind 3 kW) and a micro-hydro power (MHP) plant were introduced in the mountainous villages of Thingan and Kolkhop, respectively. These two systems are grid-tied [10]. Even in small villages with micro power systems, net income was increased and an education impact was expected with an improved environment for students [9].

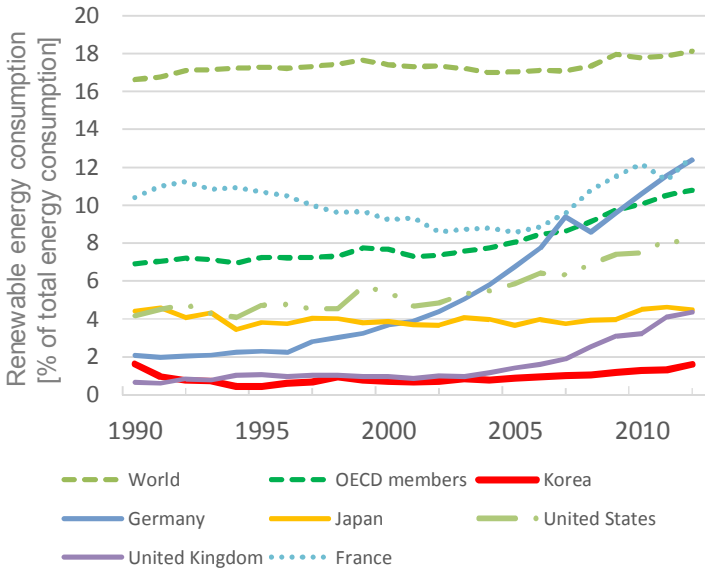

Figure 5. Renewable energy consumption ratio [7]
(% of total energy consumption)

Demand for renewable energy systems is increasing rapidly worldwide. Renewable energy is a major solution for global

warming and for addressing poverty in developing countries. Ongoing research has focused primarily on renewable energy generation rather than monitoring in rural areas as well as system designs with industrial perspectives. In this research, a remote monitoring control system was developed and installed in a rural area. Data were transmitted from foreign rural areas to South Korea and gathered into a web-based database and cloud service. Additionally, manufacturing energy consumption was modeled and stability of an off-grid renewable energy system was established. A manufacturing-oriented renewable energy system simulation was developed and a manufacturing-oriented design for a renewable energy plant was provided.

1.2 Stability issues in renewable energy systems

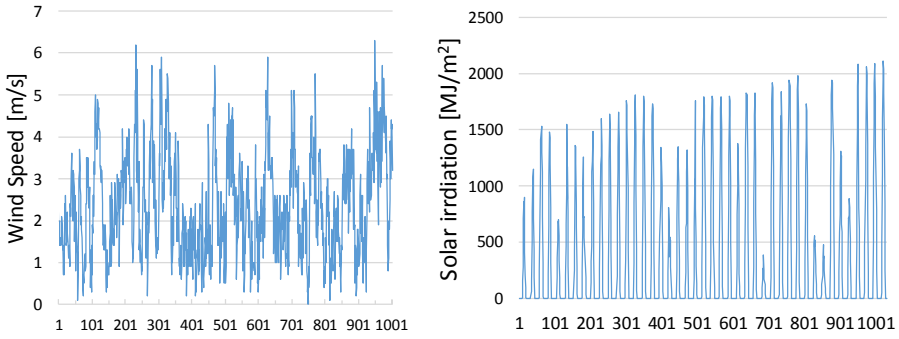

Figure 6. Typical pattern of renewable resources [11]

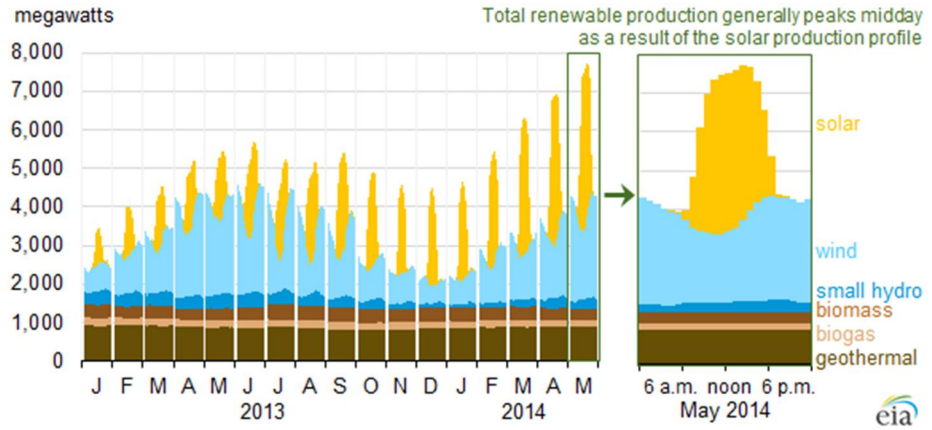

Figure 7. Hourly California renewable electricity production profile by month (image from [12])

Renewable energy systems have stability issues regarding random incoming energy sources (e.g., sunrays, wind). Especially from a manufacturing perspective, unstable energy sources can cause crucial damage to manufactured parts even in the manufacturing facility itself. Thus, renewable energy systems do not fit well with manufacturing systems. Rajab *et al.* proposed a planning and operation scheduling method for a PV–battery system [13]. Rajab's results suggested that the reliability of a renewable energy system exhibits a relationship between PV size and energy storage size. Conventional load conditions, such as residential and hospital electricity demands, are random so a statistical method was implemented to manage the reliability of a renewable energy system.

1.3 Stability issues and manufacturing processes

Manufacturing processes consume large amounts of energy, typically with high stability. As demand for renewable energy sources have increased dramatically, stability issues have also increased.

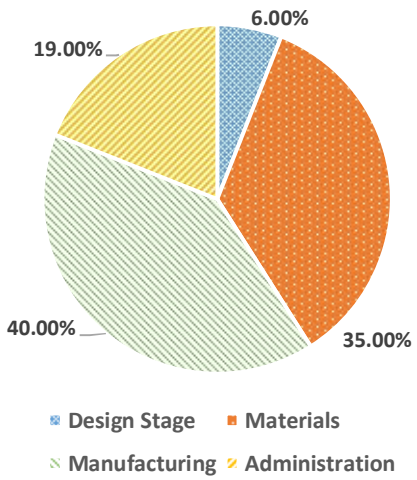

Figure 8. Product costs for manufacturing

Manufacturing costs for products are shown in Figure 8. Material costs for manufacturing were 35% and manufacturing costs were 40%. When manufacturing, the facility process may be aborted in uncertain situations, and up to 75% of costs may be wasted. Even though facility maintenance costs are not included, wasted costs are significantly high, such that stability in manufacturing systems is crucial.

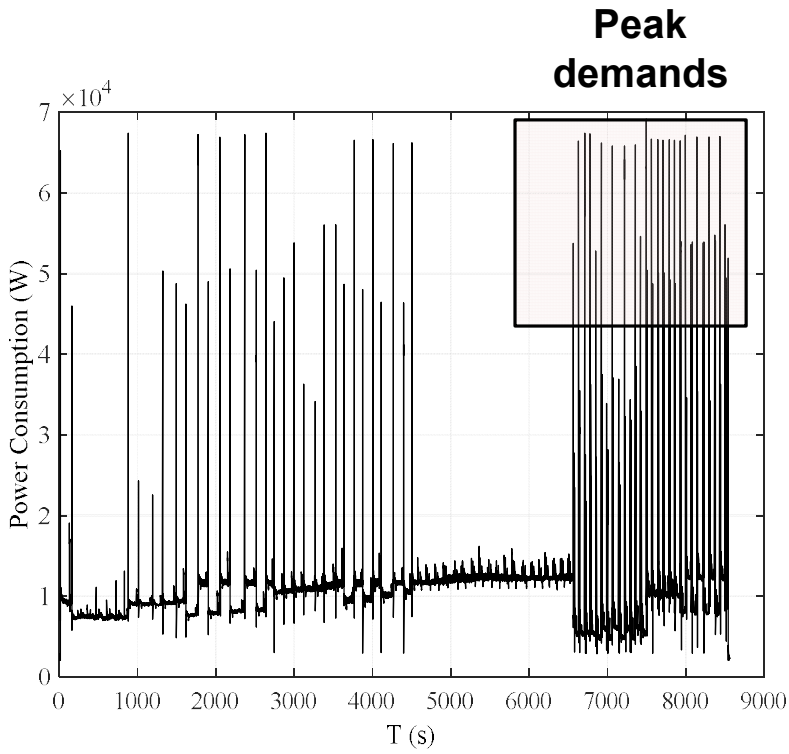

Figure 9. Power demand for manufacturing (GS400)

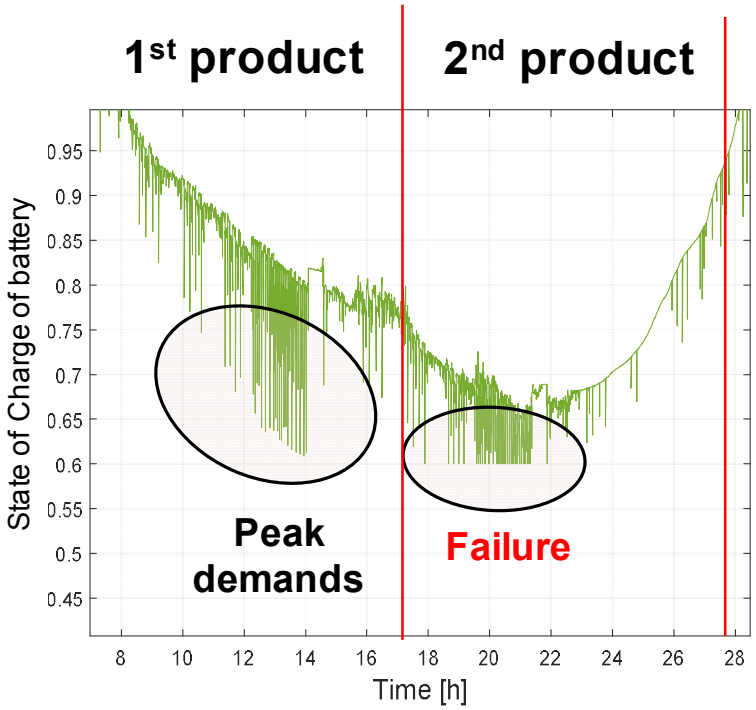

Figure 10. Failure example of manufacturing process with off-grid energy system (GS400)

There are significantly different trends between accommodation and industrial uses. Power demands for a manufacturing facility, lathe, and GS400 are shown in Figure 9. Peak demands are crucial from the point of view of stability in the system. Peak demand is caused by high acceleration in high-inertia mechanical parts, such as spindles or rapid feeds. As shown in Figure 10, peak demand can cause partial failure even if the whole system seems stable in a stationary state.

2 Renewable energy production model

Several researchers have used the Hybrid Optimization of Multiple Energy Resources (HOMER) to optimize the size of a renewable energy plant [14]. Lal *et al.* optimized a hydro mini-grid system with HOMER [15]. Chong *et al.* calculated the appropriate scale of an autonomous hybrid wind/photovoltaic (PV)/battery power system for a household [16]. There are also 68 tools for analyzing renewable energy systems [17].

2.1 PV energy production

PV is the primary source of energy generation in off-grid systems. A PV array can be used with a grid-tied inverter (GTI) with a main grid [10]. However, most off-grid cases require battery banks [13, 18-26].

2.1.1 Mathematical models and patterns of energy production

There are three major types of PV model for estimating PV potential [27-31]. An ideal single-diode PV cell model was derived from the theory of semiconductors and this model has

been widely used for simulating PV potentials [32].

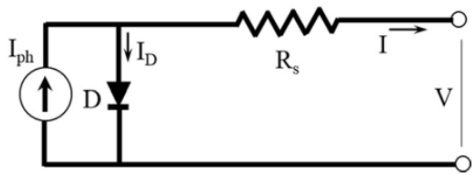

Figure 11. Ideal single-diode photovoltaic (PV) cell model [32]

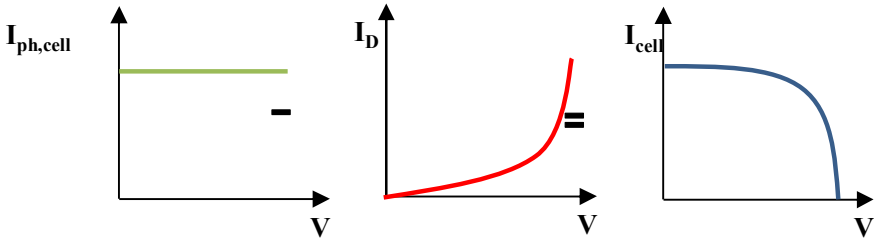

Figure 12. Brief expression of an ideal single-diode PV cell model

$$I = I_{ph,\text{cell}} - I_{0,\text{cell}}\left[\exp\left(\frac{qV}{akT}\right) - 1\right]$$

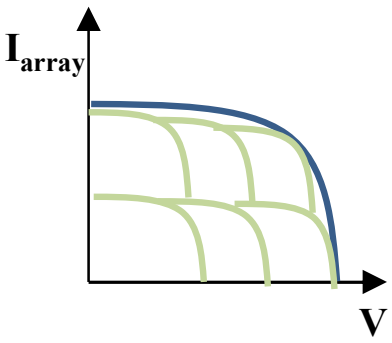

Figure 13. PV array model consists of multiple single-diode models

$$I = I_{ph} - I_0\left[\exp\left(\frac{V + R_s I}{V_t a}\right) - 1\right] - \frac{V + R_s I}{R_{sh} a}$$

$I_{ph,cell}$ and $I_{0,cell}$ are the PV and saturation current of cell and I_{ph} and I_0 represent the array of PV. q is the electron charge (1.60218×10^{-19} C), V is the potential of the PV, a is the diode ideality constant, k is the Boltzmann constant (1.38065×10^{-23} J/K), and T is the temperature of the cell.

A PV array model is obtained with the ideal single-diode PV cell model equation. In this research, the PV array model is an implicit equation and the Newton- Raphson method was used to obtain the I-V curve for the target system. Error tolerance was defined as 0.001 and range of voltage is larger than 0 V, $I = I_{sc}$ condition, to V_{oc}, $I = 0$.

$$f(V, I) = -I + I_{ph} - I_0\left[\exp\left(\frac{V + R_s I}{V_t a}\right) - 1\right] - \frac{V + R_s I}{R_{sh} a} = 0$$

$$\frac{\delta f}{\delta I} = -1 - I_0 \frac{R_s}{V_t a}\exp\left(\frac{V + R_s I}{V_t a}\right) - \frac{R_s}{R_{sh}} = 0$$

$$I_{n+1} = I_n - \frac{f(V, I_n)}{\frac{\delta f(V, I_n)}{\delta I}}, 0 < V < V_{oc}\text{ , Newton} - \text{Raphson Method}$$

Simulation conditions were defined with specification of the

target PV panel, SSP-120D, and I-V curve. Figure 14 was obtained from the proposed model and power performance and maximum power were obtained as shown in Figure 15.

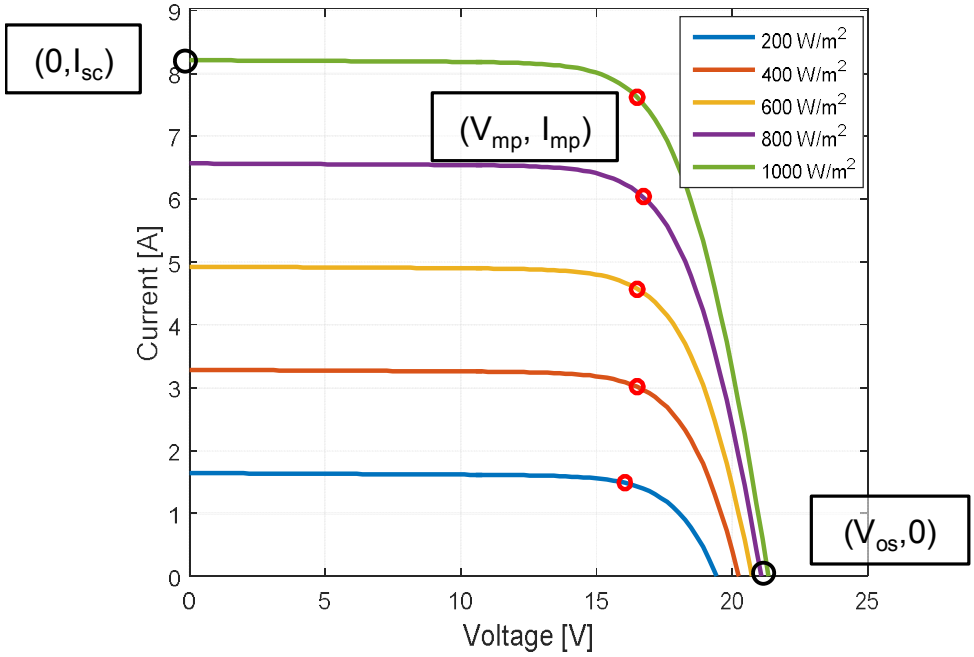

Figure 14. Typical I−V curve for an array of PVs

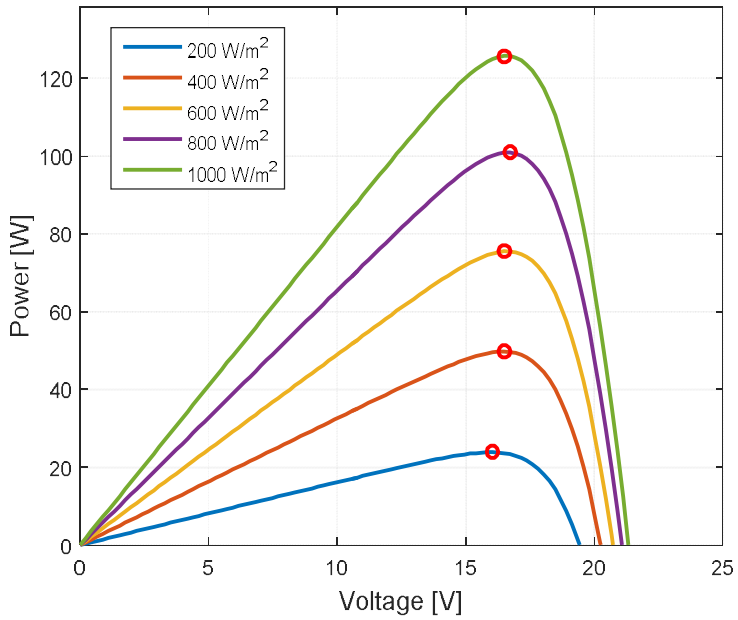

Figure 15. Typical power curve for an array of PVs

To verify the modeling results, the maximum power of the PV was measured with the conditions indicated in Table 1. The measured solar irradiation value and current were 307.6 W/m^2 and 6.51 A, respectively. The rated current was 6.89 A and the three solar panels are in series, so that the rated current is equal to 20.67 A. The PV current is proportional to solar irradiation so that the estimated current is equal to 6.36 A.

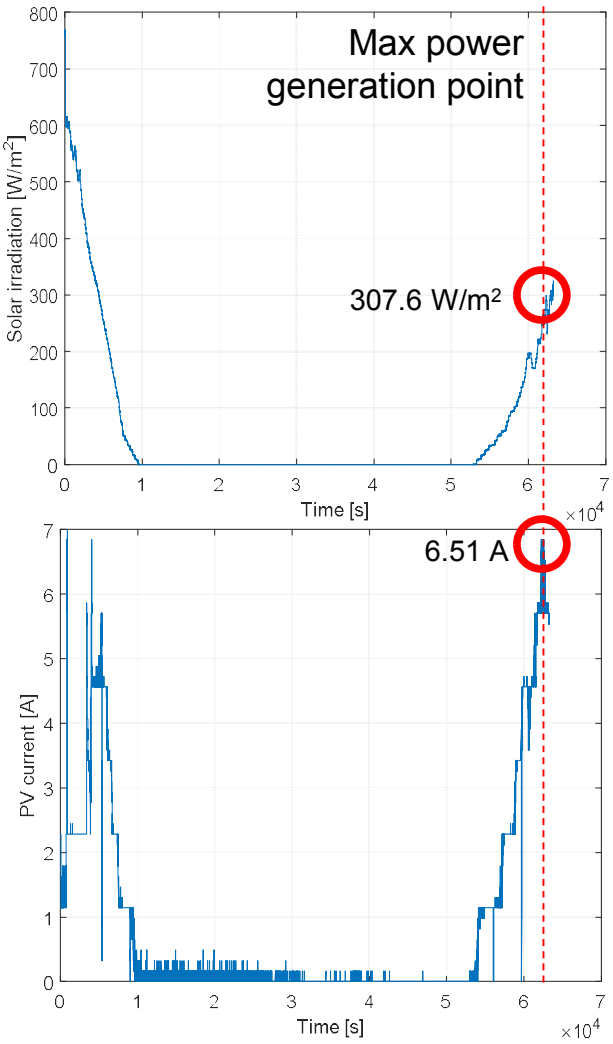

Figure 16. Experimental result of PV model verification

Table 1. Verification parameters of the PV array

Model	*SSP-120D*
Rated power	*120 W*
Short circuit current	*7.63 A*
Open circuit voltage	*21.75 V*

Rated current (@ 1,000 m/W²)	*6.89 A*
Rated voltage	*17.4 V*
Crystalline	*Multi*
Size	*1484 × 669 × 35 mm*
Install configuration	*2 in series, 3 in parallel*
Charge controller algorithm	*Maximum Power Point tracking*
Battery charging voltage	*24 V*

2.2 Wind energy production

Another energy source for renewable energy plants is wind. Wind turbines are used to generate energy from wind and several studies have investigated wind turbine models [33–37].

2.2.1 Mathematical models and patterns of energy production

The governing equation for the power of a wind turbine is given as follows:

$$P_w = \frac{1}{2} C_p(\lambda, \beta) \rho A V^3$$

$$C_p(\lambda, \beta) = C_1 \left(\frac{C_2}{\lambda_i} - C_3 \beta - C_4 \right) e^{-\frac{C_5}{\lambda_i}} + C_6 \lambda$$

$$\frac{1}{\lambda_i} = \frac{1}{\lambda + 0.08\beta} - \frac{0.035}{\beta^3 + 1}$$

$$\lambda = \frac{R\omega}{V}$$

P_w is the power generated from the wind turbine (W), C_{PU} is the power coefficient, A is the intercepting area of the rotor blades (m^2), V is the average wind speed (m/s), and λ is the tip speed ratio. Coefficients of C_p were obtained from experimental data [34, 38]. A typical power curve for a wind turbine is shown in Figure 17.

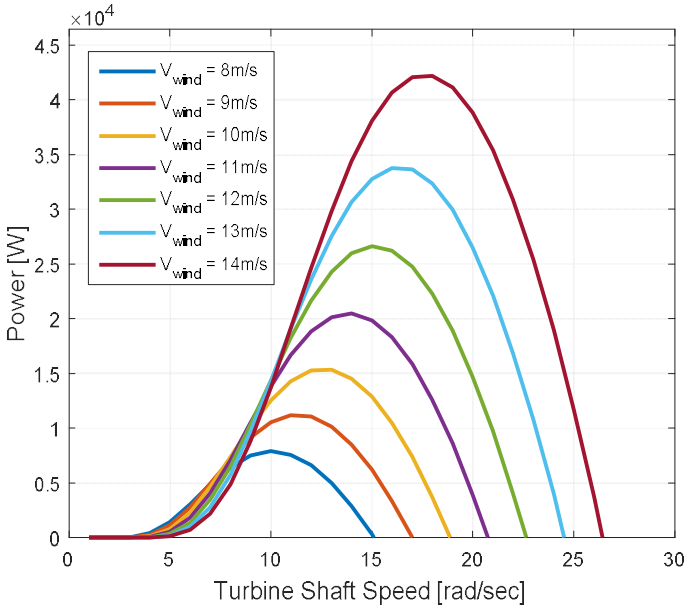

Figure 17. Typical power curve for a wind turbine

The *cut−in speed*, v_C, and the *cut−out speed*, v_F, of the wind are important parameters for a wind turbine as shown below:

$$P_w(v) = \begin{cases} \dfrac{v^k - v_C^k}{v_R^k - v_C^k} P_R, & v_C < v < v_R \\ P_R, & v_R < v < v_F \\ 0, & v \le v_C \text{ and } v \ge v_F \end{cases}$$

This model is used for the practical application of estimating the power generated by a wind turbine and a second−order polynomial is used for estimating the rating power of the wind turbine with a rating in wind speed, v_R [39]. The power output of a 400−W wind turbine versus instantaneous wind speed can be estimated as shown in Figure 18 [40].

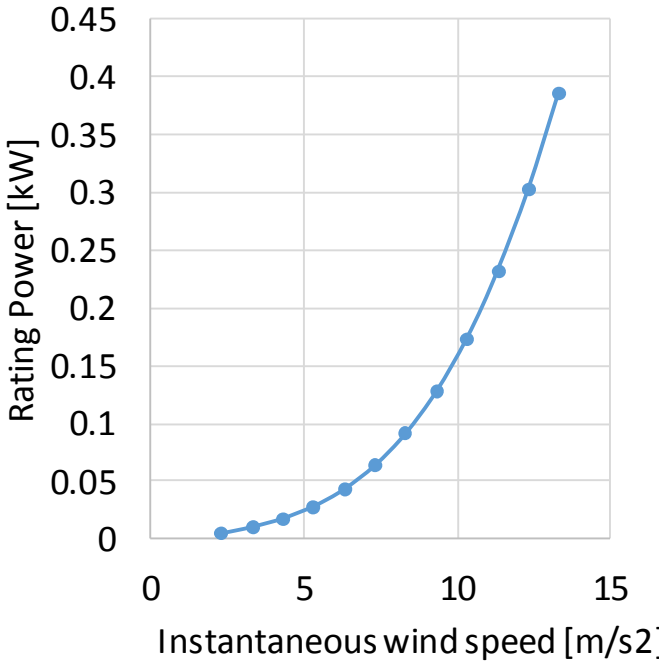

Figure 18. Power output versus instantaneous wind speed of a 400-W wind turbine [40]

2.3 Battery model

A battery is a major component of off-grid renewable energy systems. Renewable energy sources are so random that renewable power plants are eventually overdesigned. To minimize the instability of renewable energy systems, a set of batteries was installed with PV arrays and wind turbines.

In this research, a manufacturing-oriented off-grid renewable energy system requires much higher stability so a battery model is much more important than in 'conventional' research.

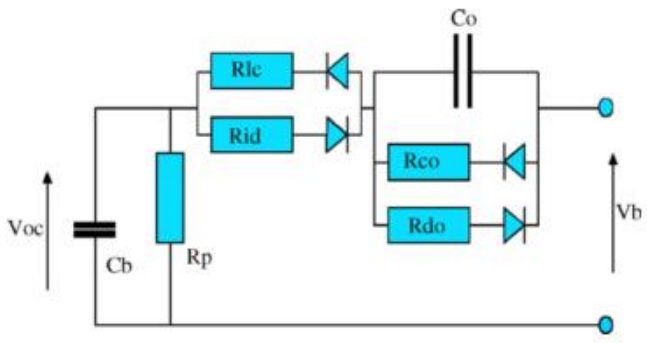

Figure 19. Equivalent battery model [41]

There are different types of lead-acid battery models [41-46]. In this research, the state of charge (SOC) model was used for estimating battery state. The governing equations for

SOC involve integrating current flow through the battery and integrating current to charge. The maximum SOC is limited by the capabilities of the battery. Furthermore, there are internal resistances calculated by the SOC so that when the SOC is low, internal resistance is high, and the external voltage is low spontaneously.

$$R_b = \frac{R_o}{S^k}$$

$$S = 1 - \frac{\int A(t)dt}{C_{10}(T, C)}$$

$$V_b = \begin{cases} A(t) \geq 0,\ V_{oc} - A(t)(R_{lc} + R_{co}) \\ A(t) < 0, V_{oc} - A(t)(R_{ld} + R_{do}) \end{cases}$$

$$E_b = \int P_b dt = \int_{V_b = V_{oc} - A_b R_b}^{V_b = V_{low}} V_b A_b dV \text{ , where } V_{low} = \text{lower voltage boundary}$$

V_{OC} is the open circuit voltage of the battery, S is the state of charge factor (form 0, for fully discharged; up to 1 for fully charged), k is the capacity coefficient, R_0 is the resistance of the fully charged battery (Ω), and C_{10} is the 10-h capacity (Ah) at a reference temperature, commonly 25°C. For a dynamic model, considering charging and discharging models, the additional terms R_{Lc}, R_{id}, R_{co}, and R_{do} are added in both directions of current flow (Figure 19).

Temperature is a crucial factor for determining performance of the battery. Off-grid systems are commonly installed outdoors or in-house without temperature control, so we measured temperature versus battery capacity. As mentioned above, stable power sources are crucial for manufacturing processes so that temperature is not negligible. As shown in Figure 21, temperature and discharge rate are crucial factors for percent capacity so that temperature versus percent battery capacity surface (Figure 21) was generated with linear interpolation from Figure 20.

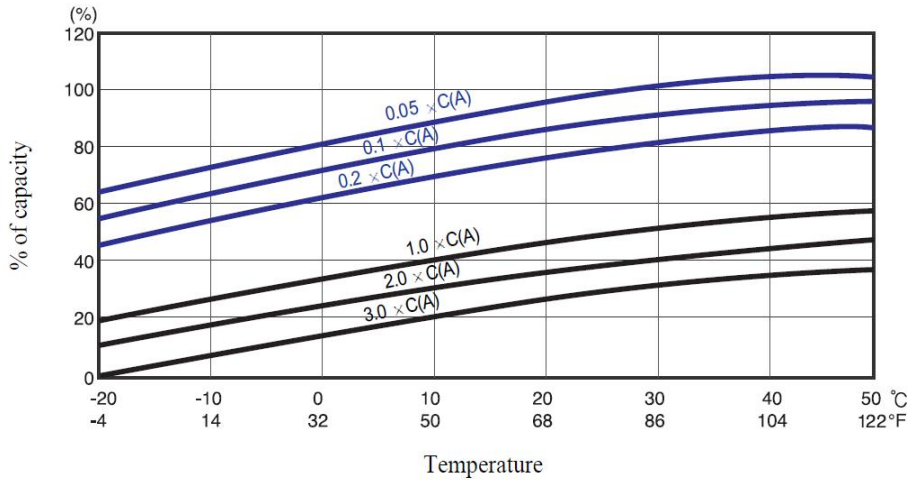

Figure 20. Relationship between temperature and discharge capacity (provided by manufacturer)

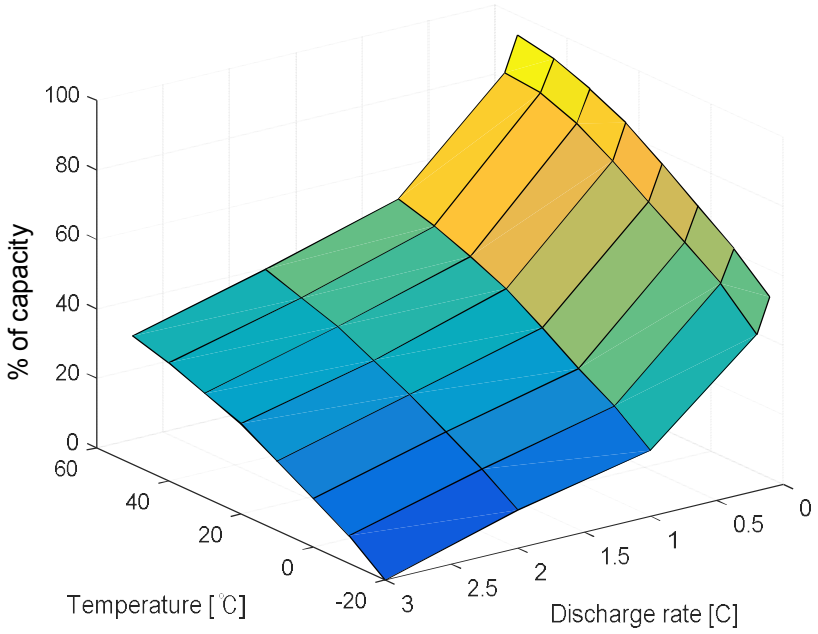

Figure 21. Temperature *vs.* percent capacity surface

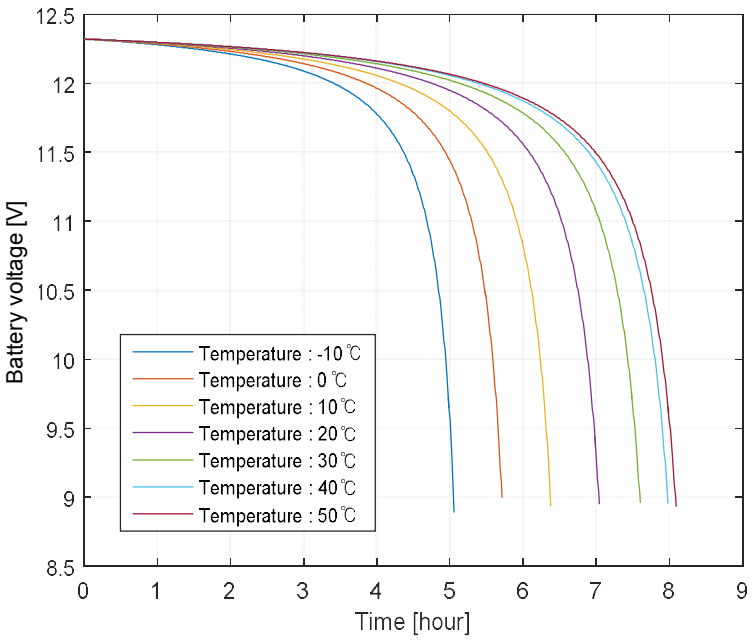

Figure 22. Equivalent battery model

Combining the SOC model and temperature versus percent capacity model, an equivalent battery model with temperature was developed. As shown in Figure 22, the lower the temperature, the faster the drop in external voltage. A monitoring platform measured the current flow of the battery and the SOC could be obtained by integrating current flow to the battery.

2.4 Combining models for a renewable energy plant

Each renewable energy model was combined and stored in a battery bank. In this research, manufacturing parameters are important so that energy consumption monitoring for the manufacturing process was implemented.

The power management system monitored the overall condition of the target system and if the voltage of a battery dropped to a pre-defined low limit value, it automatically terminated current flow from the battery to the manufacturing processes.

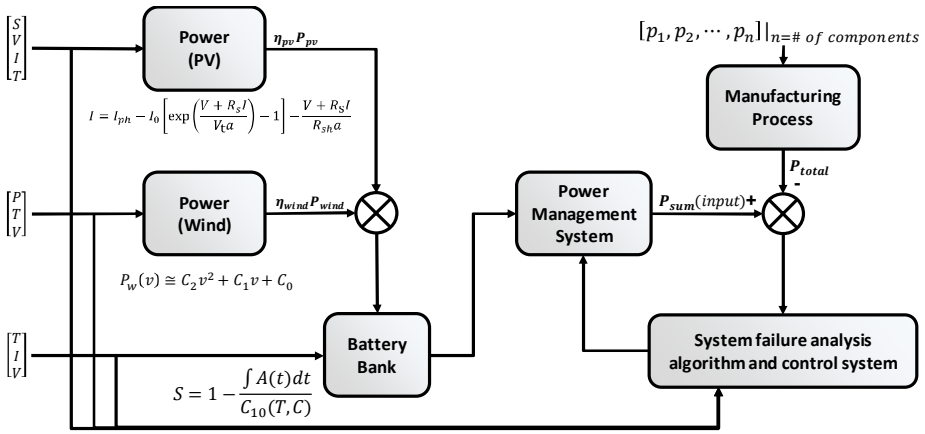

Figure 23. Schematics of the model for energy production and consumption

2.5 Operation time calculations

Operating time calculations were studied with energy production and a consumption model according to the following equation:

$$t_{est} = \frac{SOC(t,I) - SOC_{fail}}{\frac{P_{gen}(t) - P_{man}(t)}{V_{bat}(t)}} \cdot C_{10} = \frac{SOC(t,I) - SOC_{fail}}{I_{gen}(t) - I_{man}(t)} \cdot C_{10}$$
$$where, P_{gen}(t) - P_{man}(t) \neq 0$$

t_{est} is the estimated operation time of the off-grid renewable energy system and SOC_{fail} is a failure condition of the battery bank. I_{gen} and I_{man} denote the current flow of power generation and manufacturing. If I_{gen} is larger than I_{man}, energy is stored in the battery bank so that operating time increases until the battery bank is fully charged. Furthermore, current flow also affects the operating time. Operating time and instantaneous operating time can be calculated as shown in Figure 24 and Figure 25, respectively.

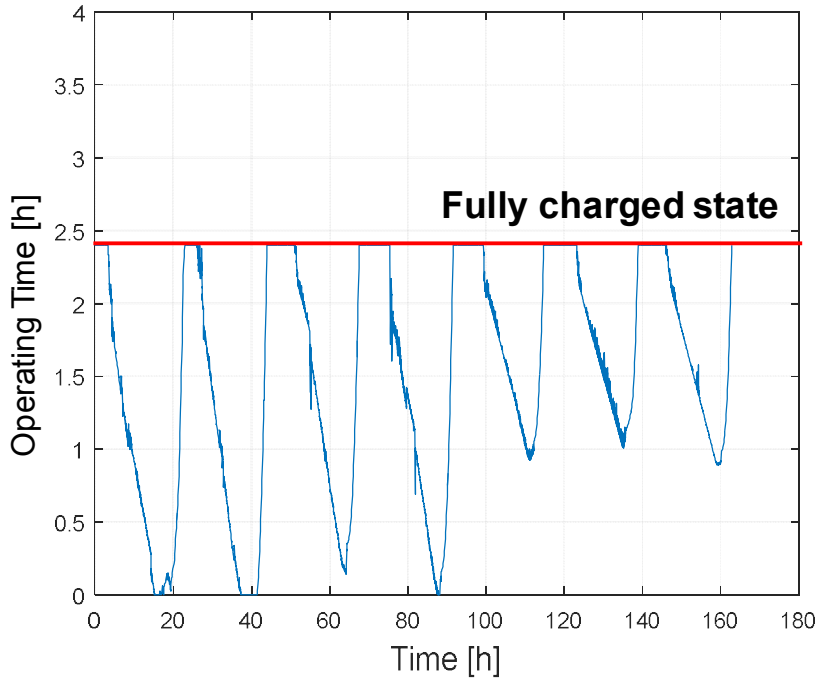

Figure 24. Operating times of the off-grid system (battery capacity = 240 Ah)

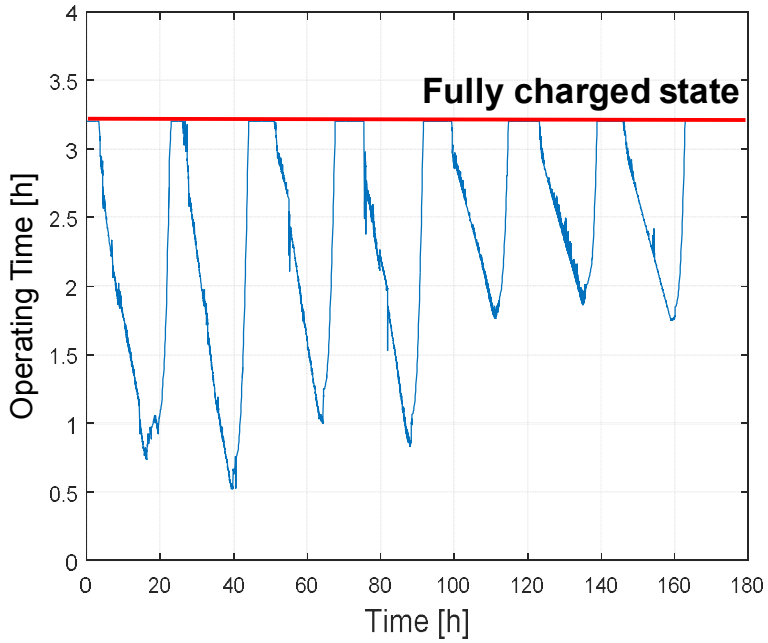

Figure 25. Operating times of the off-grid system (battery capacity = 320 Ah)

2.6 Conclusions

A renewable power model was reviewed and implemented to a renewable energy system simulator. Manufacturing power consumption was also considered to determine the stability of a manufacturing-oriented simulation. Furthermore, an operation time calculation algorithm was implemented.

3 Manufacturing energy consumption model

Conventional manufacturing processes require stable power sources. However, if a power source is not stable, such as an off-grid renewable energy system, estimating the power demand of the manufacturing process is crucial. Worldwide, the ratio of renewable energy sources is increasing so that it will be necessary to predict energy consumption in manufacturing processes. In this section, power demands for a manufacturing process were determined and modeled with process and empirical parameters of each manufacturing process: in this case, the lathe.

3.1 Overview

Energy efficiency has become an increasingly important issue in industry due to growing energy costs and environmental concerns [47]. Much research has been carried out with the aim of reducing the energy consumption of machine tools, using both experimental and theoretical methods. From the viewpoint of productivity, Dornfeld [48] developed an "eco-route map" that described the concept of improved

manufacturing processes and systems. Kara *et al.* [49] used the specific energy consumption (SEC) model for various work piece materials and machine tools. Yoon *et al.* [50] measured the power required for cutting, including tool wear, using the response-surface method (RSM). Gutowski *et al.* [51] proposed an energy framework to describe manufacturing processes, and the EnergyBlock planning method was proposed by Weinert *et al.* [52] to reduce the total energy consumption of manufacturing processes. Dietmair [53] studied the efficiency of machining processes using an energy consumption model. Xu *et al.* [54] developed a theoretical model to describe the required cutting power of machine tools, considering empirical coefficients as well as the geometric variables of the tool. Lee *et al.* [55] developed a detailed model describing the mechanical and electronic coefficients of a feed-drive system. Yoon *et al.* [56] compared the energy consumption of manufacturing processes, including bulk forming, cutting, and rapid prototyping.

As part of recent efforts to standardize the energy consumed by machine tools, the International Organization for Standardization (ISO) developed the ISO 14995 series of

standards [4]. The first part of these standards defines the design parameters of machine tools that affect energy consumption. The second part, which is still under development, describes energy consumption measurement procedures. The Japanese Standard Association (JSA) also developed standard power measurement procedures and specimens for cutting processes [57]. The JSA standard specimen for a three-axis milling machine was used by Min *et al.* [58] to calculate the energy consumption of machine tools of various sizes.

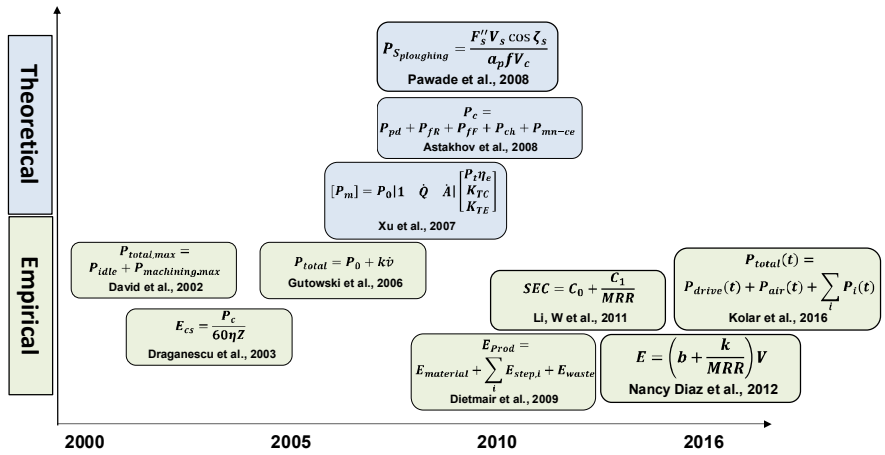

Figure 26. Research trends for machine tool energy consumption

There are two types of models for machine tool energy consumption: the first is theoretical and the second is empirical.

There are few theoretical models for machine tools and cutting power [54, 59, 60], and there are several empirical models. Because of the complexity of machine tool configurations and mechanical properties, an empirical model is commonly used to estimate energy consumption of machine tools.

The literature reviewed above describes various empirical approaches and measurement procedures. However, the development of standardized processes has been hindered by the number of parameters and the complexity of the procedures. For these reasons, we describe a simplified measurement method that integrates the feed drive, the spindle, and cutting. Six different machine tools were examined to verify the accuracy of the model.

3.2 Theoretical backgrounds on manufacturing energy consumption

The EnergyBlock method of Weinert *et al.* [52] was used to measure the energy consumption of the machine tool itself using the following two expressions:

$$P_p(t) = \begin{bmatrix} f_1(t) \ \forall t \ \in [T_0, T_1] \\ f_2(t) \ \forall t \ \in [T_1, T_2] \\ \dots \\ f_3(t) \ \forall t \ \in [T_{n-1}, T_n] \end{bmatrix}$$

and

$$E_p = \int_{T_0}^{T_n} P_p(t)dt$$

where f_n is the power profile within the time interval T_{n-1} to T_n, $P_p(t)$ is the power profile function, and E_p is the energy, which can be calculated by integrating $P_p(t)$ from T_0 to T_1.

A first-order polynomial energy model for the spindle and feed drive was assumed for simplicity [55, 61]. The SEC is widely used to describe the cutting energy. If the work piece material is known, then the SEC is a powerful tool to calculate the cutting energy, even though this varies with the cutting force, which is related to the cutting speed, the coolant, and the tool geometry. In this study, the cutting energy consumption was estimated using the material removal rate (MRR) model, inspired by the models of Kara *et al.* and Dornfeld *et al.* [49, 62], and the cutting energy consumption was decomposed using model equation 3, as suggested by Gutowski *et al.* [51].

$$P = P_0 + k\dot{v}$$

$$\text{where} \begin{cases} P = total\ power \\ P_0 = idle\ power \\ \dot{v} = the\ rate\ of\ material\ processing\ in\ cm^3/sec \\ k = a\ constant, with\ units\ of\ kJ/cm^3 \end{cases}$$

Here, we use the following basic form of the power model:

$$P_p(\alpha) = C_{0p} \cdot \alpha + C_{1p}$$

where $P_p(\alpha)$ is the power consumption of peripherals, such as idle, coolant, machining, spindle, and feed drive.

$$P_{Total} = P_{Idle} + P_{Coolant} + P_{Spindle} + P_{Feed} + P_{Machining}$$

$$,where \begin{cases} P_{Idle} = C_{1_i} \\ P_{Coolant} = C_{1_c} \\ P_{Spindle} = C_{0_s} \cdot RPM + C_{1_s} \\ P_{Feed} = C_{0_f} \cdot Feedrate + C_{1_f} \\ P_{Machining} = C_{0_m} \cdot MRR + C_{1_m} \end{cases}$$

In this manner, the power consumption of the machine tool is modeled as the sum of five terms: the power consumption for idle P_{Idle}, the power consumption of the coolant system $P_{Coolant}$, the spindle power consumption $P_{Spindle}$, the feed drive power consumption P_{ied}, and the cutting power consumption $P_{Machining}$.

C_{0s}, C_{1f}, and C_{0m} are the gradients of the power model of the cutting, spindle, and feed drive, respectively, and C_{1i} and C_{1c} are

the power offset coefficients for idling and/or the coolant pump.

3.2.1 Cutting process energy consumption model

Before obtaining cutting energy consumption, cutting force should be determined. Cutting force F_c can be calculated by Merchant' s circle, where F_c is the vector summation of F_s, resistance to shear of the metal in forming the chip, and F is the frictional resistance of the tool acting on the chip (Figure 27). In total, this is 70– 80% of the total force and it is parallel to the velocity of the tool relative to the work piece so that the cutting force F_c is a major factor in the energy consumption of the cutting process. Thus, cutting power, P, can be calculated with cutting force, F_c, and cutting speed, V.

$$P = VF_C$$

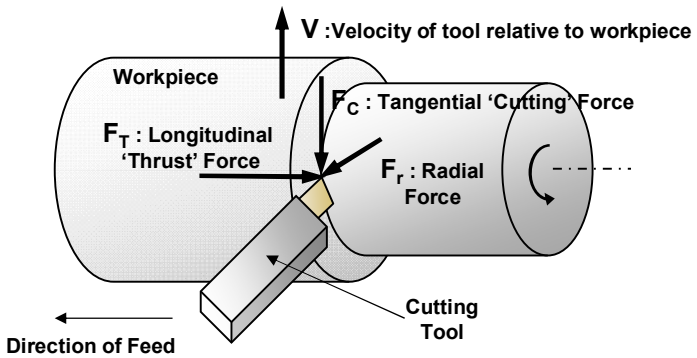

Figure 27. Cutting force diagram

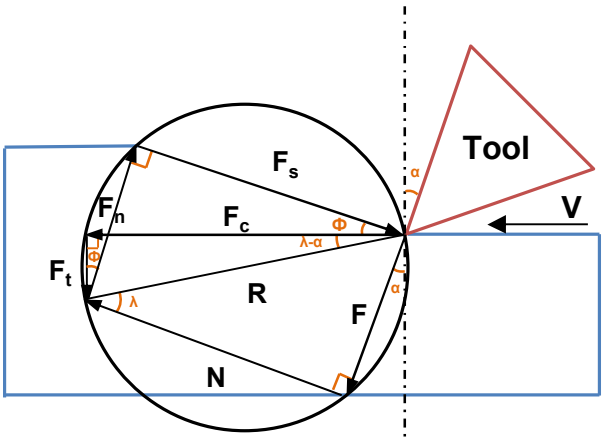

Figure 28. Merchant' s circle

Because of the complexity of the F_c calculation, the SEC model is commonly used for estimating the required energy for the cutting process. The SEC model is a simpler form of the cutting power model, rather than power calculated by cutting force if the cutting force is constant.

As shown in Figure 29, cutting force is constant with over 90 m/min of cutting speed [63]. Thus, if the cutting speed is high enough, the SEC model can be applied to estimate the cutting energy consumption.

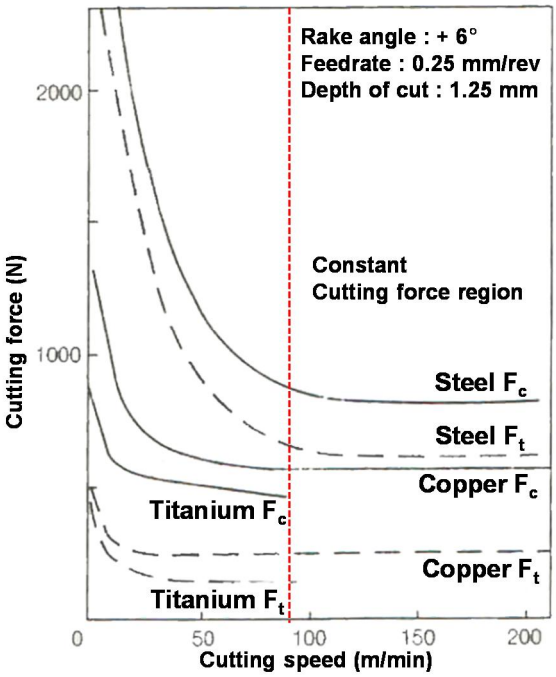

Figure 29. Trends of cutting speed versus cutting force [63]

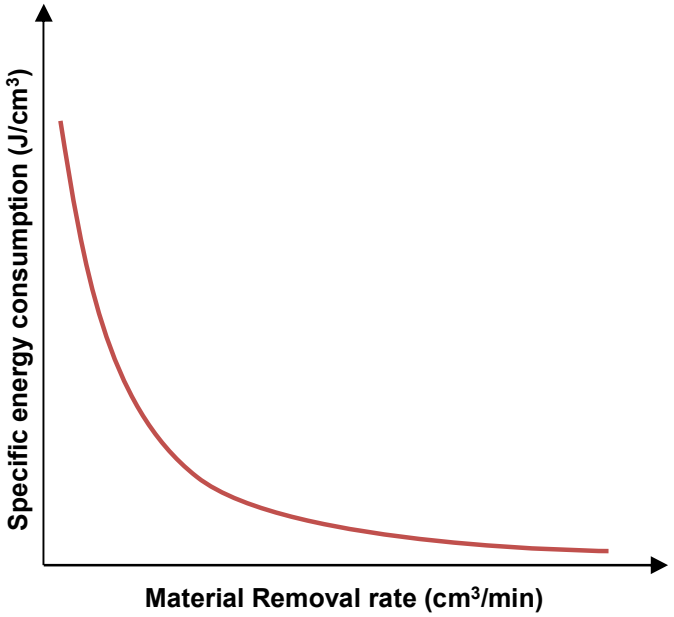

Figure 30. Typical curve of the SEC model [49]

$$SEC = C_0 + \frac{C_1}{MRR}$$

$$SEC \cdot MRR = C_0 \cdot MRR + C_1 = P_{machining}$$

The SEC model has two empirical variables, C_0 and C_1. A typical curve of the SEC model is shown in Figure 30 and the SEC model has been implemented by previous researchers [49, 50, 62, 64-66]. Two empirical variables should be obtained by experimental results within the constant cutting force region. Tool wear is directly related to cutting force [50], so tool manufacturers provide high-cutting-speed conditions.

3.2.2 Feed drive friction-based energy consumption model

For feed drive units, Lee *et al.* proposed a component-based friction model for estimating the energy demands of a machine tool [55]. Based on the friction model, power loss of the feed drive unit can be summarized as shown in Table 2.

Table 2. Composition and power losses of the feed drive system [55]

Component	Losses	Factors	Output
Motor drive	-	-	Driving power
Motor	Electrical Loss (P_{M1})	Idling loss Copper loss Iron loss	Driving torque of the motor
	Mechanical loss (P_{M2})	Inertial force Damping force Friction force	Torque used to drive the ball screw
Ball screw	Mechanical loss (P_B)	Inertial force Friction force	Force used to drive the table
Table with LM guide	Mechanical loss (P_L)	Inertial force Friction force	Table position

As Lee *et al.* mentioned power loss of each component, a common term for power loss at each component is feed rate. The following equations are described in [55]:

$$P_{M1} = P_t - 2\pi\dot{x}T_C/p_b$$

$$P_{M2} = 2\pi\dot{x}(T_C - T_l)/p_b$$

$$P_B = \dot{x}(2\pi T_l / p_b - F_l)$$

$$P_L = F_l \dot{x}$$

$$, where \begin{cases} T_C : Torque\ command \\ p_b : Ball\ screw\ lead \\ T_l : Torque\ used\ to\ the\ ball\ screw \\ F_l : Force\ used\ to\ drive\ the\ table\ and\ LM\ blocks \\ x : Table\ position \end{cases}$$

3.3 Standardized energy consumption measurement procedure

3.3.1 Assumptions and experimental design

Most existing methods that describe the energy consumption of machine tools are based on the concept of a standardized work piece; however, it is not always straightforward to use such a standardized work piece for an arbitrary machine tool because of the wide variety of types and configurations of machine tools. The energy consumed during cutting depends on several factors, including the work piece material, the cutting features, the tool material, the geometry, and the type of machine tool. This large number of factors complicates the development of a unified model. There has been substantial research into models of the cutting process and energy consumption during the cutting process using existing cutting

models.

An objective of this work was to separate the cutting energy from the energy consumption of machine tools, because the contribution of the machine tool to the cutting energy appears to be determined by the characteristics of the machine tool rather than the process. The cutting power consumption has been estimated using the cutting force and cutting speed [67], and the cutting force is proportional to the instantaneous feed rate and depth of cut if a machine tool cuts the same material with the same tool at a nominal cutting speed [68]; i.e., the process condition is the dominant variable used to estimate cutting power. If the energy consumption behavior of the machine tool itself can be described separately, it can be used to estimate the cutting energy. This method significantly reduces the time and effort required for measurements and modeling of the energy consumption of a machine tool, while providing an accurate estimate of the energy used by the machine tool, and the cutting energy.

The procedure consists of two steps. The first is to measure the energy consumption without cutting (i.e., the energy of an

air−cut), as well as the power consumption of the individual components. The second is to measure the cutting energy using the same sequence as in the first step to determine whether the cutting energy can be decoupled from the energy used by the machine tool without cutting.

3.3.2 Data measurement and analysis procedure

The energy measurement procedure is as follows:

Step 1. *Initiate energy measurement*

Step 2. *Idle state: 30 s*

Step 3. *Coolant pump: 30 s*

Step 4. *Cutting, spindle, and feed drive*

A. *Spindle on*

B. *Cutting*

C. *Travel + x-axis*

D. *Travel – z-axis*

E. *Travel – x-axis*

F. *Change spindle speed (with a constant cutting speed)*

G. *Cutting*

H. *Repeat from A*

Step 5. *Spindle and coolant off*

Step 6. *End of energy measurement*

A dwell time of 5 s is included between each step to identify the times when the power profile changes. After defining the start and end points of the profile, the power consumption was calculated from the average of the profile, subtracted from the average of the dwelling profile (i.e., the tare energy), which is a widely used decomposition process [50, 66]. The power

consumptions of the idle state and coolant pump are measured for 30 s to determine the saturated power profile. After measuring, the power consumption of the peripherals, the spindle and feed drive is moved to cut the workpiece, as shown in Figure 31.

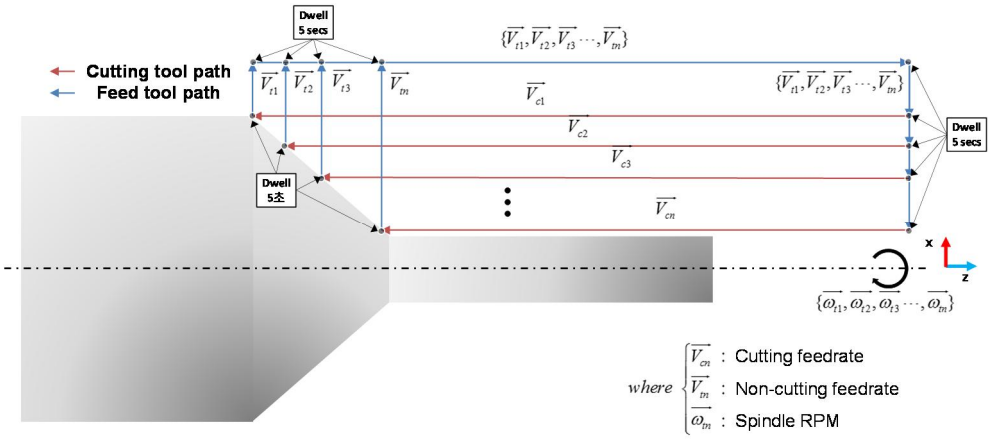

Figure 31. Detailed cutting power measurement procedure

Aramcharoen *et al.* [69] studied the power requirements of milling machines, and found that as long as an axis is not perpendicular to the force of gravity, the power demands of the axis are almost the same in the + and − directions. Thus, the power in the z−axis is measured only in the + direction (Figure 31).

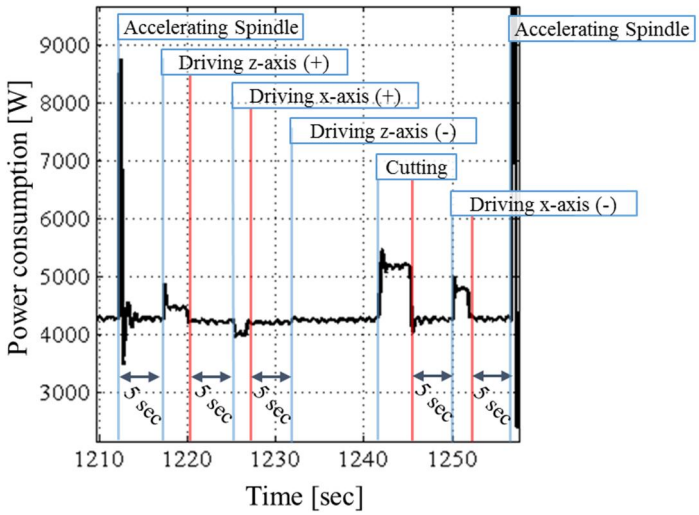

Figure 32. Example of a power profile and power measurement procedure

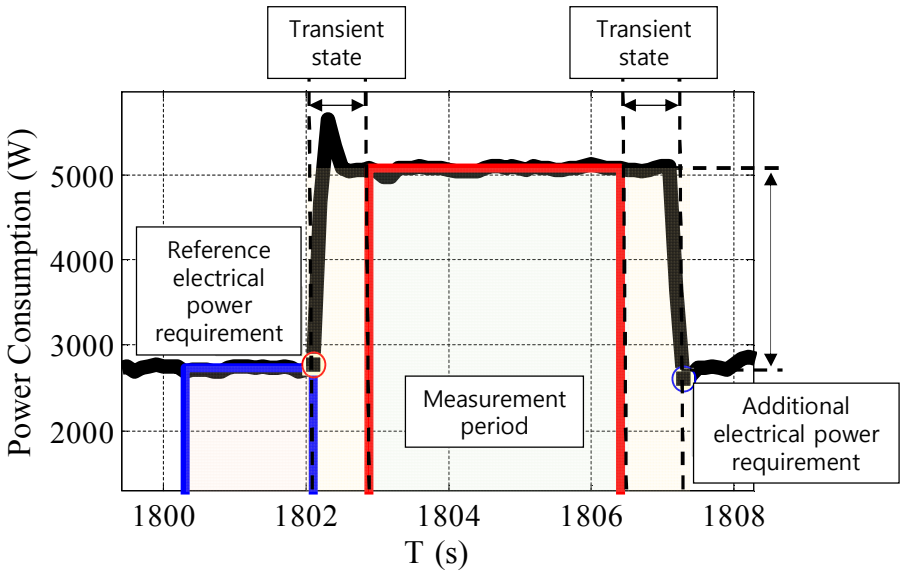

Figure 33. Decomposition of additional electrical power requirement

In this study, the measurements of energy consumption during the cutting, the spindle, and the feed-drive steps were repeated 45 times to complete three sets of the Box- Behnken

experimental design. The speeds of the spindle and the $+x$, $-x$, and $-z$ feed drives were increased gradually to control the cutting speed. The spindle speed was controlled to provide a constant cutting speed, and the feed rate was increased from 3,250 to 5,000 mm/min at intervals of 250 mm/min. Table 1 lists the cutting conditions. Horizontal cutting was carried out using 60-mm diameter AISI1045 mild steel rods, and a carbide CNMG type insert tool, with a positive rake angle of 15°.

A Yokogawa WT330 digital power meter was used to measure the energy consumption of the machine tool (Figure 34). The sampling rate was 10 Hz, and no low-pass filter was used. Six different machine tools were investigated. Table 2 lists the specifications of these machines. Only the saturated profiles were analyzed, to investigate the effects of over-shooting the power profile for each component. Acceleration and deceleration were neglected due to the low sampling rate.

The total power demand of the machine tool includes the combined demands of the idle, coolant, spindle, feed drives, and cutting power, which were determined individually. Thus, the additional electrical energy required was calculated by

subtracting the mean value of the reference electrical power requirement from the mean value of the measurement period electrical power demand (Figure 33).

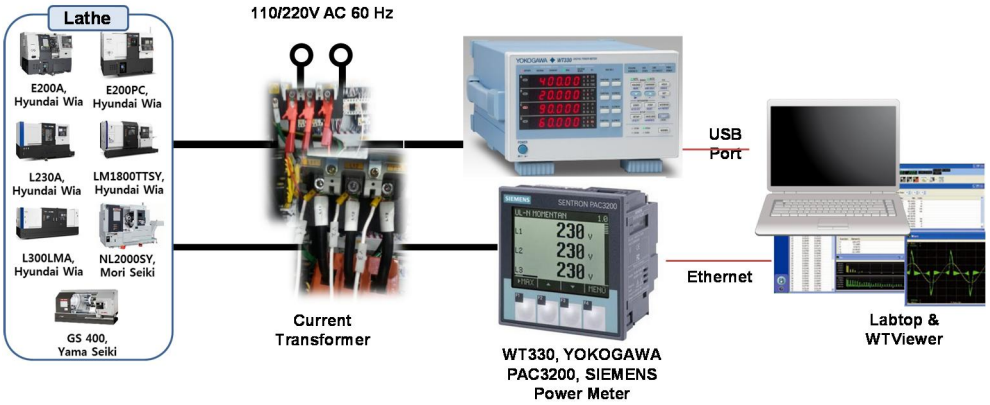

Figure 34. Block diagram of power trend acquisition setup

3.4 Results

The idle power consumption and the power consumption of a coolant pump are related to the numerical controller and the coolant pump itself. The idle power consumption and the power consumption of a coolant pump are constants [52, 53, 58, 69].

Model coefficients were calculated from the experimental results. The model results were fitted using linear regression, as shown in Figure 36– Figure 37. The spindle power consumption was fitted with a coefficient of determination of R^2 > 0.9, and the cutting power consumption was fitted with a coefficient of determination of R^2 > 0.99. A value of R^2 > 0.9 shows that the regression fit the data well.

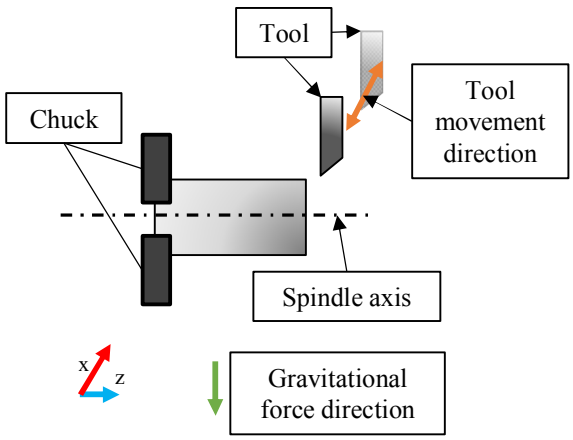

Figure 35. Axis orientation of CNC lathe

The energy consumption of the spindle and the feed drive

without cutting increased as the spindle speed and feed rate increased. The x−axis was not perpendicular to the direction of the force due to gravity, as in a typical lathe configuration (Figure 35). Thus, the energy consumption of the x−axis was influenced by gravity. The model described the energy consumption well.

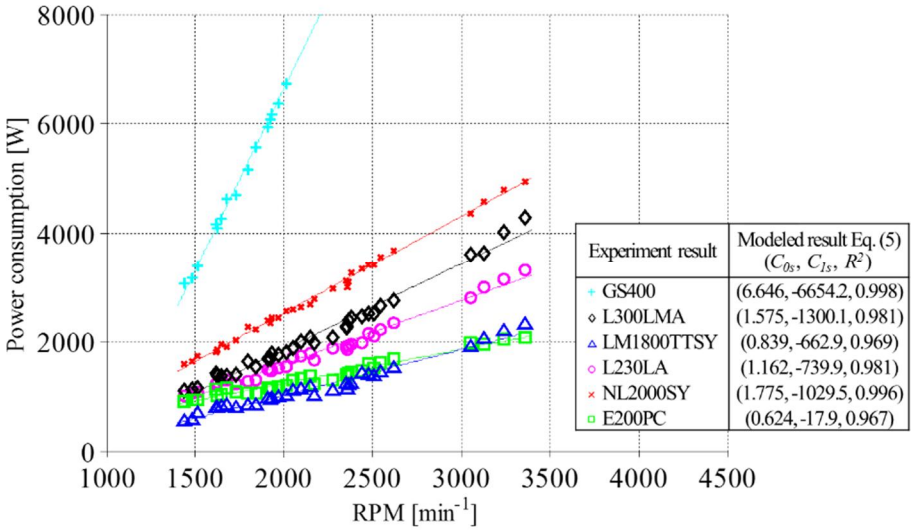

Figure 36. Spindle power of the machine tools

The energy consumption of the spindle and the feed drive vary from one machine tool to another. This variation is due primarily to the design of the machine tool. Even machine tools of similar scales have different characteristics due to differences in the feed drive system, the spindle, and their inertial mass. Further studies will be required to understand the influence of these parameters and to establish design rules for

'green' machines.

The cutting energy increased as the MRR increased and varied linearly with the MRR (Figure 38). The cutting energy varied little between the six machines, although these machine tools had different specifications. This suggests that the cutting energy is not strongly dependent on the design or components of the machine tool. Thus, the cutting energy can be decoupled from the characteristics of the machine tool, and the models for the spindle and the feed drive can be used as inputs to the cutting-energy model. The most interesting trend in the cutting power consumption occurred when the machine tool was equipped with a controller from Fanuc Corporation. In particular, the five machine tools (i.e., GS400, L230LA, L300LMA, NL2000SY, and LM1800TTSY) exhibited very similar cutting power consumption models because the gradients of the cutting power consumption model, C_{0m}, were nearly the same.

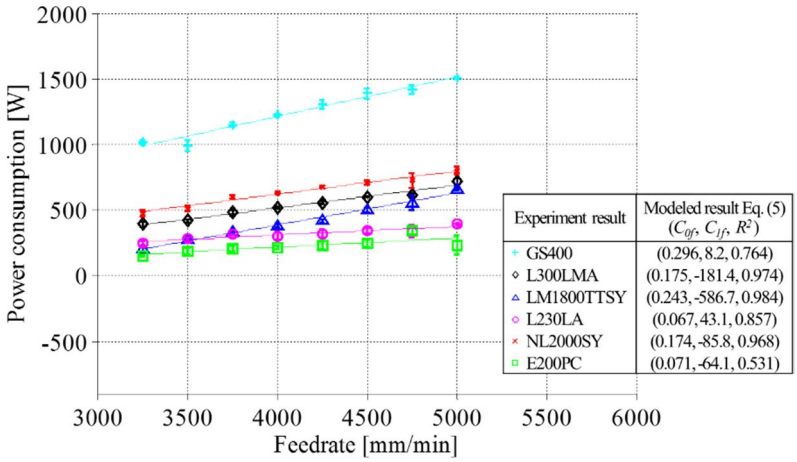

a) +x-axis direction.

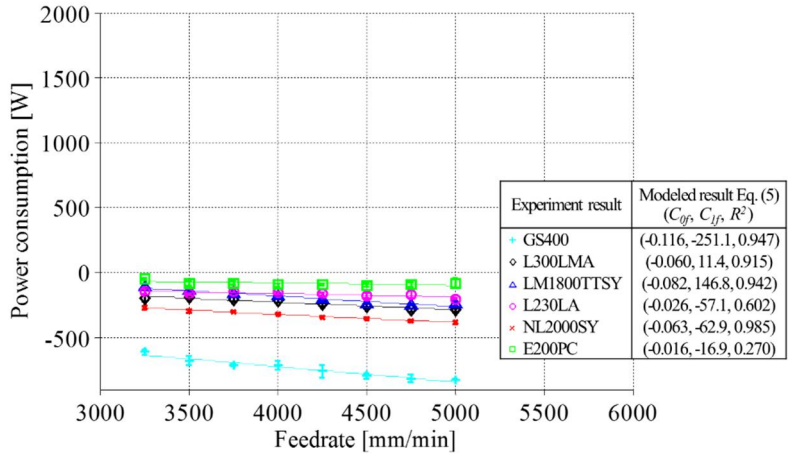

b) –x-axis direction.

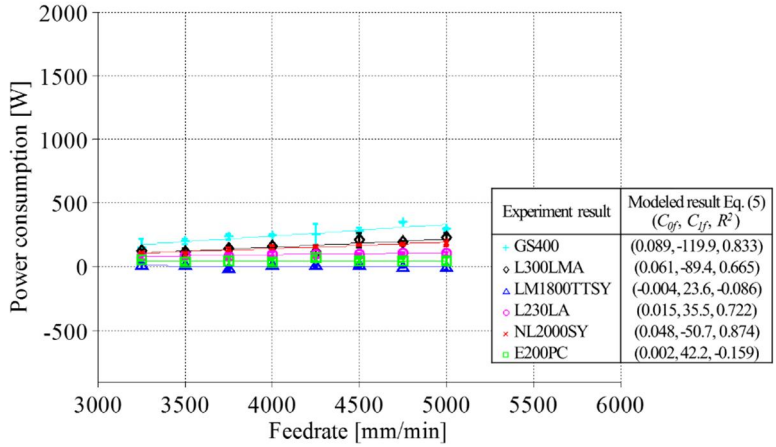

c) +z-axis direction.

Figure 37. The feed drive power of machine tools

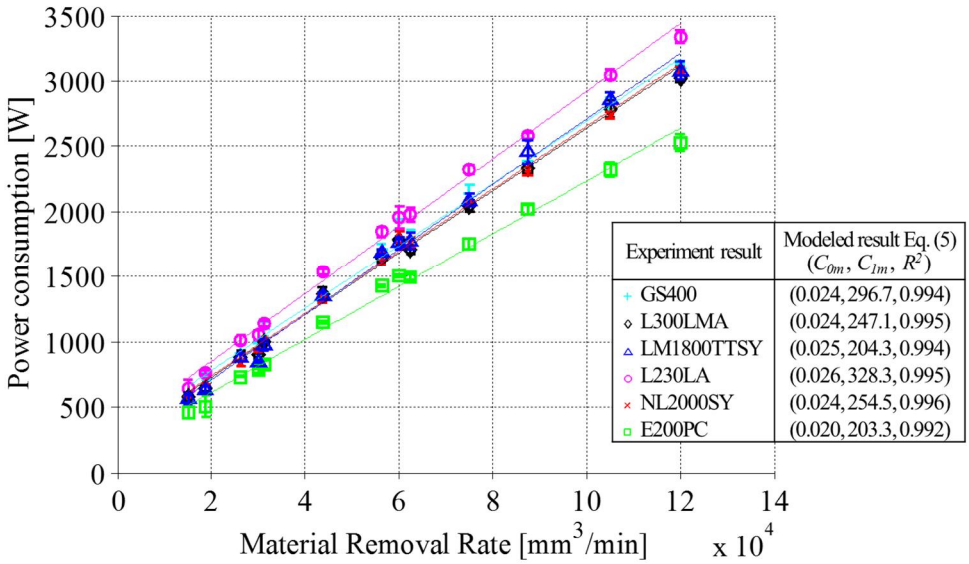

Figure 38. The cutting power of machine tools

The feed drive energy increased as the feed rate increased. The power demands of the x−axis were modeled separately in the + and − directions, and in the + z−axis direction only (Figure 37). As discussed above, power models in the +x−axis had a positive relationship with the feed rate, as shown in Figure 37−a; however, along the - x−axis, the power models exhibited a negative relationship with the feed rate, as shown in Figure 37−b [69]. However, some feed drive models were modeled with R^2 < 0.9. With the E200PC, R^2 was much smaller than with the other machine tools because of fluctuations in the power profile due to the characteristics of this machine tool. In the +z−axis direction, R^2 was smaller than in the x−axis; this

was because the signal-to-noise ratio in the z-axis was larger than that in the x-axis due to the larger power consumption in the x-axis.

3.5 Energy consumption simulator

3.5.1 Overview

The power consumption of a machine tool depends on the control parameters, including the NC code. The power consumption of each component is separated in the model; however, the power consumption of machine tools is the sum of each of the peripherals. Thus, we should sum the contributions from the different components of the model to describe overall power consumption of the machine tool. In this section, we describe the power profile simulation method.

The first step of this model is to export the operating conditions for the machine tool. The machine tool operating information is analyzed as a time-based array. The time information is calculated from the position and feed rate data. In the model, we require only the times when the peripherals' conditions change.

The second step is to include the machine tool operating conditions matrix in the time information array. We use the models in Equation 5, which require operating parameters with

a time array. The feed rates for each axis are linearly interpolated. The feed rates for each axis are calculated as a function of the position.

3.5.2 Simulation procedure and results

The model was confirmed using a simulation tool. The power profile simulation was composed of an NC code analyzer and a time-wise power profile solver. The total power consumption of the machine tool can be calculated as the sum of each of the components of the power consumption model; i.e.,

$$P_{Total}(\bar{\Gamma}, \bar{T}, \overline{C_1}, \overline{C_0}) = P_{Idle}(\bar{T}, C_{0_i}) + P_{Coolant}(\bar{T}, C_{0_c})$$
$$+P_{Feed}\left(\bar{T}, \overline{C_{1_{feed}}}, \overline{C_{0_{feed}}}, \overrightarrow{\overline{Feed}}\right) + P_{Machining}(\bar{T}, C_{1_m}, C_{0_m}, MRR)$$

$$where\ \bar{T} = \begin{bmatrix} t_0 \\ t_1 \\ \cdots \\ t_n \end{bmatrix} = \begin{bmatrix} |\overrightarrow{D_1}| \cdot \frac{1}{|\overrightarrow{Feed_1}|} \\ |\overrightarrow{D_2}| \cdot \frac{1}{|\overrightarrow{Feed_2}|} \\ \cdots \\ |\overrightarrow{D_n}| \cdot \frac{1}{|\overrightarrow{Feed_n}|} \end{bmatrix}, \bar{\Gamma} = \begin{bmatrix} On/Off \\ On/Off \\ \overrightarrow{\overline{Feed}} \\ RPM \\ MRR \end{bmatrix}, \overline{C_1} = \begin{bmatrix} \left[\overline{C_{1_f}}\right] \\ C_{1_s} \\ C_{1_m} \end{bmatrix}, \overline{C_0} = \begin{bmatrix} C_{0_i} \\ C_{0_c} \\ \left[\overline{C_{0_f}}\right] \\ C_{0_s} \\ C_{0_m} \end{bmatrix}$$

$$n\ is\ \#\ of\ process$$

$$On/Off = \begin{cases} 1, & t \geq t_n \\ 0, & t < t_n \end{cases}$$

Information on the operation of the machine tool was imported from the NC code. The power consumption model was developed using the operating conditions included in the NC code. Thus, the power profile simulator required only the NC code, the cutting variables, and the MRR. The NC code contains

only point-to-point position and feed rate data, and the NC controller interpolates velocities to drive the stage to the desired positions. The power consumption model contains the power consumption for each axis and at each feed rate independently, and interpolated velocities were calculated using the following expression:

$$\begin{bmatrix} \overrightarrow{\dot{D}_{n_x}} \\ \overrightarrow{\dot{D}_{n_y}} \\ \overrightarrow{\dot{D}_{n_z}} \end{bmatrix} = \begin{bmatrix} (\overrightarrow{\dot{D}_n} \cdot \vec{u})\vec{u} \\ (\overrightarrow{\dot{D}_n} \cdot \vec{v})\vec{v} \\ (\overrightarrow{\dot{D}_n} \cdot \vec{w})\vec{w} \end{bmatrix}$$

The time-wise power profile simulator was composed of four steps (Figure 39). In the syntax interpreter step, the NC code was imported and the operating conditions were determined using the linear interpolation (G2), spindle (S), coolant (M8), and dwell (G4) for each line of code.

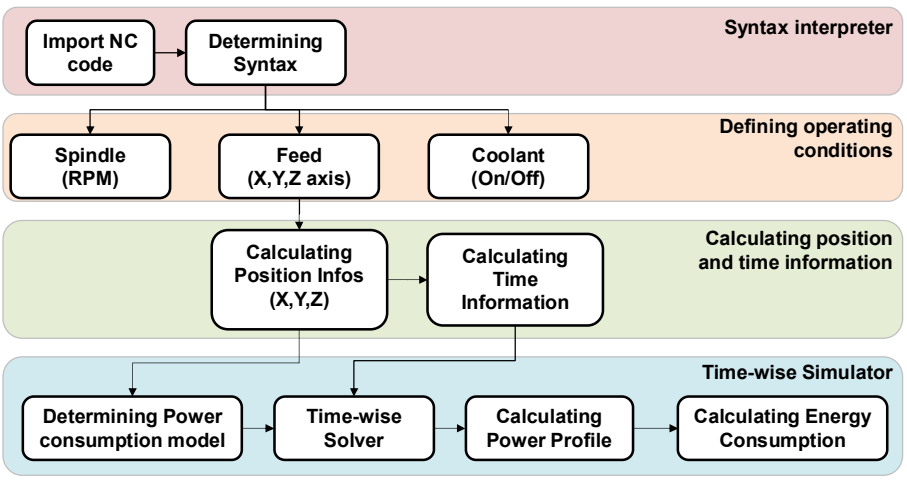

Figure 39. Flow chart describing the power profile simulation

After defining the syntax, the conditions of each of the components were defined using the condition array, $\bar{\boldsymbol{\Gamma}}$. Positions and time data were then calculated using the feed information as follows and shown in Figure 40:

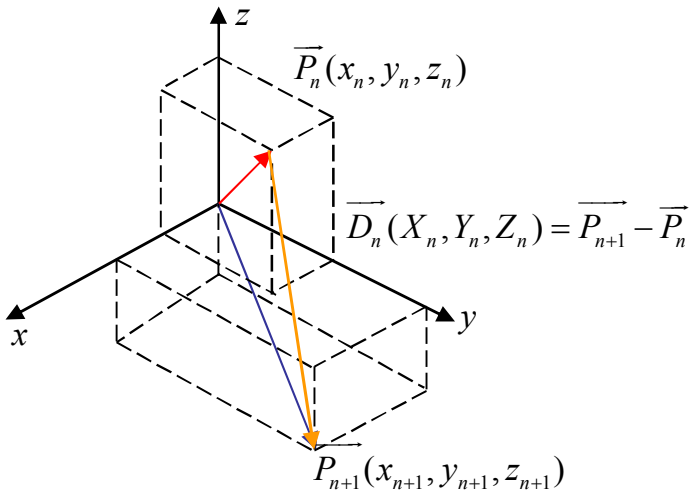

Figure 40. Definition of the feed drive position vector

$$\left|\overrightarrow{D_n}\right| = \sqrt{(x_{n+1} - x_n)^2 + (y_{n+1} - y_n)^2 + (z_{n+1} - z_n)^2}$$

$$\overrightarrow{\overrightarrow{Feed}} = \frac{d\left|\overrightarrow{D_n}\right|}{dt} = \left|\dot{\overrightarrow{D_n}}\right|$$

$$\overrightarrow{D_n} \cdot \vec{u} = \left|\dot{\overrightarrow{D_n}}\right| \cdot cos\left(tan^{-1}\left(\frac{\sqrt{((y_{n+1} - y_n)^2) + ((z_{n+1} - z_n)^2)}}{\left|\dot{\overrightarrow{D_n}}\right|}\right)\right)$$

$$\overrightarrow{D_n} \cdot \vec{v} = \left|\dot{\overrightarrow{D_n}}\right| \cdot cos\left(tan^{-1}\left(\frac{\sqrt{((x_{n+1} - x_n)^2) + ((z_{n+1} - z_n)^2)}}{\left|\dot{\overrightarrow{D_n}}\right|}\right)\right)$$

$$\overrightarrow{D_n} \cdot \vec{w} = \left|\overrightarrow{D_n}\right| \cdot cos\left(tan^{-1}\left(\frac{\sqrt{((x_{n+1} - x_n)^2) + ((y_{n+1} - y_n)^2)}}{\left|\overrightarrow{D_n}\right|} \right) \right)$$

The power profile simulator was used to calculate the power consumption of each component from the beginning to the end of each time step. We used a time step of 0.1 s.

The power profile simulator was used to calculate the power consumption of each of the peripherals at each time step. Figure 41 shows that the actual power profile and simulated power profile fit well. Figure 42 shows the power profile of the machine tool peripherals. The idle power consumption was constant at the beginning of the simulation. As the spindle speed changed, the power consumption of the feed drive changed depending on the feed rate. The sum of the peripherals was equal to the total power consumption (Figure 41).

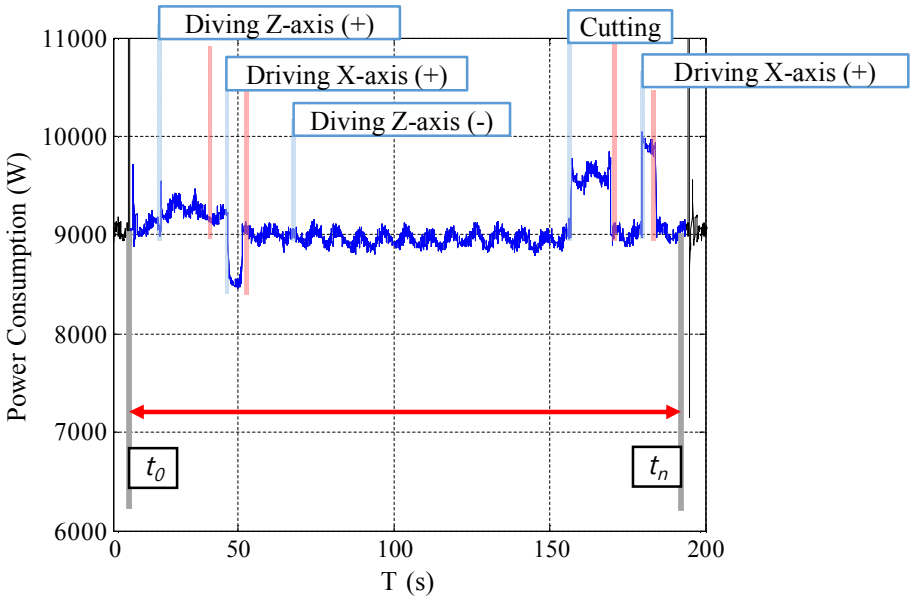

a) Actual power profile result

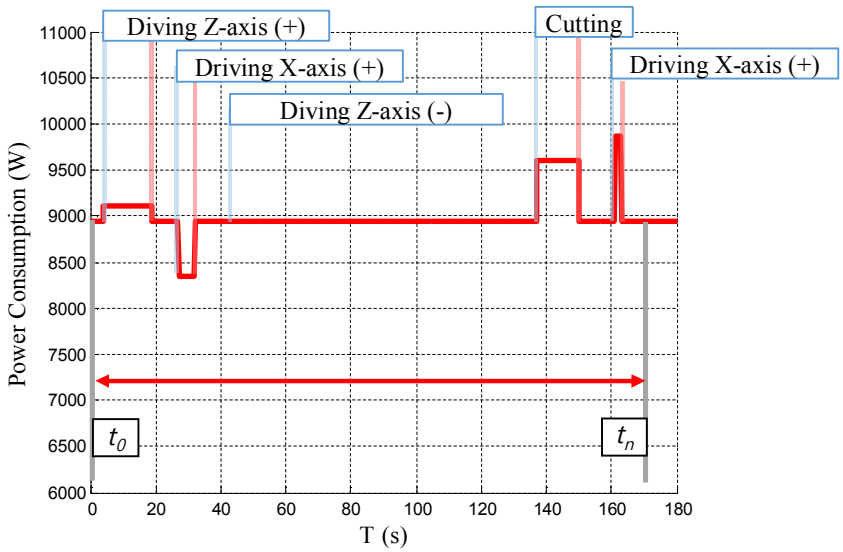

b) Simulated power profile result

Figure 41. Example of an actual power profile and a simulated power profile

To confirm the power model and the simulation method, we simulated the total energy consumption of the GS400 and NL2000SY machine tools, and compared values with the measured energy consumption. The measured energy consumption of the GS400 was 42.14 MJ, and that of the NL2000SY was 20.54 MJ; the respective simulated energy consumption values were 41.99 and 20.65 MJ. The power consumption of the GS400 spindle did not exceed 6637.8 W, due to the maximum spindle speed of 2,000 RPM. The simulated total energy consumption of the GS400 was in agreement with the measured result to within 0.36%, and the simulated total energy consumption of the NL2000SY was in agreement with the measured data to within 0.55%. Although the total energy consumption of the NL2000SY was much less than that of the GS400, the process times of the two machines were similar, and the machining power consumption did not differ significantly between the two machines.

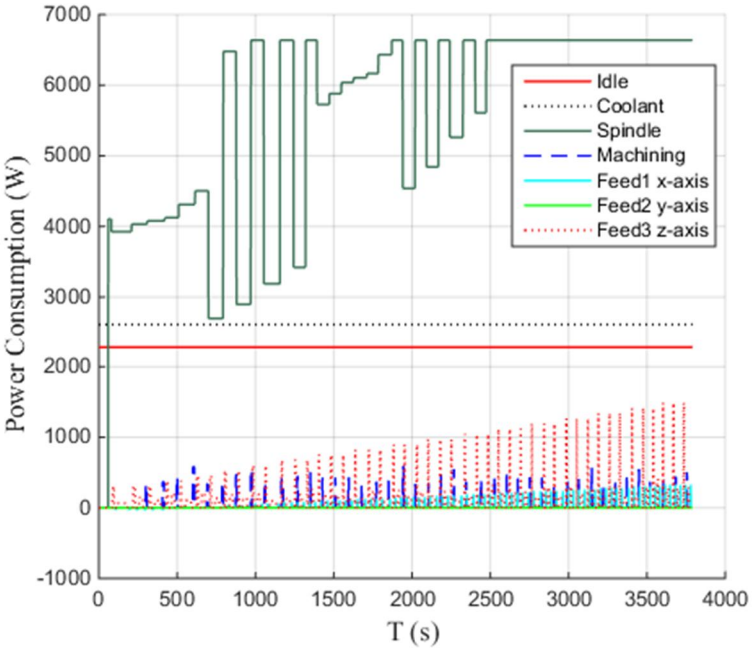

(a) Power profile result of GS400

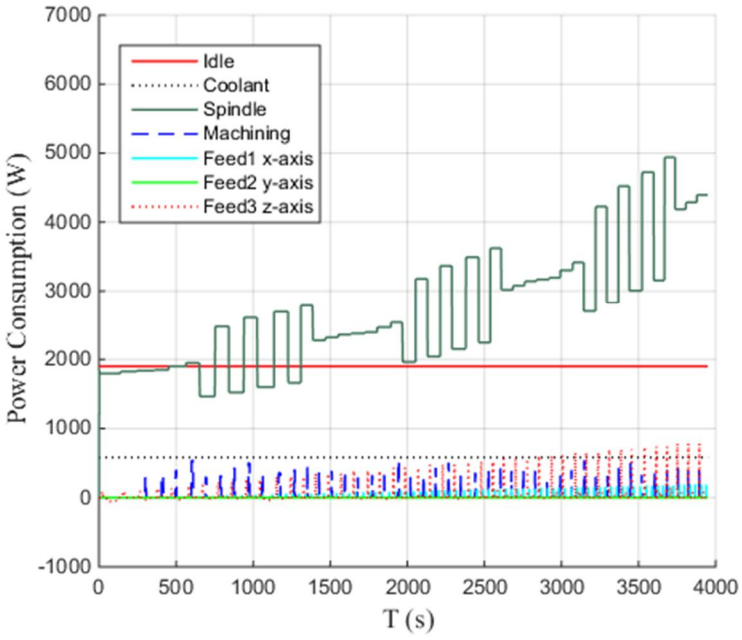

(b) Power profile result of NL2000SY

Figure 42. Simulated power profile of the machine tool peripherals

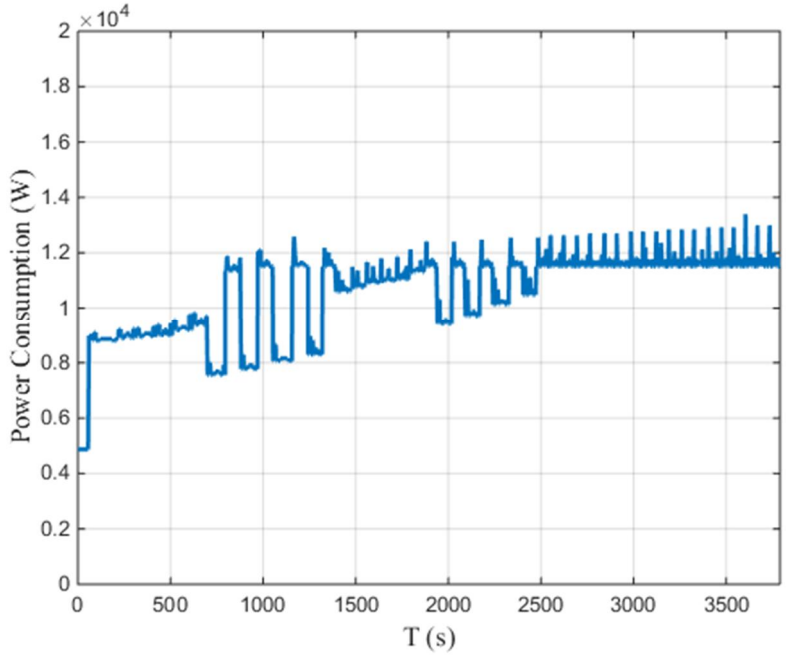

(a) Power profile result of GS400 (total power)

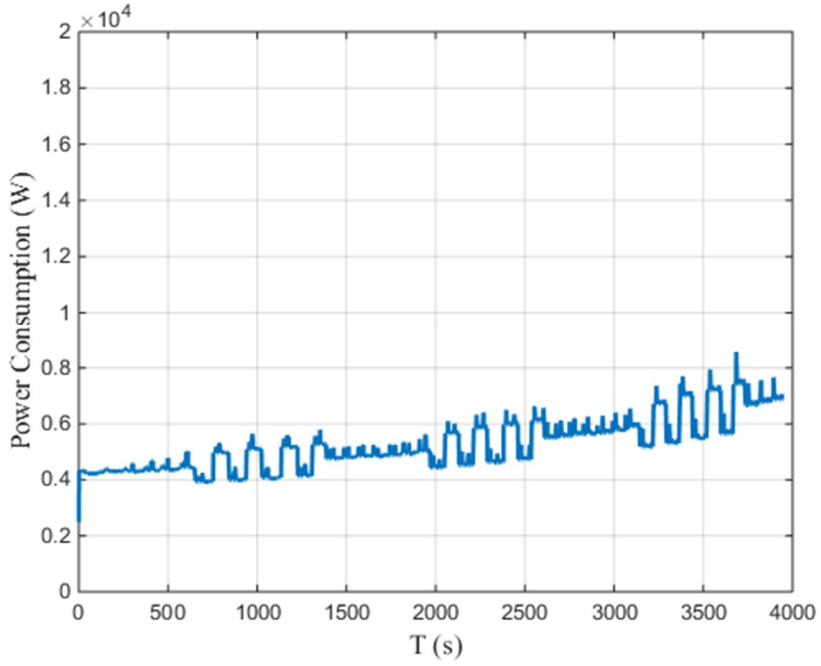

(b) Power profile result of NL2000SY (total power)

Figure 43. Simulated power profile of the machine tools

From the simulated data, the spindle power coefficient, C_{0s}, was much larger for the GS400 than the NL2000SY; however, the difference in the power trend coefficient is not necessarily an indicator of a greener machine tool, and criteria describing how green a given machine tool is should consider the scale and use of the machine.

3.6 Machine learning-based energy consumption modeling

3.6.1 Overview

A time-wise simulator could obtain the power consumption of a machine tool. However, the overall procedure of modeling requires aborting an ongoing process and attempting the proposed measurement procedure. Thus, a machine learning-based modeling methodology is one solution for obtaining a power model of the manufacturing process.

3.6.2 Physical model-based neural network design

In section 0, power trends of manufacturing processes could be obtained by a summation of first-order polynomial functions with process parameters, which is described in the NC code. Thus, the power can be simplified with the following equation:

$$P_{Total}(x_1, x_2, \ \ldots, x_n) \ = \ C_0 + C_1 x_1 + C_2 x_2 + \cdots + C_n x_n$$

$$P_{Idle}(\bar{T}, C_{0_{Idle}}) = C_{0_{Idle}}$$

$$P_{Coolant}(\bar{T}, C_{0_{Coolant}}) = C_{0_{Coolant}}$$

$$P_{Spindle}\left(\bar{T}, C_{1_{Spindle}}, C_{0_{Spindle}}, RPM\right) = C_{1_{Spindle}} \cdot RPM + C_{0_{Spindle}}$$

$$P_{Feed}\left(\bar{T}, \overline{C_{1_{Feed}}}, \overline{C_{0_{Feed}}}, \overrightarrow{\overrightarrow{Feed}}\right) = \overline{C_{1_{Feed}}} \cdot \overrightarrow{\overrightarrow{Feed}} + \overline{C_{0_{Feed}}}$$

$$P_{Machining}\left(\bar{T}, C_{1_{Machining}}, C_{0_{Machining}}, MRR\right) = C_{1_{Machining}} \cdot MRR + C_{0_{Machining}}$$

Based on the form of the equation above, an artificial neural network (ANN) with a pure line function was used as a transfer function of the network and the output form of the network is equal to the power model. Labeled data sets were generated with the simulator and training.

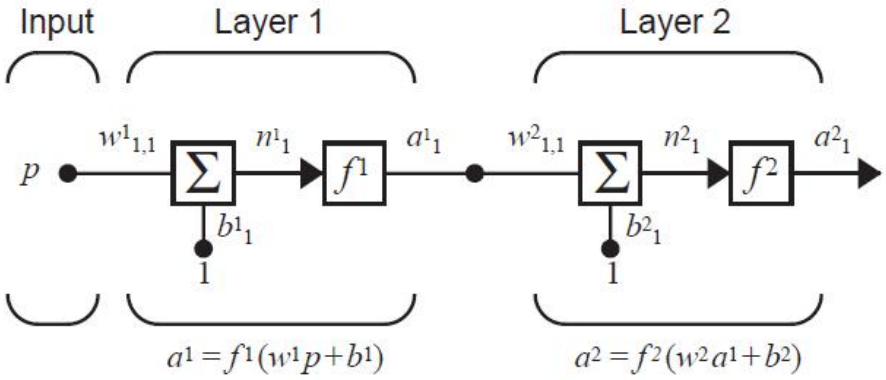

Figure 44. Block diagram of a two-layer artificial neural network (ANN) [70]

$$a^2 = f^2(w^2 f^1(w^1 p + b^1) + b^2)$$

$$\text{,where} \begin{cases} p & \text{is a vector of input parameters} \\ w_{m,l}^{n} & \text{is weight matrix of } n^{th} \text{ layer} \\ b_{m}^{n} & \text{is bias matrix of } n^{th} \text{ layer} \\ a_{m}^{n} & \text{is output parameters vector of } n^{th} \text{ layer} \\ f^{n}(a) & \text{is transfer function of } n^{th} \text{ layer} \end{cases}$$

$$a^2 = w^2 w^1 p + b^1 + b^2 \qquad , where\ f(a) = purlin(a) = wa + b$$

$$a^2 = W_0 x_0 + W_1 x_1 + \cdots + W_n x_n + B_0, \text{where} \begin{cases} W_n = w^2 w^1 \\ B_0 = b^1 + b^2 \\ p = \begin{bmatrix} x_0 \\ x_1 \\ \vdots \\ x_n \end{bmatrix} \end{cases}$$

3.6.3 Backpropagation algorithm

To train the hidden layer of the ANN, a backpropagation algorithm was implemented.

$$W^m(k+1) = W^m(k) - \frac{\alpha}{Q}\sum_{q=1}^{Q} s_q^m \left(a_q^{m-1}\right)^T$$

$$\mathrm{b}^m(k+1) = \mathrm{b}^m(k) - \frac{\alpha}{Q}\sum_{q=1}^{Q} \mathrm{s}_q^m$$

$$\mathrm{s}^M = -2\dot{\mathrm{F}}^M(\mathrm{n}^M)(\mathrm{t}-\mathrm{a})$$

$$\mathrm{s}^m = \dot{\mathrm{F}}^m(\mathrm{n}^m)\left(\mathrm{W}^{m+1}\right)^T \mathrm{s}^{m+1},\ for\ m = M-1, \ldots, 2, 1$$

$$\dot{\mathrm{F}}^m(\mathrm{n}^m) = \begin{bmatrix} \dot{f}(n_1^m) & 0 & \cdots & 0 \\ 0 & \dot{f}(n_2^m) & \cdots & 0 \\ \vdots & \vdots & & \vdots \\ 0 & 0 & \ldots & \dot{f}(n_{S^m}^m) \end{bmatrix}$$

3.6.4 Results

ANN training parameters are described in Table 3. Six input neurons are for manufacturing operation conditions and only one output neuron is for the power demand for manufacturing at the last layer of the ANN. The number of hidden layers is 100, which is considered a high level. The initial learning rate is low

because of the highly sensitive variables due to the Purelin function. At first, the state of training, all weights, and biases are initiated with random variables so that the error in the first state is high and the backpropagation algorithm is easily unstable. Thus, the learning rate of the designed ANN would be low.

Table 3. ANN design and training parameters

Name of variable	*Value*	*Note*
Number of layer	*3*	-
Number of input neurons	*6*	*6 operating parameters*
Number of output neurons	*1*	*Only power obtained*
Number of hidden neurons	*100*	*High level of degree*
Transfer function	*Purelin()*	*Due to physical model*
Training data set	*2,000*	*Random samples*
Verification data set	*37,907*	*Generated by simulator*
Initial learning rate	1.0×10^{-4}	-
Learning rate	5.0×10^{-5}	*Automatically adjusted*

For faster learning of the power profile of a machine tool, an adjustable-learning-rate algorithm was implemented and the final learning rate was 5.0×10^{-5}. The performance index is shown in Figure 45 and it converges well with the low learning rate. Results of the ANN are shown in Figure 46 and the results are summarized in Table 4. The number of iterations was over 640,000 and the error of the actual results and trained results was 1.28%.

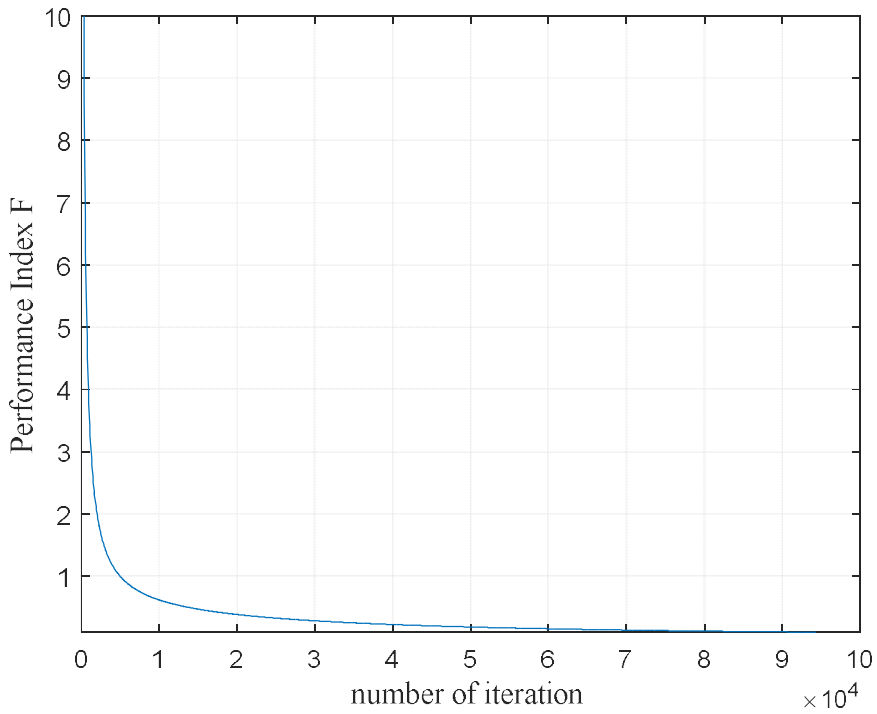

Figure 45. Results of performance index *vs.* number of iterations

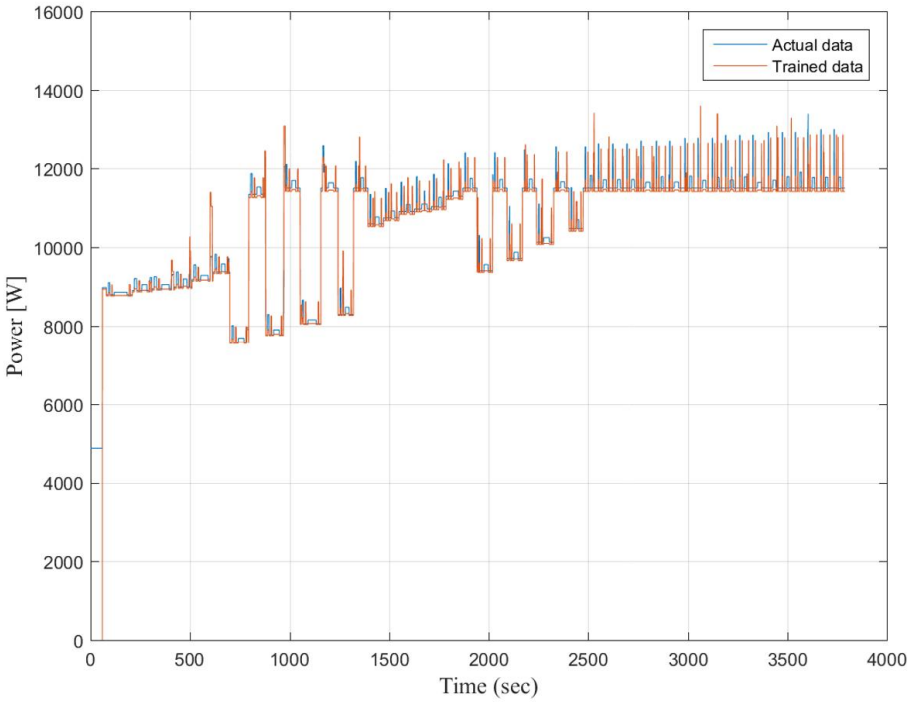

Figure 46. Results of trained ANN

Table 4. Summary of simulation results

Number of iteration	640,274
Total time	3 min
Energy consumption (Actual)	665.389 kWh
Energy consumption (Trained)	656.994 kWh
Error	**1.28%**

3.7 Summary

An energy consumption model was investigated and modeled with process parameters. The proposed model showed high accuracy and a simulator was implemented. Moreover, a physical model-based ANN was proposed and training results fit the actual results well.

4 Energy model for renewable energy and manufacturing processes

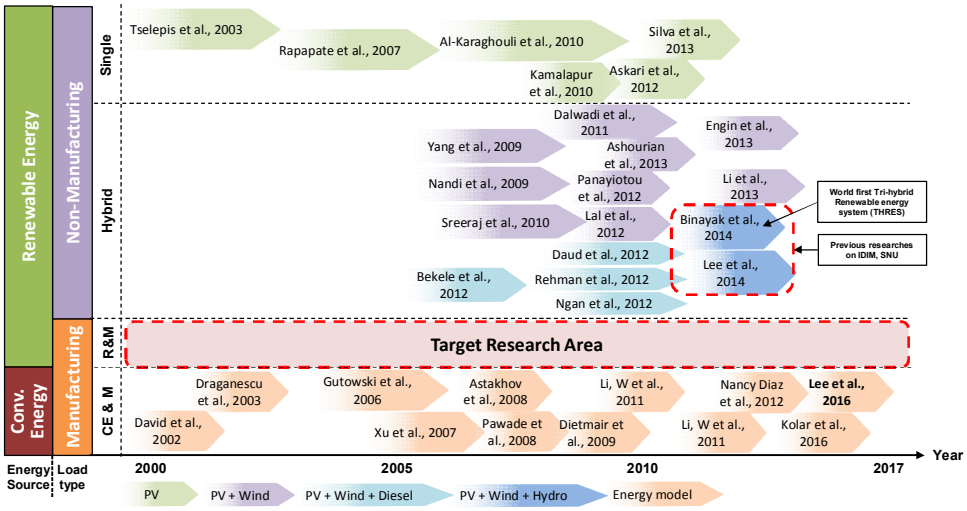

Figure 47. Previous research on renewable energy and load conditions

The load conditions of a renewable energy system are important. In previous research of renewable energy systems, load conditions were random, with typical applications of hospitals and accommodations [10, 16, 18, 71–80]. However, no manufacturing oriented off-grid renewable energy system has been studied, as shown in Figure 47.

Thus, a manufacturing-oriented renewable energy model was proposed and simulated with actual experimental data. A primary disadvantage of renewable energy is random output characteristics due to random input variables, such as sunrays

and wind speed, so a manufacturing-oriented model was proposed and used for estimating not only the failure rate but also the scale effect of a renewable energy plant for operating manufacturing facilities.

4.1 Overview

Mathematical models of renewable energy sources and manufacturing energy consumption were investigated and implemented. Each of the equations was implemented in Matlab to simulate operating conditions. An overall simulation flow chart is shown in Figure 48. The main purpose of a manufacturing-oriented renewable energy simulation is to estimate the stability of a renewable energy system with manufacturing processes and provide scale effects of renewable energy systems. In this research, the target components of a renewable system include PV arrays, wind turbines, and a battery bank. Input variables are monitored by an off-grid monitoring platform.

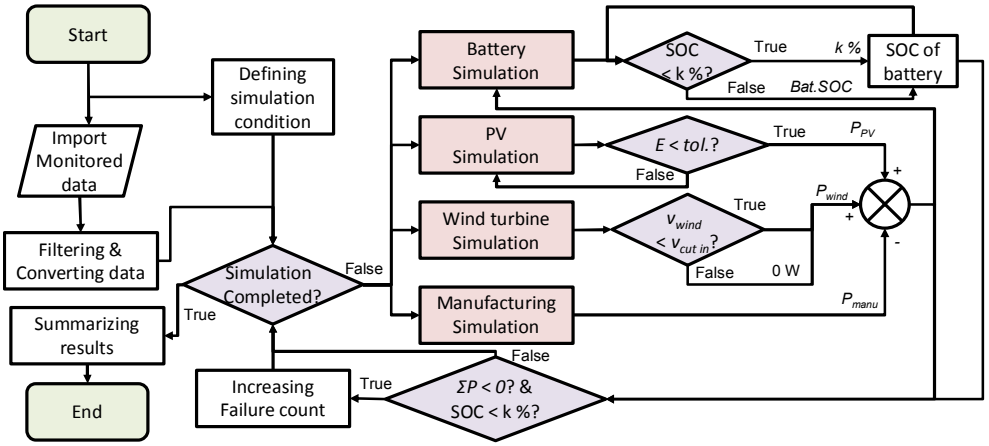

Figure 48. Flow chart of manufacturing-oriented renewable energy simulation

4.2 Assumptions of models

Before modeling a manufacturing-oriented renewable energy system, three assumptions should be defined first. The first assumption is energy conservation of renewable energy generation and manufacturing energy consumption. The amount of energy generated from renewable energy sources is equal to the sum of stored energy in batteries and energy consumption for the load. The main controller and inverter consume little amounts of energy and the battery has self-discharge characteristics. Additionally, wires also consume a small amount of energy when the current flows. However, the amount of energy consumed by these components is relatively low such that the energy losses from the controller, inverter, and wires are negligible.

The second assumption is that there is no degradation effect in short-term operation. There are several degradation models for renewable energy systems. Although there is a degradation effect on each component, process stability in a manufacturing system is crucial so that monitoring and predicting failure within a week is a sufficient period of time. Additionally, the

purpose of this research is an instantaneous stability estimation for a manufacturing-oriented model such that degradation factors are negligible.

The third assumption is that the battery bank is fully charged in the first state of operation. The SOC of the battery bank is calculated by integrating the current flow of the battery. Thus, there should be integrating constants for the initial condition of the battery. Therefore, the battery is fully charged in the first state of operation and for verification of modeling results, the recharging period was at least 3 days and collecting data and determining the fully charged battery for the test bed.

4.3 Generalized load condition

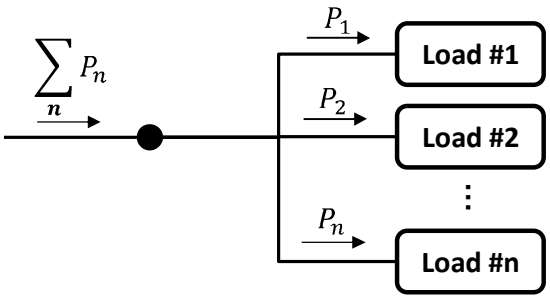

$$\int (\eta_{pv} P_{pv} + \eta_w P_w) dt + \int \eta_b P_b dt = \int P_{manu} dt$$

Kirchhoff's rules

$$\int (\eta_{pv} P_{pv} + \eta_w P_w) dt + \int \eta_b P_b dt = \int (\sum P_{\boldsymbol{n}}) dt$$

$\boldsymbol{n}$ **= number of electric load**

Figure 49. Schematics of generalized load condition

To calculate various types of load conditions, Kirchhoff's rule was implemented on the power consumption side. Figure 49 shows Kirchhoff's rules for various conditions for this research. Even for an AC load condition with resistive and inductive loads, the load condition can be estimated as the summation of individual loads.

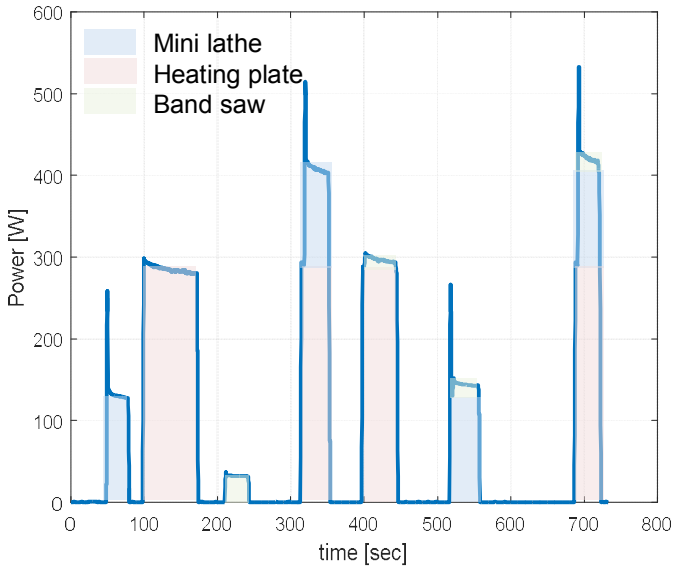

Figure 50. Experimental results of various load conditions

The mini lathe and band saw, as inductive load conditions, and a heating plate, as a resistive load condition, were investigated to confirm generalized load conditions. Each facility can run not only individually but also in combination. Figure 50 shows that Kirchhoff's rule was confirmed in this study. A summary of various load conditions is provided in Table 5. Thus, a combination of various types of electric load can be considered and individual electric loads can be combined with Kirchhoff's rule.

Table 5. Summation of various load conditions

Experiment Condition	*Average Power [W]*	*Summation [W]*
Mini Lathe	*128.5*	-
Heater	*279.4*	-
Band Saw	*31.4*	-
Lathe + Heater	*408.7*	*407.9 (= 128.5 + 279.4)*
Heater + Band saw	*304.9*	*301.8 (= 279.4 + 31.4)*
Lathe + Band saw	*152.1*	*159.9 (= 128.5 + 31.4)*
Lathe + Heater + Band saw	*424.8*	*439.3 (= 128.5 + 279.4 + 31.4)*

4.4 Test bed for model

An off-grid renewable energy test bed was installed at SNU, Seoul. In total, eight PV arrays and a 400-W wind turbine were installed (Figure 51). An off-grid monitoring platform was also installed at the test bed. Hardware for the test bed differed from the monitoring hardware in Nepal because different numbers of sensors were applied in this case (Figure 52).

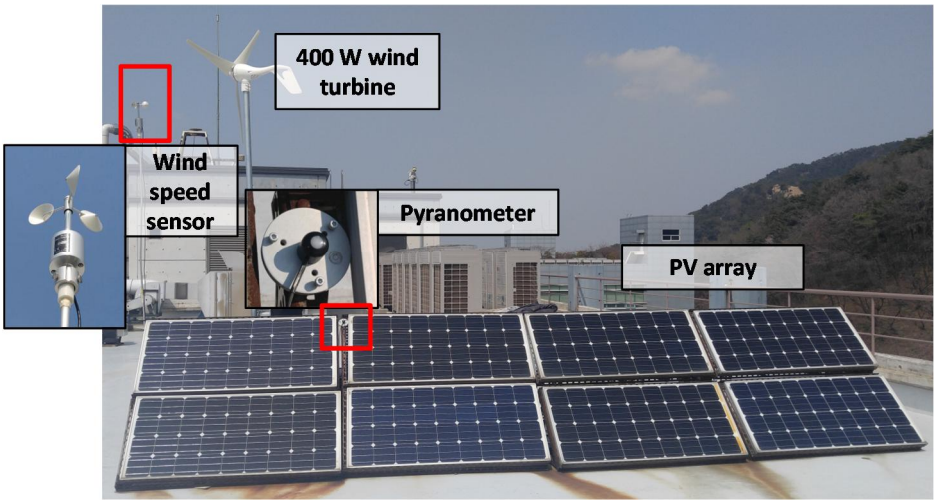

Figure 51. Off-grid renewable energy testbed in SNU

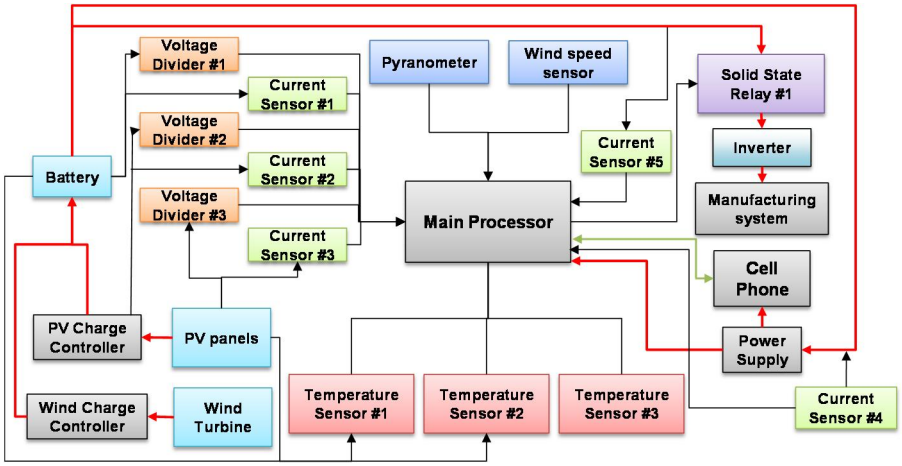

Figure 52. Hardware block diagram for off-grid testbed in SNU

The detailed specifications of the off-grid energy test bed at SNU are described below.

Table 6. Solar panel specifications

Model name	*SSP-120D*
Rated Power (P_{max})	*120 W*
Short circuit current (I_{sc})	*7.63 A*
Open circuit voltage (V_{oc})	*21.75 V*
Rated current (I_{pv})	*6.89 A*
Rated voltage (V_{pv})	*17.4 V*
Battery charging voltage	*12 V*
Crystalline	*Multi*
Size	*1484 × 669 × 35 mm*

Table 7. MPPT solar charge controller specifications

Model name	*Tracer-4215BN*
Rated voltage	*12/24 V (Auto work)*
Charge algorithm	*Maximum Power Point Tracking*
Rated charge current	*40 A*
Maximum battery voltage	*32 V*
Maximum PV input voltage	*150 VDC*
Maximum PV input power	*520 W (12 V) / 1040 W (24 V)*
Self-consumption	*≤ 50 mA (12 V) / ≤ 27 mA (24 V)*

Table 8. Wind turbine specifications

Model name	*FA24V-400*
Rated Power	*400 W*
Rotor diameter	*1.2 m*
Start-up wind speed	*2 m/s*
Yaw mode	*Fixed-wing*
Rated voltage (V)	*24 V*
Shell material	*Die-cast aluminum*
Blade material	*High-strength nylon composite*
Motor type	*Single-phase permanent magnet DC generator*

Table 9. Battery specifications

Model name		*ESH40-12*
Nominal Capacity (AH)		*40 Ah*
Nominal Voltage (V)		*12 V*
Dimensions (L × W × H × TH) (mm)		*197 × 165 × 170 × 170 mm*
Weight (kg)		*12.8 kg*
Internal Resistance (mΩ)		*10.5 mΩ*
Charge voltage (@ 25℃)	*Cyclic use (V)*	*14.40 V*
	Standby use (V)	*13.32 V*

4.5 Modeling results

First, energy conservation should be verified. A PAC3200 (Siemens) power meter was installed in the AC power line. Customized power measurement software was developed with LabVIEW. The PAC3200 is capable of communicating with a TCP/IP-based Modbus protocol so that power information can be obtained anywhere.

As shown in Figure 53, the sum of power generation from the renewable power plant and power demand trends of the manufacturing device were matched. This result is evidence of

energy conservation in the system.

Failure of the off-grid system was detected at 22 V in the battery bank (Figure 54). The SOC was also calculated for the battery model with current measurement data (Figure 57). Thus, criteria for failure modes can be estimated with the SOC of the battery bank.

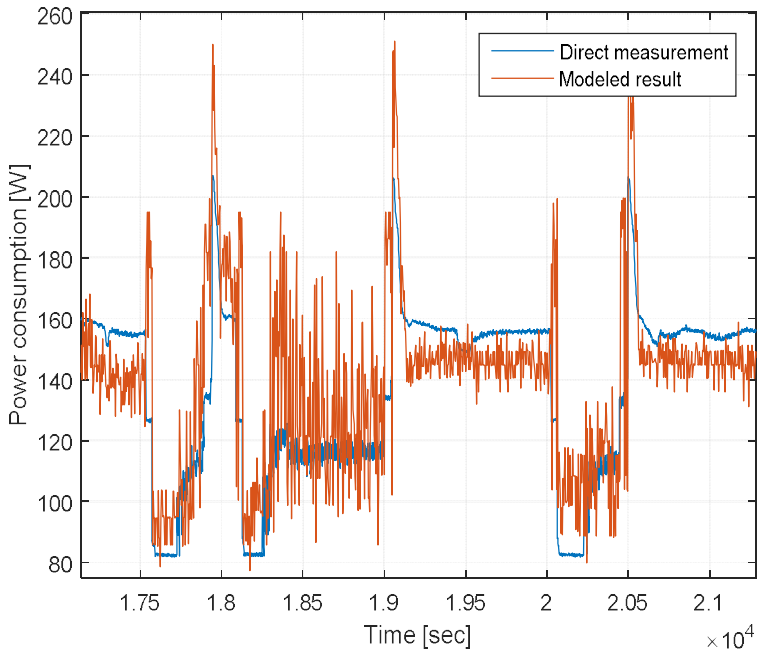

Figure 53. Power trends of direct measurement and modeled results

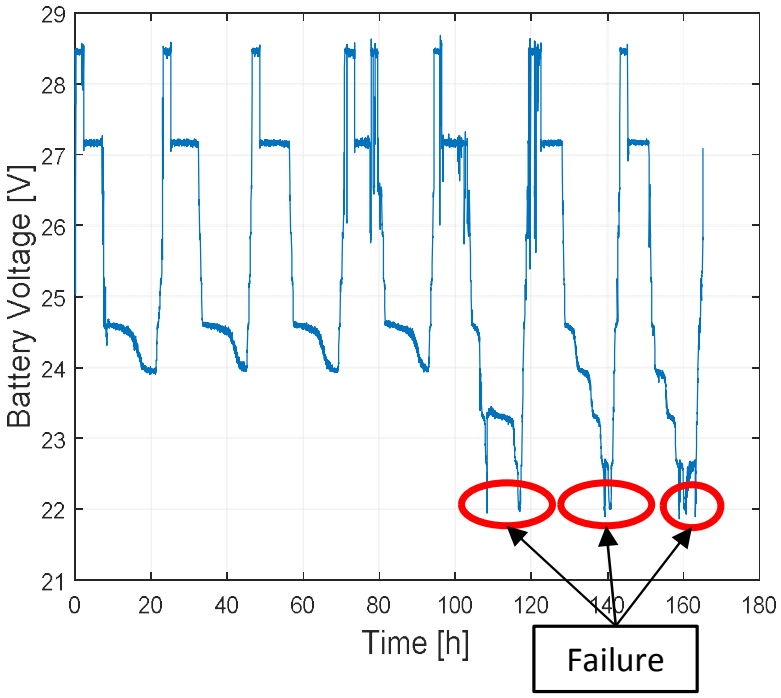

Figure 54. Results of monitored voltage of battery bank (actual results)

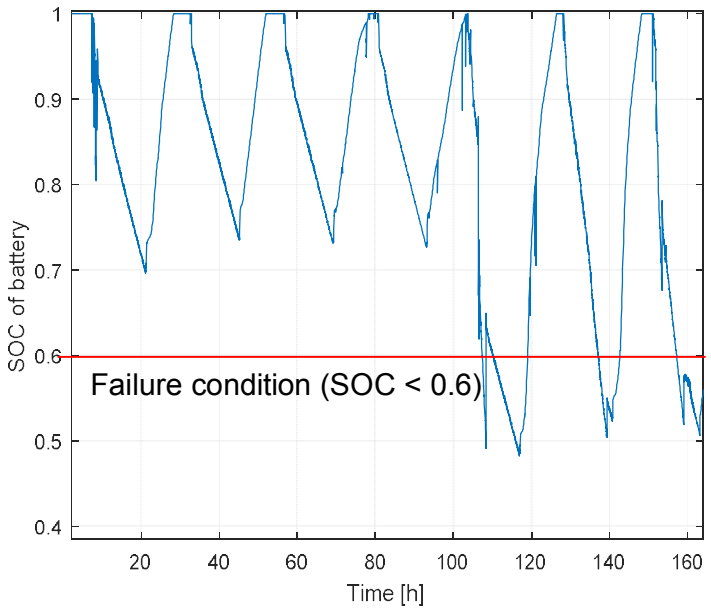

Figure 55. Results of monitored SOC of battery bank (actual results)

4.5.1 Case study 1: 3D Printer

To measure stability of the off-grid renewable energy system with manufacturing processes, a simple target specimen was designed (Figure 56). The target manufacturing process is a three dimensional (3D) printer (3Dwox DP200, Shindoh Corp.). Detailed specifications of the 3D printer are described in Table 10.

NC code was automatically generated by the provided CAM software. To obtain operating conditions, interpreter software was developed. Results of the interpretation of the NC code for position information are shown in Figure 57.

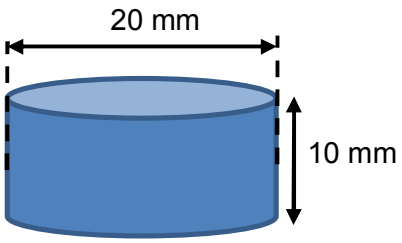

Figure 56. Dimensions of the test specimen

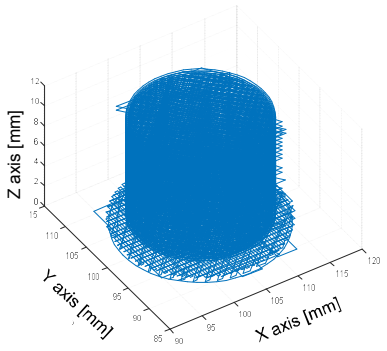

Figure 57. Operating position of manufacturing of target specimen

Table 10. Specifications of 3Dwox DP200, Shindoh Corp

Model name	*3DWOX DP200*
Material	*PLA, ABS*
Layer thickness	*0.05–0.4 mm*
Nozzle size	*0.4 mm*
Rating power	*150 W*
Support file	*.stl, gcode*

The power trend for a fabricated test specimen is shown in Figure 58. To simulate the stability of the off-grid renewable energy system, the simulator assumes that the manufacturing process, the 3D printer, continuously fabricates the target specimen.

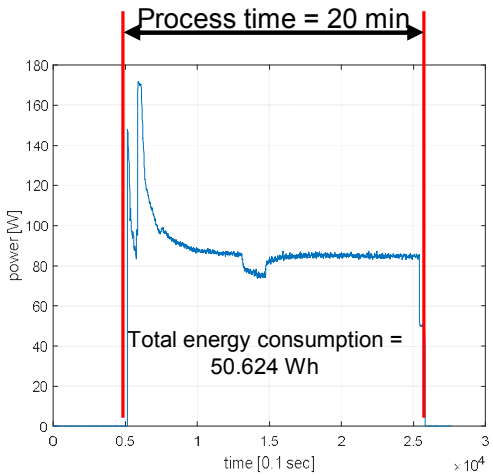

Figure 58. Power trends of a three dimensional (3D) printer to fabricate a target specimen

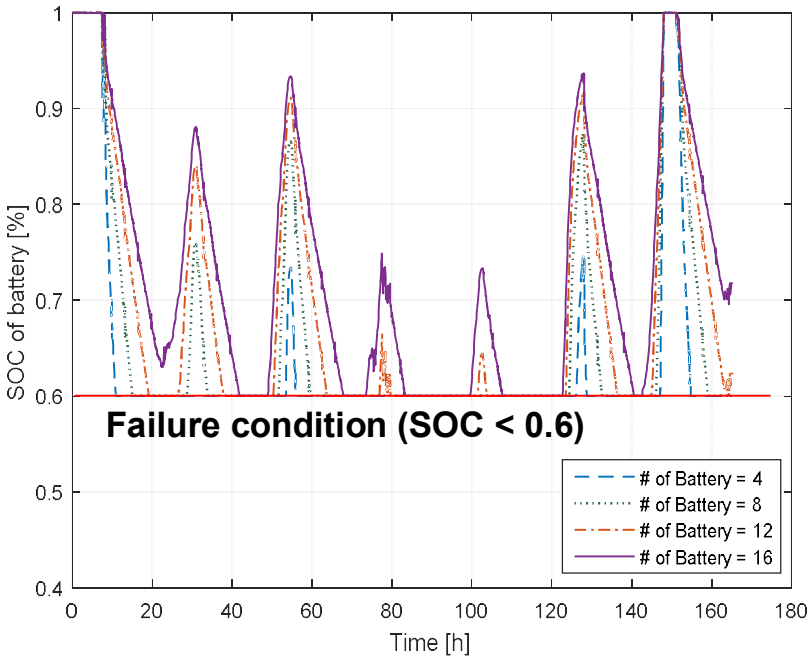

Figure 59. SOC result with six PV arrays and two wind turbines

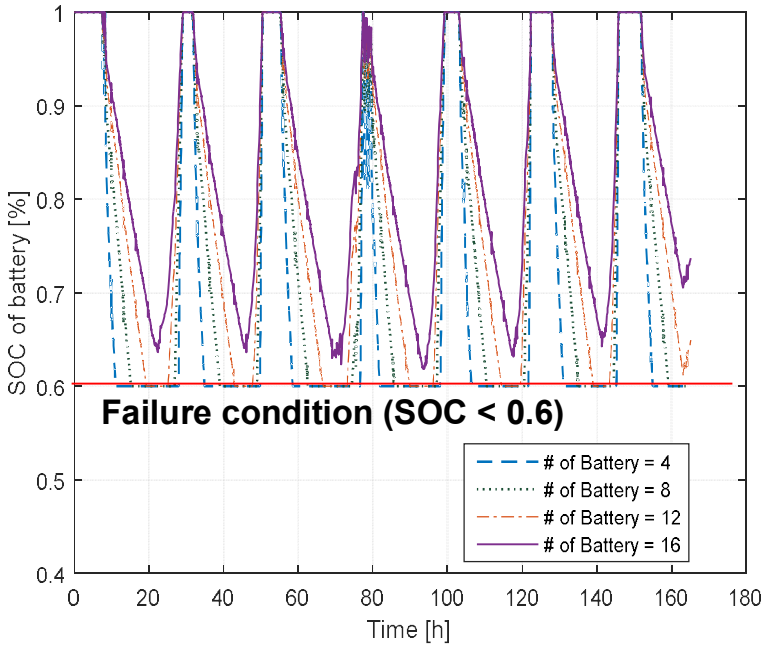

Figure 60. SOC results with ten PV arrays and two wind turbines

An SOC-based simulation was conducted and two major simulation results are shown in Figure 59 andFigure 60. In the case of six PV arrays and two wind turbines, even when the number of battery banks was increased from 4 to 16, failure occurred. However, as the number of PV arrays increased from 6 to 10, stability of the whole system increased.

Based on the modeling results, the failure rate can be calculated as follows:

$$\textbf{\textit{Failure rate}} = \frac{\textbf{\textit{Unstable operating time}}}{\textbf{\textit{Total operating time}}}$$

Overall stability of the off-grid manufacturing system is correlated with the incoming power source (solar irradiation, wind speed), scale of the renewable energy system, and capabilities of the battery bank. Wind speed varies with the installation location of the wind turbines. Thus, wind speed is varied by multiplying wind speed data to observe the effects of natural energy sources.

The failure rate indicates the stability of the whole system; if the failure rate reaches 0, it means it exhibits stable around-the-clock operating conditions for the manufacturing process. However, if the manufacturing process is fixed, an appropriate scale of the renewable energy system is present, and if the manufacturing parameters are controlled, the surface of the failure rate would approach 0, so that the minimum requirements for the renewable energy system scale decrease, which means a minimal-scale renewable energy system could be used with manufacturing facilities.

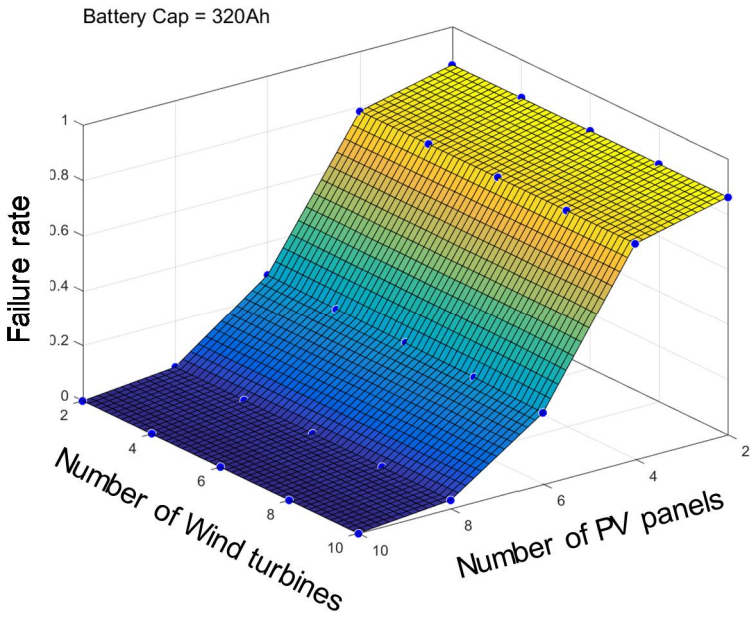

Figure 61. Surface of failure rate *vs.* scale of renewable energy system (@ $1 \times v_{wind}$)

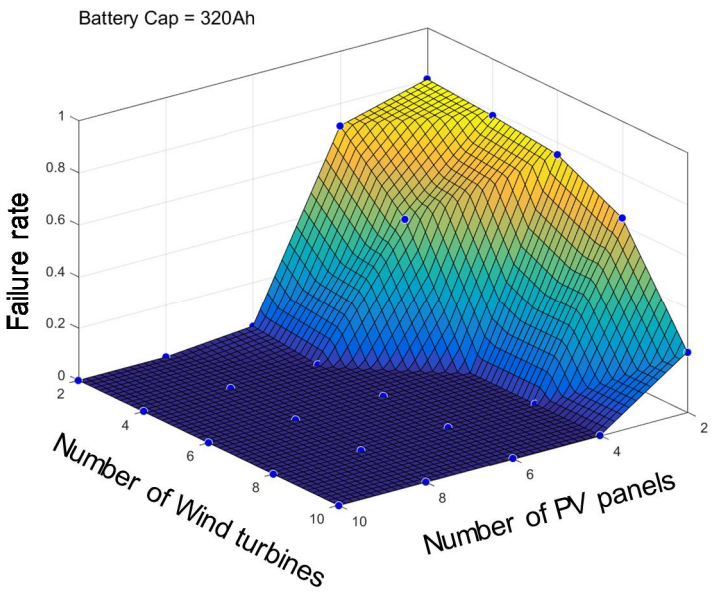

Figure 62. Surface of failure rate *vs.* scale of renewable energy system (@ $3 \times v_{wind}$)

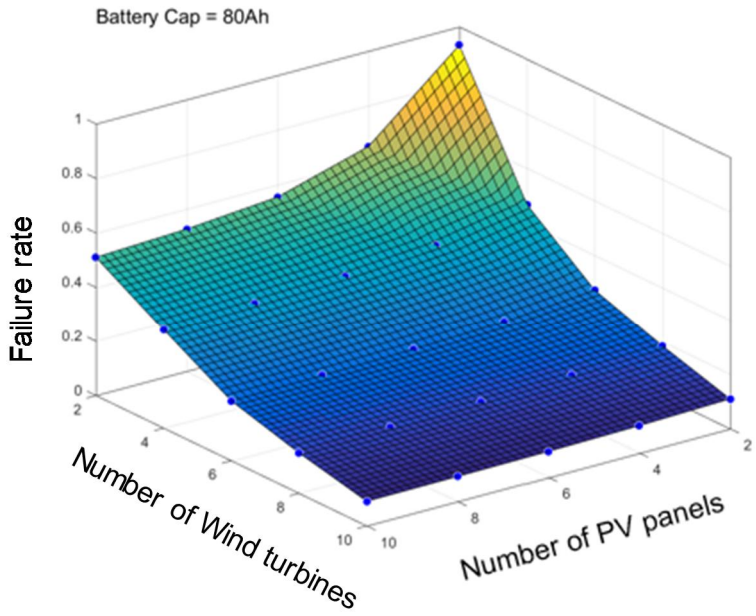

Figure 63. Surface of failure rate *vs.* scale of renewable energy system (@ $5 \times v_{wind}$)

With the modeling results, a manufacturing-oriented off-grid system was designed (960 W of a total of eight PV arrays, two in series, four in parallel; 320 Ah at 24 V for a total of eight batteries, two in series and four in parallel; and a 400-W wind turbine), installed, and operated with the same manufacturing process from April 20- 26. Energy conservation was verified with direct measurement data and modeled (Figure 64).

With the modeling results above, the estimated failure rate of the redesigned system was 0.033 (Figure 65). Operating

conditions were monitored with an off-grid monitoring platform installed at SNU (Figure 52). Figure 66 and Figure 67 show that the redesigned off-grid system with the manufacturing process did not fail. The error in the estimated failure rate versus the actual results was caused by preparation time.

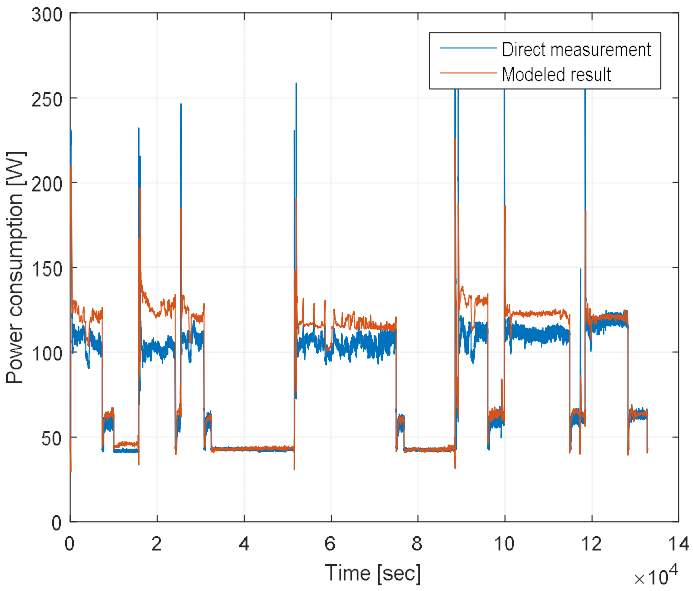

Figure 64. Verification of energy conservation in the redesigned off-grid system

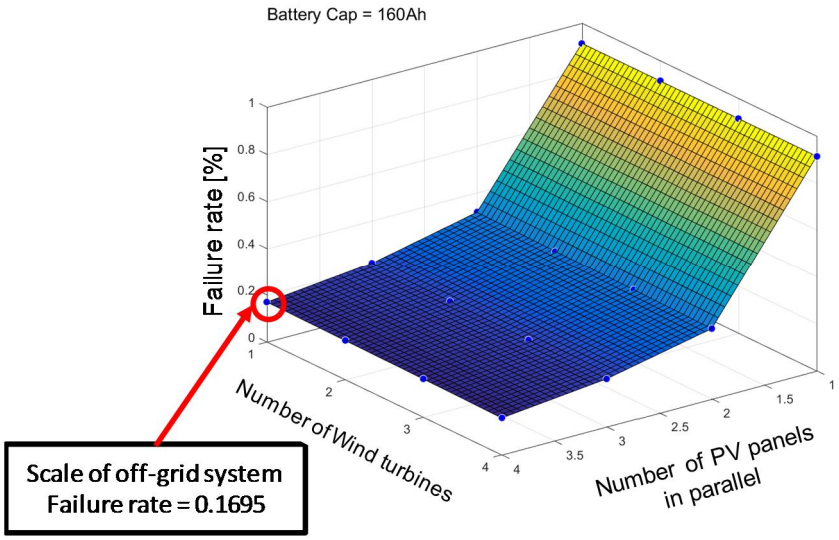

Figure 65. Failure rate of redesigned off-grid system with a manufacturing process

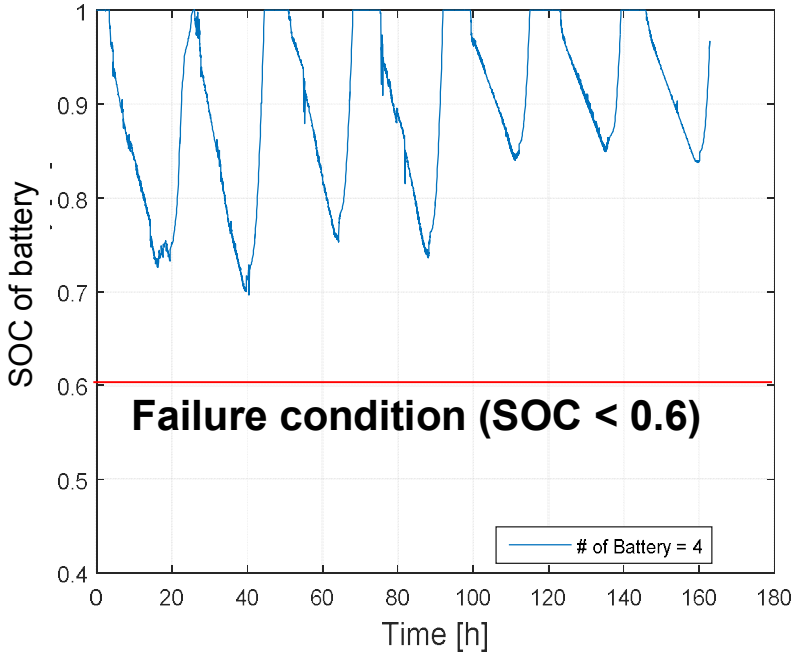

Figure 66. SOC results of eight PV arrays, one wind turbine, and eight batteries

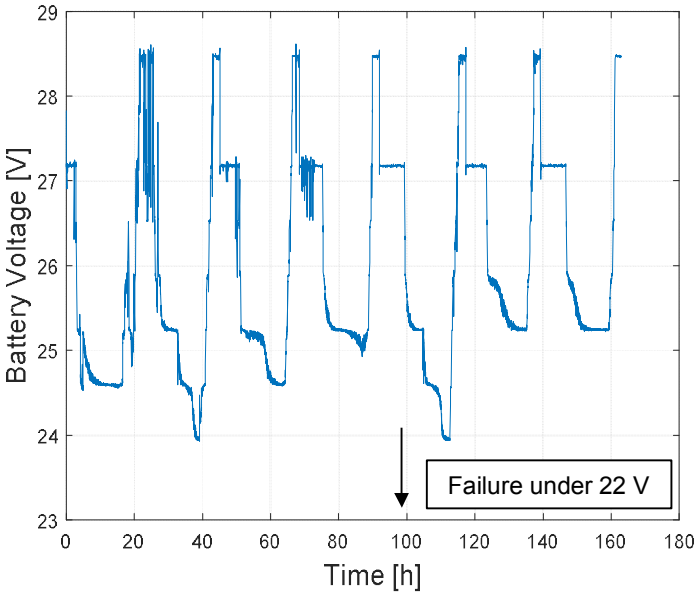

Figure 67. Results of battery bank voltage (actual data)

4.5.2 Case study 2: Lathe

Similar to the first case, the lathe is the second case for a larger-scale manufacturing system. The target lathe machine is a NL2000SY and its power profile was simulated with the time-wise simulator proposed in Chapter 0. The manufacturing procedure is described in Figure 68.

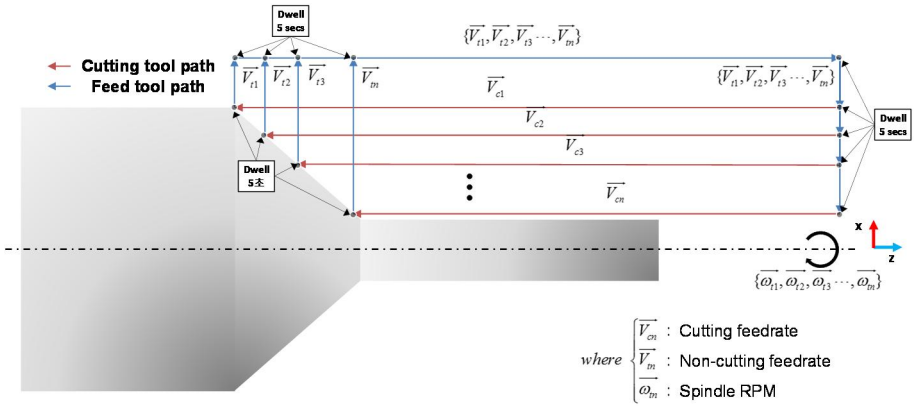

Figure 68. Process procedure for case study: the lathe

The failure rate surface was calculated with the simulation results. Because of the scale of the manufacturing process, the minimum requirement scale for the renewable energy system is much larger than in case 1. As shown in Figure 69, the capacity of the battery was 8,000 Ah with 200 PV arrays for the renewable energy system to reach a failure rate of almost 0.

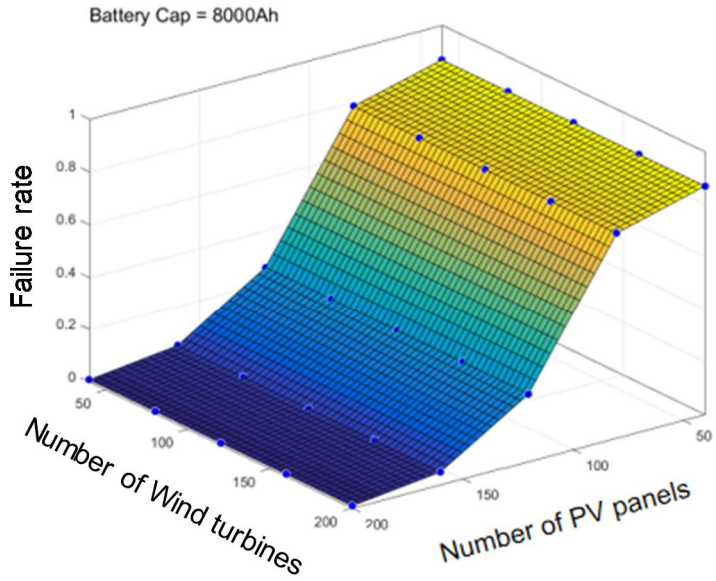

Figure 69. Surface of failure rate *vs.* scale of renewable energy system (@ $1 \times v_{wind}$)

If the wind speed is multiplied by 3, the surface of the failure rate is changed and the required capacity of the battery bank is reduced.

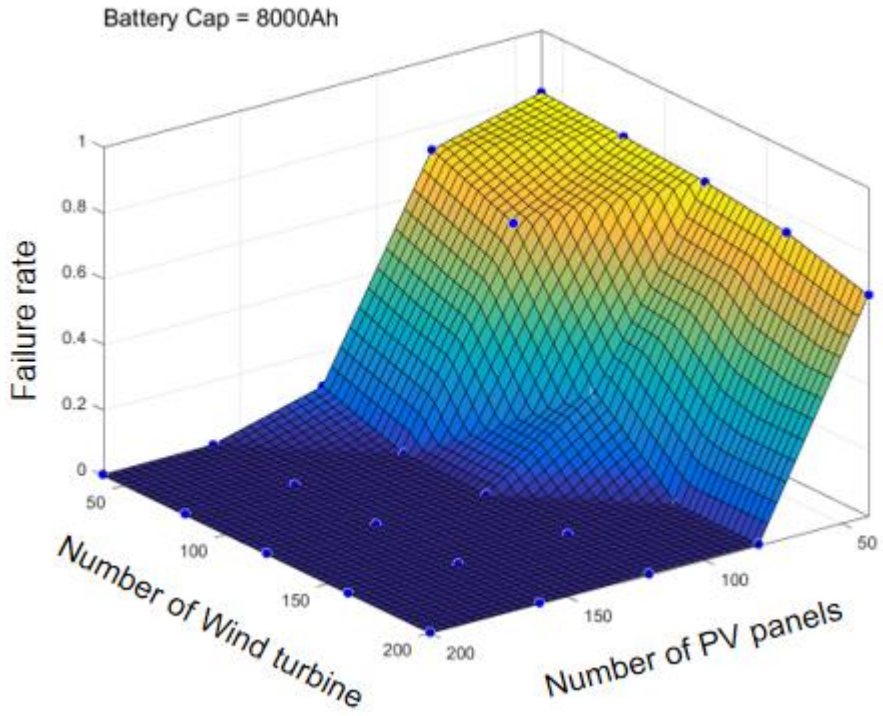

Figure 70. Surface of failure rate *vs.* scale of renewable energy system (@ $3 \times v_{wind}$)

A larger manufacturing process requires a large-scale off-grid renewable energy system. Peak demand is also a key factor because a larger current flow will induce a larger discharge of the battery bank.

4.5.3 Case study 3: Band saw

A band saw is a simple manufacturing tool that is capable of fabricating simple two dimensional (2D) parts. An off-grid renewable energy system would typically be installed in a rural area of a developing country so a simple manufacturing facility should be considered. Thus, the band saw is a good candidate for analysis.

Nine repeat cuts of a 1-mm thick acrylic plate were performed with an off-grid renewable system (Figure 71). The simulation result showed that a 240-W PV array, 400-W wind turbine, and a 120 Ah battery bank system would be required for continuous cutting processes with the band saw (Figure 72).

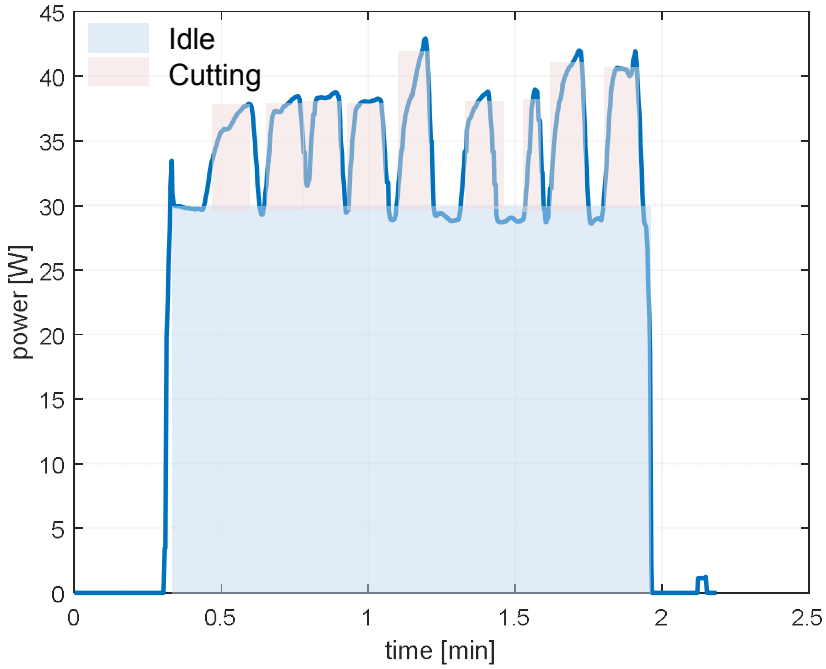

Figure 71. Power demand profile of the acrylic plate cutting process

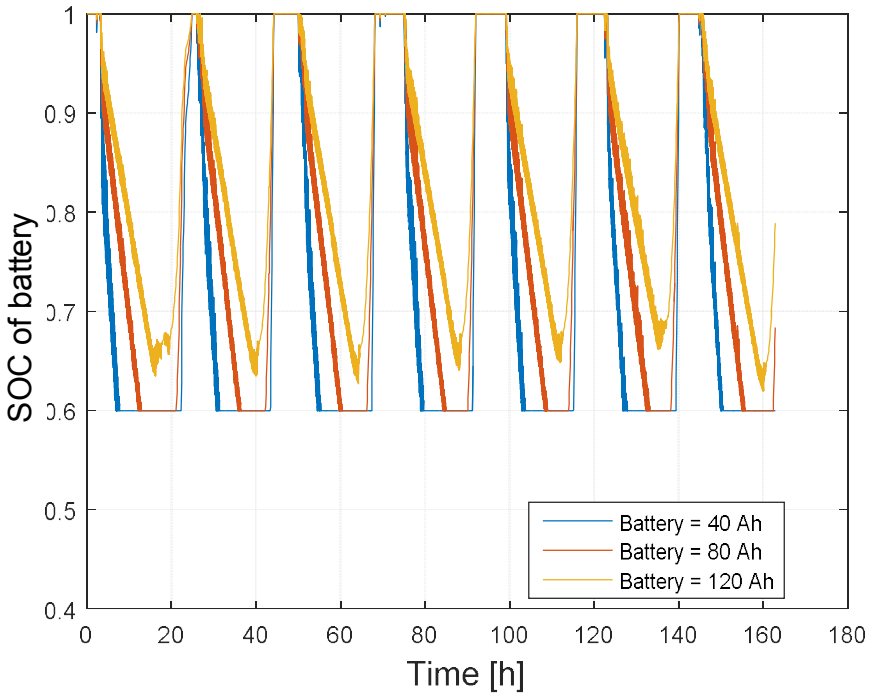

Figure 72. Simulation results of an off−grid renewable energy system with a band saw

4.5.4 Case study 4: Vaccine carrier

A vaccine carrier can have a large impact in developing countries. However, some countries do not have the infrastructure for electricity so an active-type vaccine carrier was developed as a practical example of an off-grid renewable system. A vaccine carrier is a good example for estimating the stability of an off-grid energy system.

Recently, cold-chain procedures were proposed for delivering vaccines farther than a single vaccine carrier. Cold-chain requires stable electricity so that the proposed model can estimate the stability of the whole system with multiple vaccine carriers. The vaccine carrier consists of the cooling part, the Peltier module. In this research, the power demands of a single Peltier-type vaccine carrier were measured and a simulation method was used to estimate the stability of an off-grid system with a vaccine carrier.

Figure 73 shows the power demands of the vaccine carrier in two states: cooling on and off. A stable-size off-grid renewable energy system for cold chain storage in rural areas for vaccine carriers requires a 360-W PV array, a 400-W

wind turbine, and 160 Ah of battery bank capacity (Figure 74).

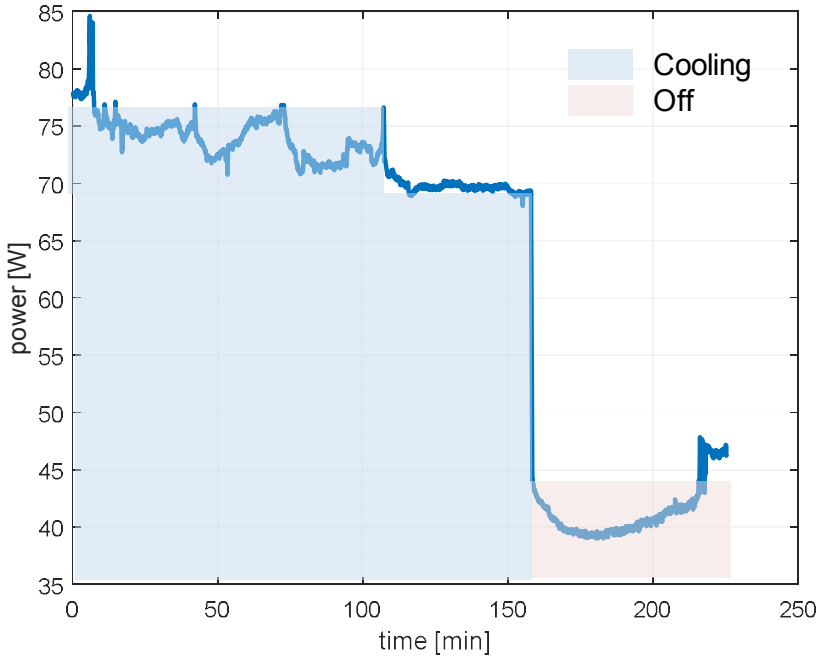

Figure 73. Power demand profile of a vaccine carrier with cooling on *vs.* off

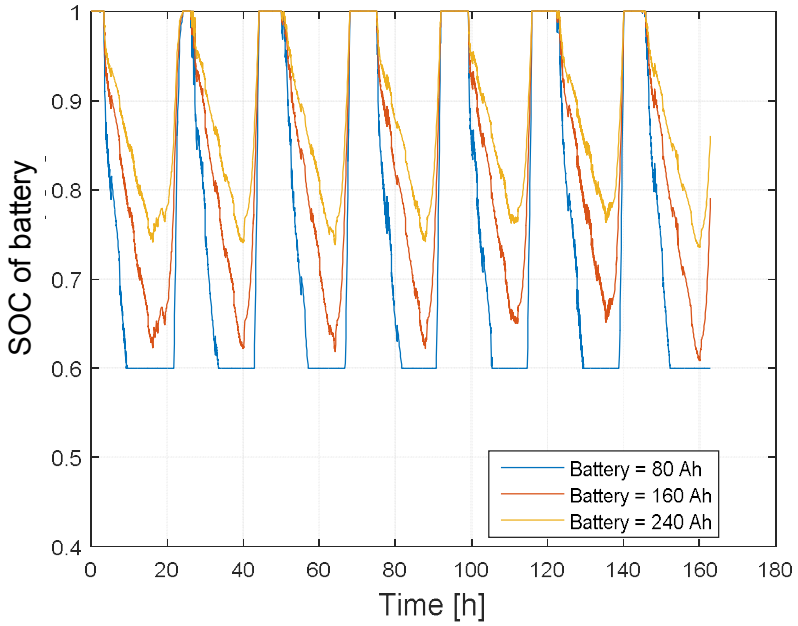

Figure 74. Simulation results of an off−grid renewable energy system with a vaccine carrier

4.5.5 Comparison with other models

Monte-Carlo-based analyses are widely used in the design of off-grid renewable energy plants for rural areas. The major merit of such a statistical analysis is that the modeled results propose the appropriate scale for various types of load conditions. However, design results based on statistical methods tend to overdesign an off-grid system.

The Monte-Carlo method examines several samples and generates random input variables. An even load condition is generated randomly and power generation can be calculated simultaneously. Accommodating load conditions can be modeled with statistical methods so that the Monte-Carlo simulation fits in randomized load conditions [81].

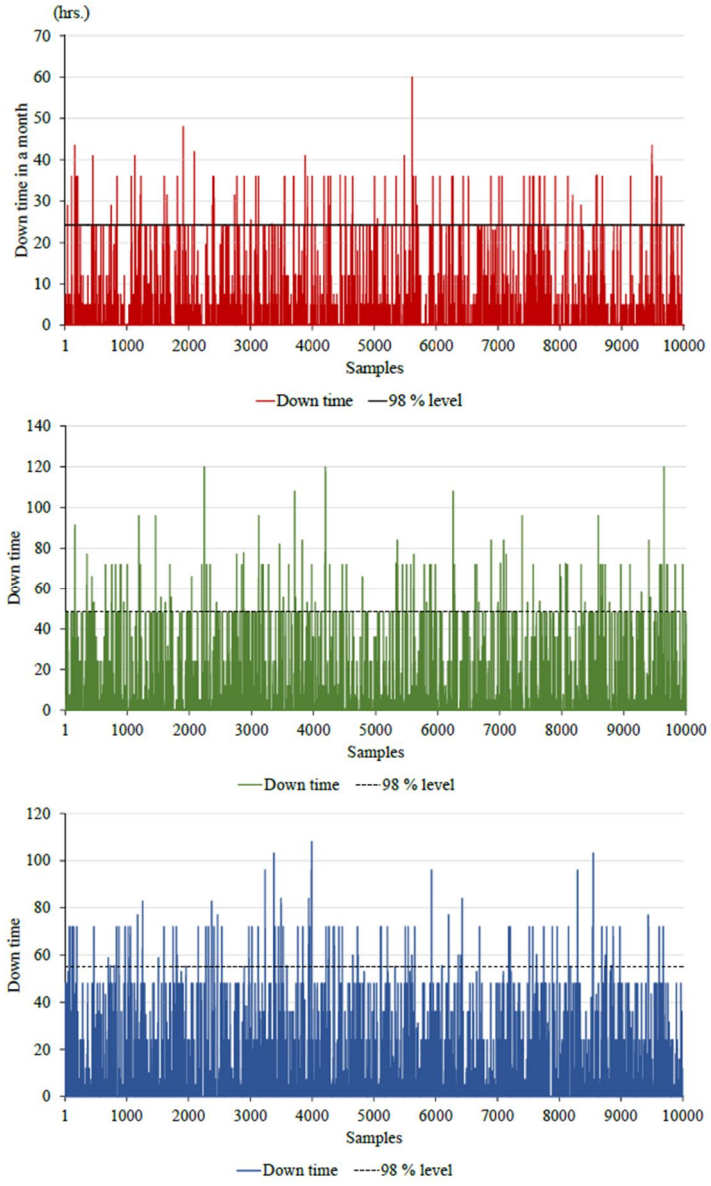

Figure 75. Monte Carlo analysis of a PV/wind/hydro system [81]

As shown in Figure 76, the HOMER model provides statistically based load conditions. The electric load can be defined at 1-h intervals and load conditions can be generated randomly. Bhandari's and Lee's models use statistically based load conditions.

Figure 76. Load condition example in HOMER Pro

Figure 77 shows HOMER model results. The unit scale of the wind turbine is 400 W. The size of the PV panel is 2.01 kW, one wind turbine, and 360 Ah of battery capacity. The target

location was Building 312, Seoul National University. Temperature and solar irradiation data were imported into HOMER Pro.

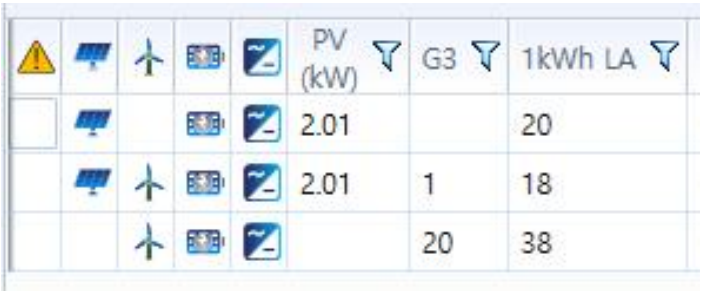

					PV (kW)	G3	1kWh LA
					2.01		20
					2.01	1	18
						20	38

Figure 77. Optimal results obtained with HOMER Pro

Comparison results are shown in Table 11. The results of the time-wise model were a 1.2-kW PV panel, a 400-W wind turbine, and 320 Ah of battery capacity. The time-wise model results are lower than the statistical result. Load conditions were monitored and modeled. Because the load condition was modeled in the time domain, unnecessary conditions are not considered so that the design result is smaller than the statistical model with the same stability.

Table 11. Comparison result of HOMER and time-wise model.

Case	HOMER Model	Time-wise Model	Comparison

PV	2,010 W	1,200 W	-500 W [-40.3%]
Wind	400 W	400 W	0 W
Battery	360 Ah	320 Ah	-40 Ah [-12.5%]

4.6 Summary

A manufacturing-oriented simulation method was introduced and the simulation was compared with actual monitored data. A data set was provided to the off-grid monitoring platform and the stability of the whole system was calculated. Two manufacturing processes were investigated as case studies and failure rate surfaces were calculated. Moreover, a statistical model widely used in off-grid systems is used to perform a comparison with the modeling results.

Various load conditions for the off-grid system were analyzed with the proposed simulation method. In total, four cases of load conditions were considered: a 3D printer, a large-scale lathe, a band saw, and a vaccine carrier. Four practical cases of load conditions were measured and simulated and the stable system size for each condition was obtained.

Furthermore, the proposed model was compared with a statistical model, the HOMER model, to show that the time-wise simulation method has value in designing an off-grid system. With the same rating load conditions in both models, the proposed model obtained a smaller scale off-grid system. Moreover, peak demand could be considerable within a few seconds.

5 Conclusions

Emerging problems with energy generating sources have grown since the era of the industrial revolution. Global warming has been realized as a problem and the ‘climate crisis’ has accelerated. Furthermore, in developing countries, renewable energy systems are used widely and the energy consumption ratio of renewable energy has increased. From the point of view of manufacturing industries, the largest portion of energy consumption in South Korea, renewable energy is not attractive because of the unstable characteristics of energy sources (e.g., solar radiation, wind speed). Thus, monitoring of renewable energy systems is crucial in predicting their stability.

For developing countries, real-time off-grid renewable energy monitoring systems for rural areas have not been developed. As such, an SMS-based real-time monitoring platform was developed and installed in a developing country, Nepal.

To further investigate the stability of renewable energy systems, a manufacturing-oriented energy system was

introduced and a simulation method was developed. An off-grid renewable energy test bed was installed in SNU, Seoul, and two manufacturing cases were investigated. From small to large scale manufacturing processes, an SOC-based simulation method was implemented and the failure rate with a monitored data set and manufacturing energy consumption simulator were calculated. Finally, a scale effect of the renewable energy system could be obtained based on manufacturing processes with an off-grid monitoring platform and could provide stability of the renewable energy system with regard to the manufacturing processes examined.

Appendix

Monitoring system for a renewable energy system

On-grid energy monitoring systems are widely used because fully functioning infrastructures have already been implemented [82-85]. Thus, a monitoring system with an on-grid system uses high-speed communication protocols. Due to the large bandwidth in communication capability, a large data set can be transmitted and analyzed with high-performance hardware. A high-speed data acquisition rate supports a high level of stability in controlling a target system [86, 87].

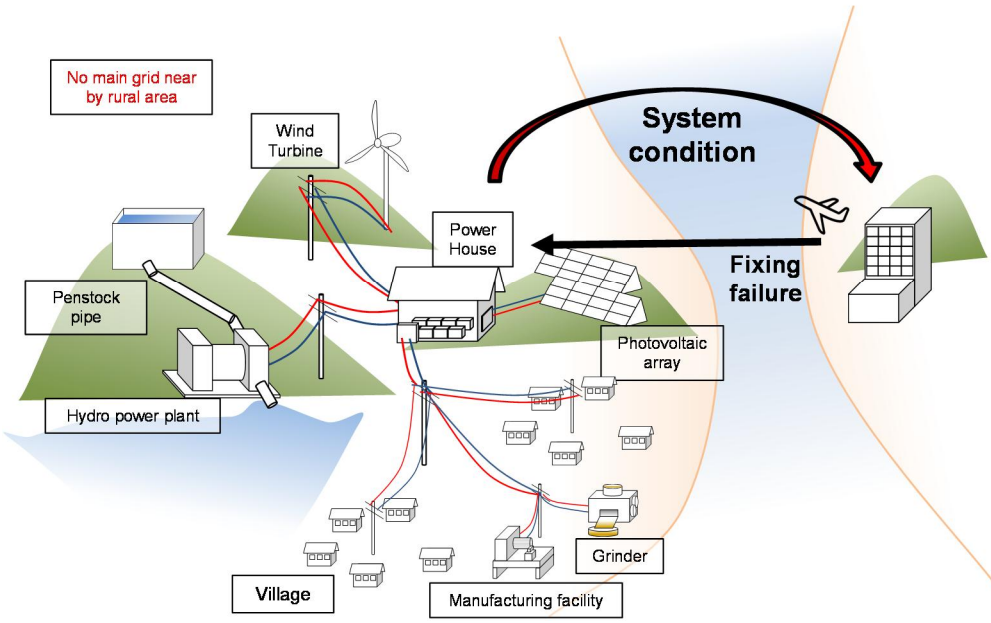

Figure 78. Issues in an off-grid renewable energy system

In the case of an off-grid renewable energy monitoring system, the impact is much larger than with an on-grid system. Off-grid systems are commonly installed in rural areas so the infrastructure is not necessarily fully functional. Communication capabilities are significantly lower and there are typically no trained engineers working in rural areas. If the whole system malfunctions, it can take several months to fix the problem. Sometimes, malfunctioning is not even reported for a few weeks.

Several off-grid type power systems have been installed in several different countries. Stand-alone PV power systems [24, 88-93], PV/wind power systems [15, 16, 18, 63, 74, 94-98], and PV/wind/diesel power systems [75, 77, 99-101] have been investigated. Akikur *et al.* surveyed over 30 different off-grid rural systems [102]. The scale of an off-grid rural energy system varies with the demand load scale. Some of them have monitoring systems locally (Table 12), although an off-grid system is typically installed in a rural area and a remote monitoring system is not installed even with a large-scale energy system.

Table 12. Previous research of off-grid renewable energy systems

Study/Project location	Total annual load	Monitoring	Reference
Vadodara, India	1825 kWh/year	-	(Dalwadi et al. 2011) [94]
Juara village, Tioman island, Malaysia	181.04 MWh/year	Local	(Ashourian et al. 2013) [95]
Two different sites: 1. Nice, France; 2. Nicosia, Cyprus	8760 kWh/year	-	(Panayiotou, Kalogirou, and Tassou 2012) [96]
Dalajia Island in China	13.14 MWh/year	-	(Yang, Wei, and Chengzhi 2009) [97]
Sitakuda, Bangladesh	61,685 kWh/year	-	(Nandi and Ghosh 2009) [18]
Naboualu Vanua Levu Island, Fiji	360.985 MWh/year	Local	(Lal and Raturi 2012) [15]
Sukhalai, Hoshangabad, Madhya Pradesh, India	15,768 kWh/year	Local	(Sreeraj, Chatterjee, and Bandyopadhyay 2010) [74]
Turkey	1142 kWh/year	-	(Engin 2013) [63]
Patenga, Chittagong, Bangladesh	58.4 MWh/year	Local	(Nandi and Ghosh 2010) [98]
Urumqi, China	4.015 MWh/year	Local	(Li et al. 2013) [16]

Some researchers have investigated cell phone-based data collecting technology in rural areas of Ghana and controlling simple hand pumps in Zambia [103]. As shown in the results of hand pump monitoring, even a simple monitoring method can have a huge impact.

Table 13. List of commercially available monitoring devices and SNU monitoring system

Corporation	Target Energy Source	Cloud Service	On-line monitoring	Remote control	Failure diagnosis	System control	Cost
Logic energy	P/W	◎	○	X	△	X	○
ENMAT	P/W/B	○	○	X	X	X	○
INTERPV	P/W/H	△	○	X	△	X	△
TMCC	P/W	◎	○	X	X	X	△
OpenEnergyMonitor.org	P/L	◎	○	X	X	X	○
GreenPower Monitor	P/L	◎	○	X	△	X	–
Powerdash	P	○	◎	X	△	X	–
SNU R-monitoring system	**P/W/H/L**	◎	◎	○	○	○	◎

◎: Great, ○: Good, △: Bad, X: None, -: No information.

P: PV, W: Wind turbine, H: Hydro turbine, L: Load.

Issues in data transmission via telecommunication methods

The major issues regarding data transmission via telecommunication include the communication frequencies for mobile phones. In this research, an off-grid renewable energy system was installed at Thingan and Kolkhop, in Nepal. There are three major telecommunications companies in Nepal: Nepal telecom, Ncell, and Smart telecom. The location of the target system is highlighted with a red dot in Figure 79. Communication coverage and frequencies were provided by each telecommunication service company. Nepal telecom provided the widest range of frequencies, followed by Ncell.

Table 14. Communication frequencies in Nepal

Technology	*Frequency*	*Operator*
LTE (4G)	*1800 MHz*	*Nepal Telecom*
GSM	*900 MHz/1800 MHz*	*Nepal Telecom, Ncell, Smart Telecom*
CDMA	*800 MHz/1900 MHz*	*UTL, Nepal Telecom*
WCDMA (3G)	*2100 MHz*	*Nepal Telecom, Ncell*
WiMAX	*2300 MHz*	*Nepal Telecom*

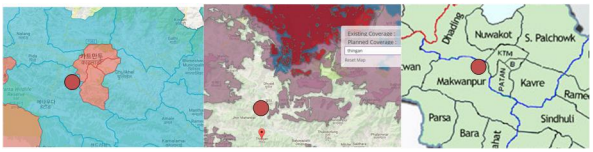

Figure 79. Communication coverage in Nepal

The cost of data transmission with SMS and multimedia messaging service (MMS) is a major issue for a monitoring system. International transmission costs of SMS are quite high so the data-transmitting interval is important. Table 15 shows detailed cost information for SMS from Nepal to South Korea.

Table 15. Detailed information of SMS cost

Item	*Quantity*
SMS cost from Nepal to Korea	*￡6*
MMS cost from Nepal to Korea	*￡12*
Max. Data length of SMS	*80*
Max. Data length of MMS	*1,000*
Currency (₩/￡)	*17.61*

From Table 15, a cost estimation surface was obtained to estimate the relationship between data interval and data length versus data transmitting costs per month. The data interval is

directly related to the cost of SMS and data length indicates the limitations of the data transmitting form.

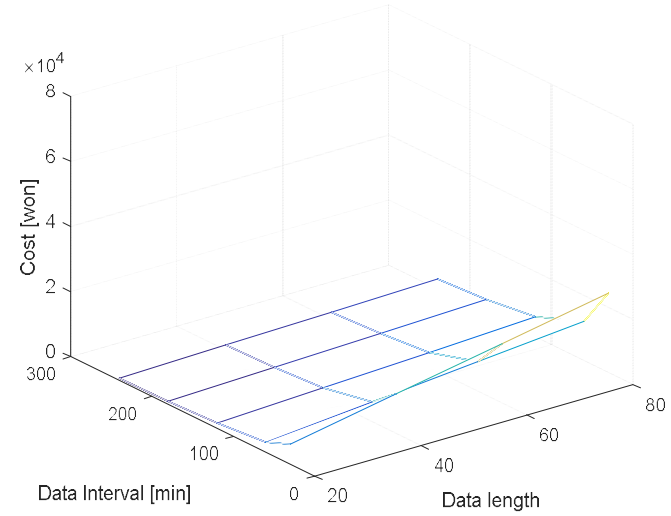

Figure 80. Cost estimate of MMS per month

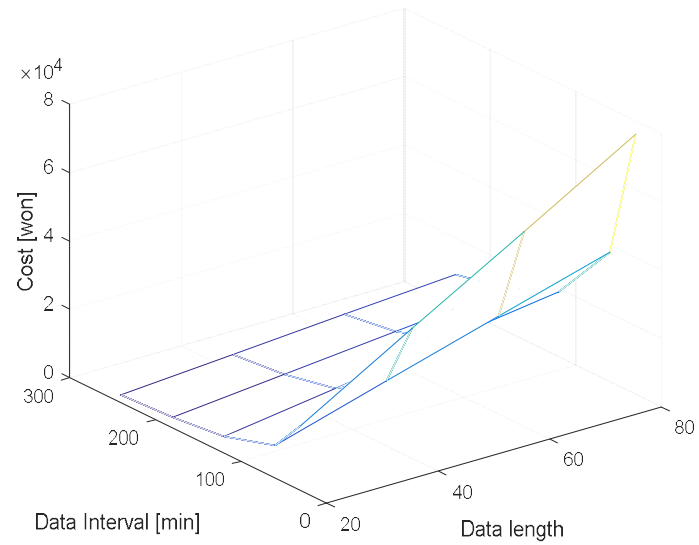

Figure 81. Cost estimate of SMS per month

Issues regarding bidirectional control

Bidirectional control is necessary for controlling an off-grid power system in a rural area. Once the telecommunication line is confirmed, bidirectional communication can be confirmed too. Because of the different interfaces between Arduino- and Android-based smart phones, customized data trimming and interrupting should be implemented in the monitoring platform. Thus, a serial communication interrupt was implemented so that a control solid state relay (SSR) was possible as soon as a control message was acquired.

Summary

Previously, there have been monitoring systems for off-grid renewable energy systems in rural areas. However, none of them could transmit data back from the rural area. Because of the lack of telecommunication capabilities in these areas, a primitive telecommunication service was investigated to overcome difficulties in the transmission of data from rural areas. A target off-grid energy system was installed in

Thingan, Nepal, and telecommunication capabilities were investigated and we estimated the cost of data transfer. Finally, telecommunication capabilities were confirmed and the capabilities of the monitoring device were defined.

Objectives

Based on previous research and commercially available devices, it is worth developing a monitoring platform capable of transmitting data in real time from a rural area. An off-grid system should be monitored in real time and the stability of the target system should be estimated.

Thus, the research objectives were 1) to develop an off-grid monitoring platform, 2) develop a renewable energy model for estimating the stability of the off-grid energy system, and 3) develop a manufacturing-oriented model and verify the stability of the off-grid energy system with some manufacturing process examples.

Development of an off-grid energy monitoring platform

Overview

The main purpose of a monitoring platform is to monitor the operating conditions of an off-grid renewable energy system in a rural area. An off-grid system is typically installed in a rural area of a developing country, so the minimum requirements are important in reducing the cost of the whole system.

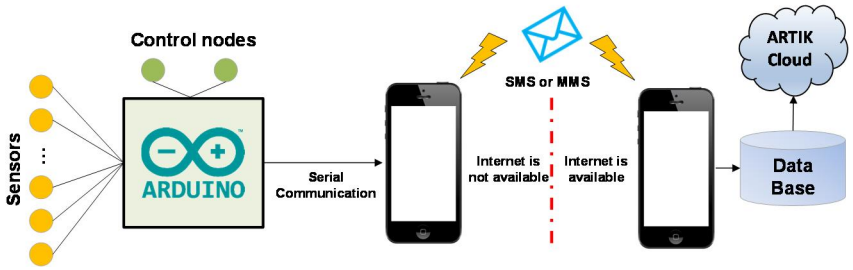

Figure 82. Schematic of a real-time online energy monitoring system

Requirements for an off-grid energy monitoring platform

In rural areas, the internet is commonly not available so SMS or MMS is used as the telecommunication method. SMS has a

short data length per message. However, a wide communication range is possible and once communication capabilities are confirmed, bi-directional communication is possible.

Sensor nodes can be fabricated at low cost. Sensors for an off-grid system should be compact and rigid even under harsh environmental conditions. Commercially available sensors are rigid and accurate but often too expensive to install in rural areas in developing countries. If sensor breakdown occurs, the cost of maintenance can increase dramatically.

The core processor also requires high stability at low cost. Arduino is a strong candidate; however, any type of embedded system could be implemented. A customized Real-Time OS (RTOS) can be implemented to accurately control sensor nodes and the data transmission interval.

Finally, several application capabilities are necessary for the end-user. Thus, Web DB and a cloud service were connected to the monitoring platform. As one example, ARTIK Cloud was used to monitor an off-grid system on a web page.

Off-grid monitoring platform

To achieve a stable data acquisition procedure even with low-performance hardware, an off-grid monitoring platform was proposed (Figure 82). There were three layers: the first was the hardware layer, the second was the telecommunication layer, and the third was the data analysis layer.

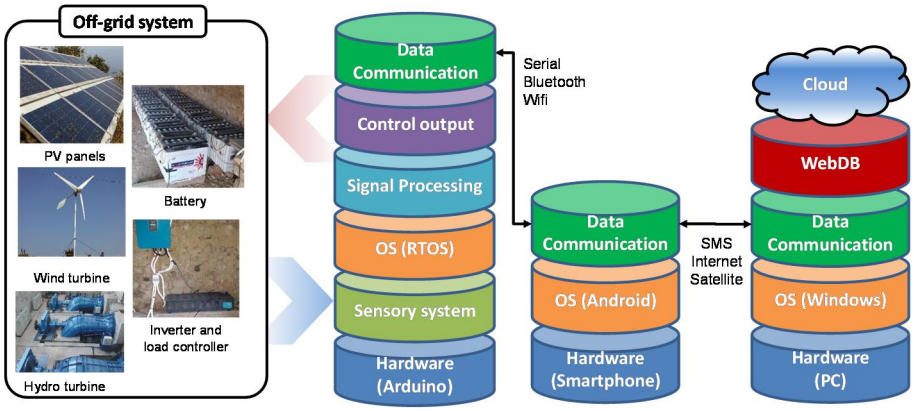

Figure 83. Schematic of an off-grid monitoring platform

In the first layer of the off-grid monitoring platform, sensors are directly or indirectly connected to the off-grid system where they measure the climate and the operating conditions of the target system. Then, a filtered data set was merged and zipped into a pre-defined form within 160 bytes to send the message via SMS. Merged characters were sent to the

second layer, ready to transmit.

At the second layer, merged characters were sent via SMS. The main purpose of this step is to check the form of the data from the first layer and if the data set is confirmed, add actual time after the merged characters and send it to the destination point, the third layer.

At the third layer, incoming data were checked and stored in several ways, such as Web DB with MySQL and ARTIK Cloud service. In this research, Web DB and Cloud were the main data storage method although any type of interface could be added at the third layer.

Hardware design for off-grid monitoring platform

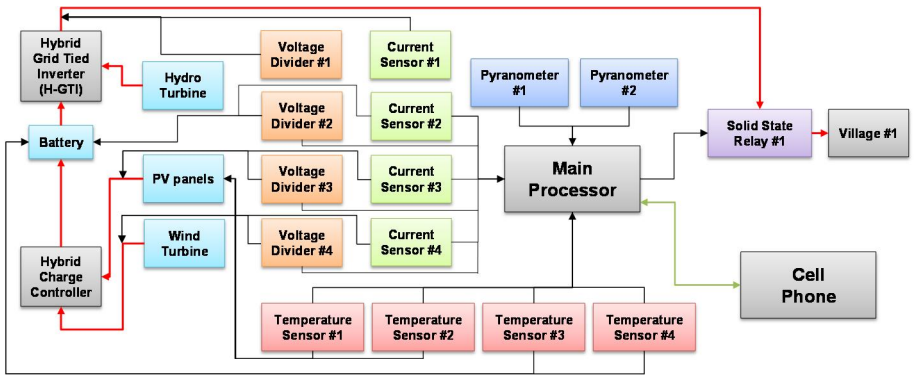

Figure 84. Hardware schematics of the off-grid monitoring platform

Main processor

The main processor of the monitoring system was Arduino Mega. Arduino Mega is equipped with 10 bits, 16 channels of ADC, and tens of digital I/Os. The processor was equipped with serial communications and an internal timer and interrupt.

Sensors

To sense solar irradiation, a customized pyranometer was fabricated and tested. SP-215 (Apogee Corp.) was used for calibrating the sensor signal. The zenith angle is crucial for calculating incident radiation from the sun so a sensor cap was fabricated. A Teflon disk 2 mm thick was fabricated and used to cover the top of the sensor cap (Figure 85). A PDB-C139 photodiode was used. Results of the calibrated sensor are shown in Figure 86.

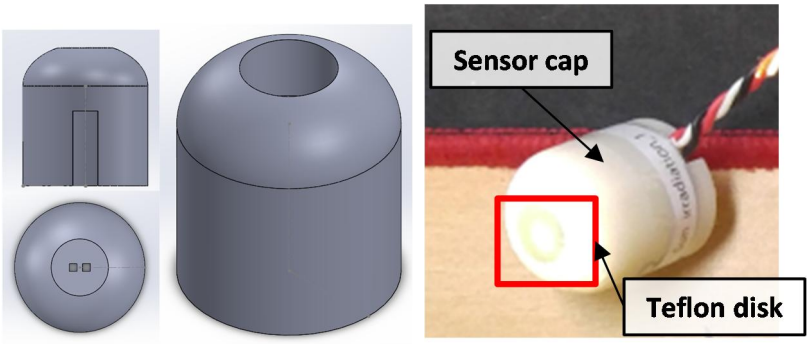

Figure 85. Customized pyranometer

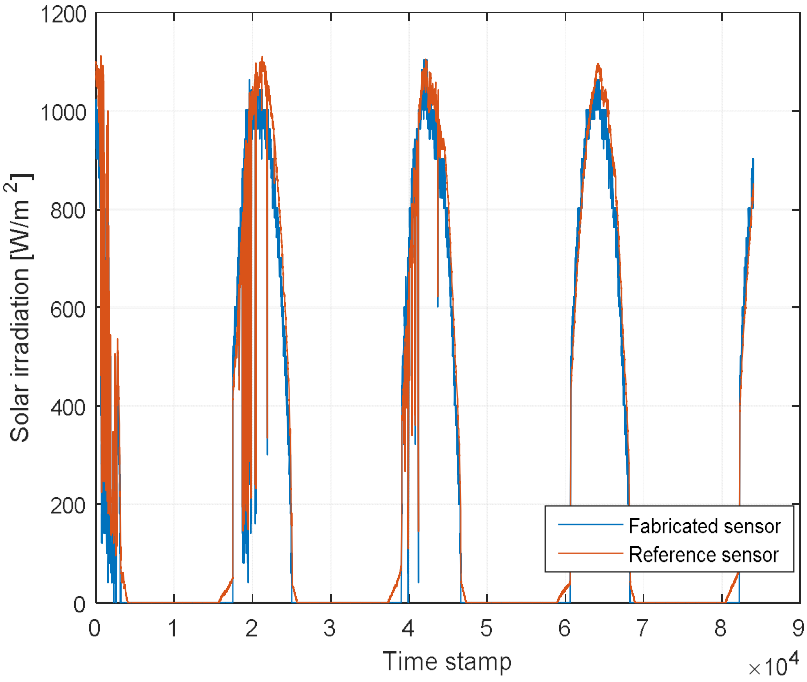

Figure 86. Calibration results with the customized pyranometer

The temperature sensor was a TC1047AVNB (Microchip Technology Inc.), which has temperature range of - 40 to 125℃ with a high linear signal (Figure 87) [104].

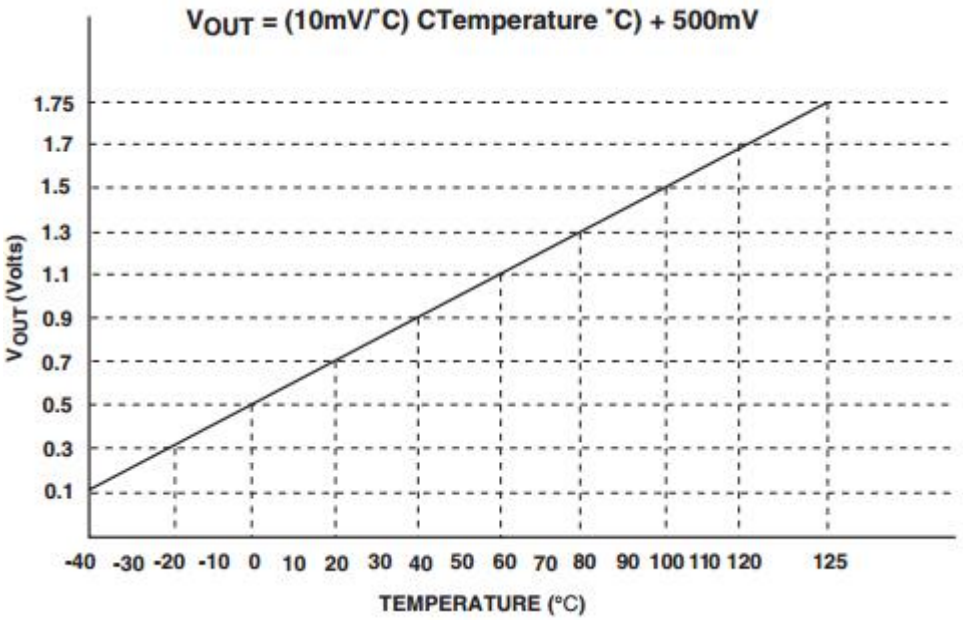

Figure 87. Output curve of the temperature sensor [104]

A Hall effect-based ring-type current sensor (WCS1x00 series) was used to monitor current flow in the off-grid energy system. The Hall effect-based sensor has high linearity (Figure 88) [105].

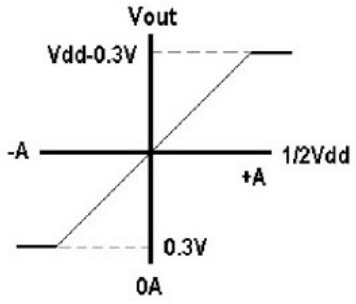

Figure 88. Output curve of Hall effect-based current sensor [105]

Telecommunication device

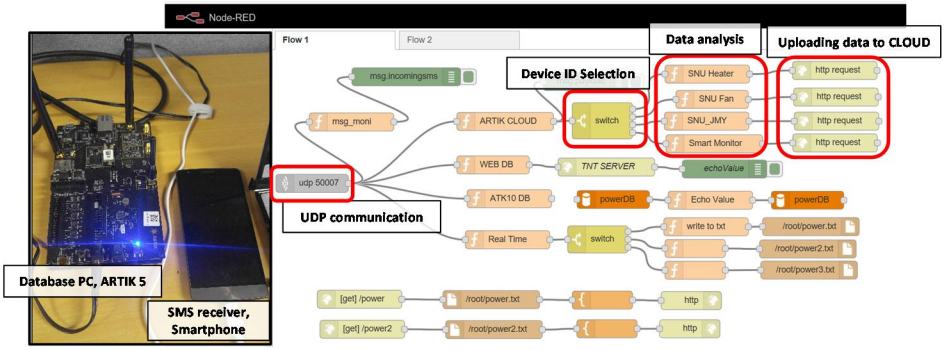

Figure 89. Database PC and backend data storage program in the database layer

Incoming data was stored in a PC database, the ARTIK 5 platform, and an external Web DB. ARTIK 5 can gather data sets from several devices. As device ID is defined in the transmitted data set, ARTIK 5 obtains the device ID and sends data to the destination ARTIK Cloud. Control software was coded by Node-RED, installed in Linux.

Software design for off-grid monitoring platform

To achieve accurate data acquisition and signal processing of target signals, a customized RTOS was implemented. The task of the monitoring device was monitored at the end of processing so that extra resources could be estimated and additional functions added. Furthermore, an interrupt was implemented to catch control signals far from an off-grid power plant.

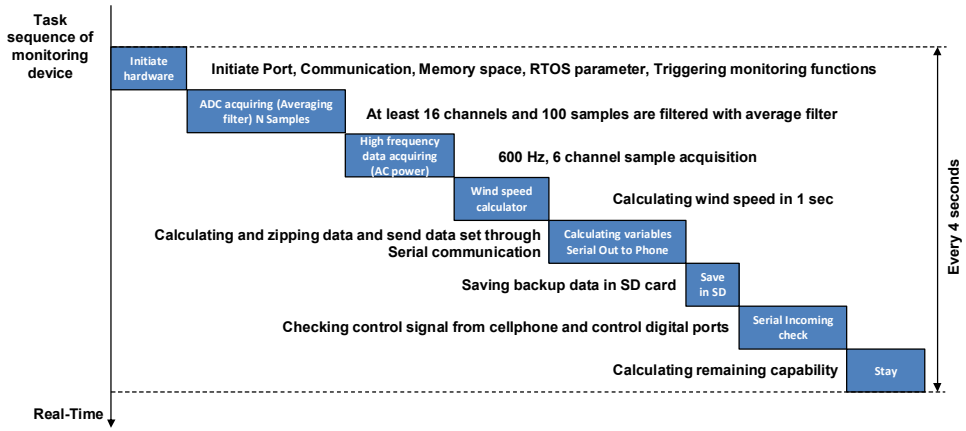

Figure 90. Hardware schematic of the off-grid monitoring platform

Customized real-time OS

A customized real-time OS is essential for accurate data acquisition and operating stability. Because of the importance of

the timing of data acquisition, each cycle of tasks is controlled by an internal timer. When the internal timer reaches predefined counts, a timer interrupt routine is loaded.

Task management

The remaining tasks of the monitoring device were measured with an internal timer. Calculation of the remaining tasks is important if adding more functions or widening the filter width or weights.

Signal Processing

A digital filter was implemented in the monitoring system. To minimize the task load of the monitoring system, a one dimensional digital filter was implemented. Window width and target data length could be adjusted. A discrete average filter can be expressed as follows:

$$d' = \mathrm{E}[D] = d_1 p_1 + d_2 p_2 + \cdots + d_n p_n$$

$$p_1 = p_2 = \cdots = p_n, \ \sum p_n = 1$$

$$d' = \sum \frac{d_n}{n}$$

where D is the set of data, d_n is the n^{th} single data point of D, d' are filtered data, p_n is the probability of each data point d_n as the weight of the discrete filter, and n is the length of the data as the window width of the digital filter.

There are two different signal acquisition procedures. The first is low-speed data measurement for DC signals and the other is high-speed data measurement for AC signals.

Low-speed data measurement

The low-speed data measurement procedure is suitable for temperature, DC voltage, DC current, solar irradiation, and any type of DC signal. The low-speed data measurement procedure acquires a data set with user-defined width and then a digital filter was applied to reduce external noise.

High-speed data measurement

The high-speed data measurement procedure is suitable for AC voltage, AC current, and any type of AC signal. Because of the relatively high frequency of AC power (commonly 50/60 Hz), high-speed data measurement is at 600 Hz.

Development results

The most important function of the monitoring platform is communication, so the first prototype was sent to Nepal on January 24th. Two temperature sensors and two current sensors were provided in the first version. Nepal Telecom provided telecommunication services for transmitting SMS. Figure 91 and Figure 92 show the installation results and incoming SMSs from Nepal.

Figure 91. First test set up for data transmitting from Nepal to South Korea

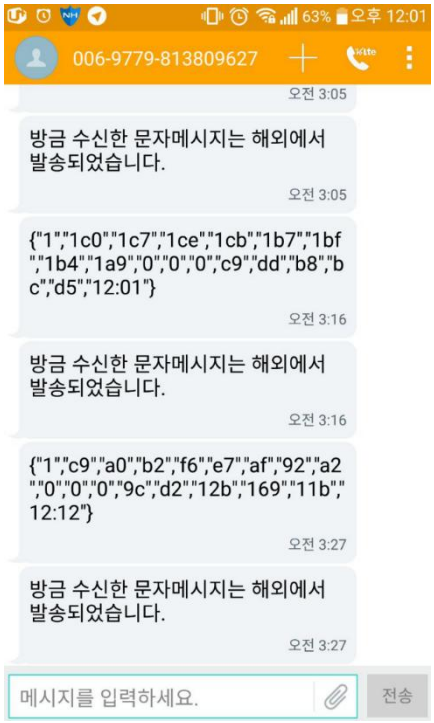

Figure 92. Results of SMS data transmission from Nepal

Figure 93. Images of sensor installation in Thingan, Nepal

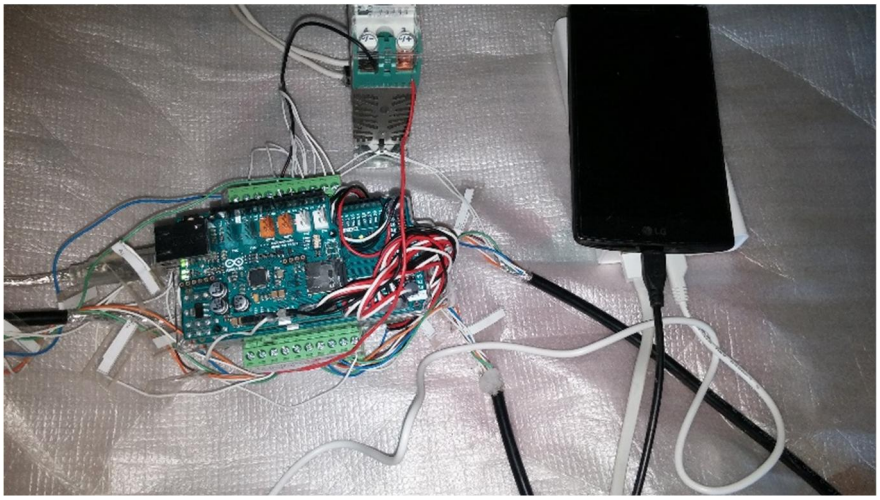

Figure 94. Monitoring device for off−grid power system in Thingan, Nepal

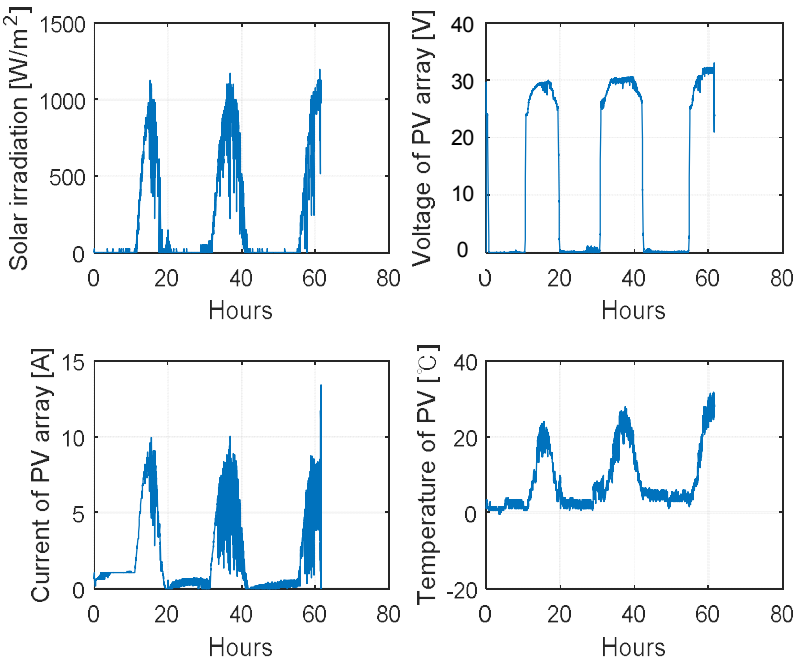

Figure 95. Sensor data from Thingan on February 4- 6th

Development summary

For two sets of tests, the off-grid monitoring platform from Nepal to South Korea was used. An off-grid monitoring system was developed and applied to a renewable system in Thingan, Nepal. Climate data and power data were acquired successfully and data sets were transmitted via SMS. Controllability of the monitoring platform was confirmed. A control signal was sent from South Korea to Nepal via SMS and the monitoring platform control SSR to turn on/off the load current.

6 Bibliography

[1] "GISTEMP Team, 2017: GISS Surface Temperature Analysis (GISTEMP). NASA Goddard Institute for Space Studies. Dataset accessed 2017-04-18 at https://data.giss.nasa.gov/gistemp/.".

[2] ""TRENDS IN GLOBAL CO2 EMISSIONS", 2016 Report, PBL Netherlands Enbiromental Assessment Agency, European Commission Joint Research Centre.."

[3] "ISO 50001:2011 – Energy Management System, Internation Organization for Standardization."

[4] *ISO 14955-1 Environmental evaluation of machine tools-Part 1: Energy-saving design methodology for machine tools*, 2014.

[5] "Global Climate & Energy Project, Stanford University Scalable and Flat Controls for Reliable Power Grid Operation with High Renewable Penetration, GCEP, Stanford University, 2010."

[6] K. E. Agency, "2015 Korea Energy Handbook," 2015.

[7] "The world data bank, Renewable energy consumption (% of total final energy consumption), 1990-2012."

[8] O. Mielnik and J. Goldemberg, "Foreign direct investment and decoupling between energy and gross domestic product in developing countries," *Energy policy,* vol. 30, no. 2, pp. 87-89, 2002.

[9] B. Bhandari *et al.*, "Socio-economic impact of renewable energy-based power system in mountainous villages of Nepal," *International Journal of Precision Engineering and Manufacturing-Green Technology,* vol. 4, no. 1, pp. 37-44, 2017.

[10] B. Bhandari, K.-T. Lee, C. S. Lee, C.-K. Song, R. K. Maskey, and S.-H. Ahn, "A novel off-grid hybrid power system comprised of solar photovoltaic, wind, and hydro energy sources," *Applied Energy,* vol. 133, pp. 236-242, 2014.

[11] "Climate data, National Climate Data Service System, Korea Meteorological Administration."

[12] "Climate dataset acquired by Korea Meteorological Administration, period : 1. 1. 2016 ~ 2.13. 2016, **California continues to set daily records for utility scale solar energy, JUNE 25, 2014."

[13] R. Khalilpour and A. Vassallo, "Planning and operation scheduling of PV-battery systems: A novel methodology," *Renewable and Sustainable Energy Reviews,* vol. 53, pp. 194-208, 2016.

[14] P. Lilienthal, P. Gilman, and T. Lambert, *HOMER® micropower optimization model*. United States. Department of Energy, 2005.
[15] S. Lal and A. Raturi, "Techno-economic analysis of a hybrid mini-grid system for Fiji islands," *International Journal of Energy and Environmental Engineering,* vol. 3, no. 1, pp. 1-10, 2012.
[16] C. Li *et al.*, "Techno-economic feasibility study of autonomous hybrid wind/PV/battery power system for a household in Urumqi, China," *Energy,* vol. 55, pp. 263-272, 2013.
[17] D. Connolly, H. Lund, B. V. Mathiesen, and M. Leahy, "A review of computer tools for analysing the integration of renewable energy into various energy systems," *Applied Energy,* vol. 87, no. 4, pp. 1059-1082, 2010.
[18] S. K. Nandi and H. R. Ghosh, "A wind–PV-battery hybrid power system at Sitakunda in Bangladesh," *Energy Policy,* vol. 37, no. 9, pp. 3659-3664, 2009.
[19] E. Tzen, K. Perrakis, and P. Baltas, "Design of a stand alone PV-desalination system for rural areas," *Desalination,* vol. 119, no. 1, pp. 327-333, 1998.
[20] A. Benatiallah, R. Mostefaou, and K. Bradja, "Performance of photovoltaic solar system in Algeria," *Desalination,* vol. 209, no. 1, pp. 39-42, 2007.
[21] J. Sachs and O. Sawodny, "A two-stage model predictive control strategy for economic diesel-pv-battery island microgrid operation in rural areas," *IEEE Transactions on Sustainable Energy,* vol. 7, no. 3, pp. 903-913, 2016.
[22] L. An and D. D.-C. Lu, "Design of a single-switch DC/DC converter for a PV-battery-powered pump system with PFM+ PWM control," *IEEE Transactions on Industrial Electronics,* vol. 62, no. 2, pp. 910-921, 2015.
[23] T. Ma, H. Yang, and L. Lu, "A feasibility study of a stand-alone hybrid solar–wind–battery system for a remote island," *Applied Energy,* vol. 121, pp. 149-158, 2014.
[24] S. Silva, M. Severino, and M. De Oliveira, "A stand-alone hybrid photovoltaic, fuel cell and battery system: a case study of Tocantins, Brazil," *Renewable energy,* vol. 57, pp. 384-389, 2013.
[25] M. Glavin, P. K. Chan, S. Armstrong, and W. Hurley, "A stand-alone photovoltaic supercapacitor battery hybrid energy storage system," in *Power Electronics and Motion Control Conference, 2008. EPE-PEMC 2008. 13th*, 2008, pp. 1688-1695: IEEE.
[26] B. S. Borowy and Z. M. Salameh, "Methodology for optimally sizing the combination of a battery bank and PV array in a

wind/PV hybrid system," *IEEE Transactions on energy conversion,* vol. 11, no. 2, pp. 367-375, 1996.
[27] T. Hiyama, S. Kouzuma, and T. Imakubo, "Identification of optimal operating point of PV modules using neural network for real time maximum power tracking control," *IEEE Transactions on Energy Conversion,* vol. 10, no. 2, pp. 360-367, 1995.
[28] A. Mellit, M. Benghanem, and S. A. Kalogirou, "Modeling and simulation of a stand-alone photovoltaic system using an adaptive artificial neural network: Proposition for a new sizing procedure," *Renewable energy,* vol. 32, no. 2, pp. 285-313, 2007.
[29] A. Mellit and A. M. Pavan, "A 24-h forecast of solar irradiance using artificial neural network: Application for performance prediction of a grid-connected PV plant at Trieste, Italy," *Solar Energy,* vol. 84, no. 5, pp. 807-821, 2010.
[30] M. G. Villalva, J. R. Gazoli, and E. Ruppert Filho, "Comprehensive approach to modeling and simulation of photovoltaic arrays," *IEEE Transactions on power electronics,* vol. 24, no. 5, pp. 1198-1208, 2009.
[31] Z. Salam, K. Ishaque, and H. Taheri, "An improved two-diode photovoltaic (PV) model for PV system," in *Power Electronics, Drives and Energy Systems (PEDES) & 2010 Power India, 2010 Joint International Conference on*, 2010, pp. 1-5: IEEE.
[32] F. Kanellos, A. I. Tsouchnikas, and N. Hatziargyriou, "Micro-grid simulation during grid-connected and islanded modes of operation," in *International Conference on Power Systems Transients*, 2005, vol. 6.
[33] W. Yang, P. J. Tavner, C. J. Crabtree, and M. Wilkinson, "Cost-effective condition monitoring for wind turbines," *IEEE Transactions on industrial electronics,* vol. 57, no. 1, pp. 263-271, 2010.
[34] M. Kalantar, "Dynamic behavior of a stand-alone hybrid power generation system of wind turbine, microturbine, solar array and battery storage," *Applied energy,* vol. 87, no. 10, pp. 3051-3064, 2010.
[35] N. W. Miller, J. J. Sanchez-Gasca, W. W. Price, and R. W. Delmerico, "Dynamic modeling of GE 1.5 and 3.6 MW wind turbine-generators for stability simulations," in *Power Engineering Society General Meeting, 2003, IEEE*, 2003, vol. 3, pp. 1977-1983: IEEE.
[36] Y. Lei, A. Mullane, G. Lightbody, and R. Yacamini, "Modeling of the wind turbine with a doubly fed induction generator for grid integration studies," *IEEE transactions on energy conversion,* vol. 21, no. 1, pp. 257-264, 2006.
[37] C. Eisenhut, F. Krug, C. Schram, and B. Klockl, "Wind-turbine model for system simulations near cut-in wind speed," *IEEE*

Transactions on Energy Conversion, vol. 22, no. 2, pp. 414–420, 2007.

[38] S. Samanvorakij and P. Kumkratug, "Modeling and simulation PMSG based on wind energy conversion system in MATLAB/SIMULINK," in *Proc. of the Second Intl. Conf. on Advances in Electronics and Electrical Engineering—AEEE*, 2013.

[39] L. Lu, H. Yang, and J. Burnett, "Investigation on wind power potential on Hong Kong islands—an analysis of wind power and wind turbine characteristics," *Renewable Energy,* vol. 27, no. 1, pp. 1–12, 2002.

[40] "Performance chart of FA 400W wind turbine, 2009, Nanjing Oulu Electric Transmission Co., Ltd."

[41] M. Dürr, A. Cruden, S. Gair, and J. McDonald, "Dynamic model of a lead acid battery for use in a domestic fuel cell system," *Journal of power Sources,* vol. 161, no. 2, pp. 1400–1411, 2006.

[42] M. A. Casacca and Z. M. Salameh, "Determination of lead–acid battery capacity via mathematical modeling techniques," *IEEE Transactions on Energy Conversion,* vol. 7, no. 3, pp. 442–446, 1992.

[43] M. Ceraolo, "New dynamical models of lead–acid batteries," *IEEE transactions on Power Systems,* vol. 15, no. 4, pp. 1184–1190, 2000.

[44] M. Chen and G. A. Rincon–Mora, "Accurate electrical battery model capable of predicting runtime and IV performance," *IEEE transactions on energy conversion,* vol. 21, no. 2, pp. 504–511, 2006.

[45] R. A. Jackey, "A simple, effective lead–acid battery modeling process for electrical system component selection," SAE Technical Paper0148–7191, 2007.

[46] N. Moubayed, J. Kouta, A. El–Ali, H. Dernayka, and R. Outbib, "Parameter identification of the lead–acid battery model," in *Photovoltaic Specialists Conference, 2008. PVSC'08. 33rd IEEE*, 2008, pp. 1–6: IEEE.

[47] S. Anderberg, S. Kara, and T. Beno, "Impact of energy efficiency on computer numerically controlled machining," *Proceedings of the Institution of Mechanical Engineers, Part B: Journal of Engineering Manufacture,* vol. 224, no. 4, pp. 531–541, 2010.

[48] D. A. Dornfeld, "Moving towards green and sustainable manufacturing," *International Journal of Precision Engineering and Manufacturing–Green Technology,* vol. 1, no. 1, pp. 63–66, 2014.

[49] S. Kara and W. Li, "Unit process energy consumption models for material removal processes," *CIRP Annals-Manufacturing Technology,* vol. 60, no. 1, pp. 37-40, 2011.
[50] H.-S. Yoon, J.-Y. Lee, M.-S. Kim, and S.-H. Ahn, "Empirical power-consumption model for material removal in three-axis milling," *Journal of Cleaner Production,* 2014.
[51] T. Gutowski, J. Dahmus, and A. Thiriez, "Electrical energy requirements for manufacturing processes," in *13th CIRP international conference on life cycle engineering*, 2006, vol. 31.
[52] N. Weinert, S. Chiotellis, and G. Seliger, "Methodology for planning and operating energy-efficient production systems," *CIRP Annals-Manufacturing Technology,* vol. 60, no. 1, pp. 41-44, 2011.
[53] A. Dietmair and A. Verl, "Energy consumption forecasting and optimisation for tool machines," *Energy,* vol. 62, p. 63, 2009.
[54] M. Xu, R. B. Jerard, and B. K. Fussell, "Energy based cutting force model calibration for milling," *Computer-Aided Design and Applications,* vol. 4, no. 1-4, pp. 341-351, 2007.
[55] W. Lee, C.-Y. Lee, and B.-K. Min, "Simulation-based energy usage profiling of machine tool at the component level," *International Journal of Precision Engineering and Manufacturing-Green Technology,* vol. 1, no. 3, pp. 183-189, 2014.
[56] H.-S. Yoon *et al.*, "A comparison of energy consumption in bulk forming, subtractive, and additive processes: Review and case study," *International Journal of Precision Engineering and Manufacturing-Green Technology,* vol. 1, no. 3, pp. 261-279, 2014.
[57] *Machine Tools—Test Methods for Electric Power Consumption–Part 1: Machining Centres*, 2010.
[58] T. Behrendt, A. Zein, and S. Min, "Development of an energy consumption monitoring procedure for machine tools," *CIRP Annals-Manufacturing Technology,* vol. 61, no. 1, pp. 43-46, 2012.
[59] R. Pawade, H. A. Sonawane, and S. S. Joshi, "An analytical model to predict specific shear energy in high-speed turning of Inconel 718," *International Journal of Machine Tools and Manufacture,* vol. 49, no. 12, pp. 979-990, 2009.
[60] V. P. Astakhov and X. Xiao, "A methodology for practical cutting force evaluation based on the energy spent in the cutting system," *Machining Science and Technology,* vol. 12, no. 3, pp. 325-347, 2008.
[61] P. Mativenga and M. Rajemi, "Calculation of optimum cutting parameters based on minimum energy footprint," *CIRP*

Annals-Manufacturing Technology, vol. 60, no. 1, pp. 149-152, 2011.
[62] N. Diaz, K. Ninomiya, J. Noble, and D. Dornfeld, "Environmental impact characterization of milling and implications for potential energy savings in industry," *Procedia CIRP,* vol. 1, pp. 518-523, 2012.
[63] M. Engin, "Sizing and simulation of PV-wind hybrid power system," *International Journal of Photoenergy,* vol. 2013, 2013.
[64] L. Zhou, J. Li, F. Li, Q. Meng, J. Li, and X. Xu, "Energy consumption model and energy efficiency of machine tools: a comprehensive literature review," *Journal of Cleaner Production,* vol. 112, pp. 3721-3734, 2016.
[65] J.-Y. Lee *et al.*, "A simplified machine-tool power-consumption measurement procedure and methodology for estimating total energy consumption," *Journal of Manufacturing Science and Engineering,* vol. 138, no. 5, p. 051004, 2016.
[66] W. Li and S. Kara, "An empirical model for predicting energy consumption of manufacturing processes: a case of turning process," *Proceedings of the Institution of Mechanical Engineers, Part B: Journal of Engineering Manufacture,* vol. 225, no. 9, pp. 1636-1646, 2011.
[67] O. I. Avram and P. Xirouchakis, "Evaluating the use phase energy requirements of a machine tool system," *Journal of Cleaner Production,* vol. 19, no. 6, pp. 699-711, 2011.
[68] L. Qian and M. R. Hossan, "Effect on cutting force in turning hardened tool steels with cubic boron nitride inserts," *Journal of Materials Processing Technology,* vol. 191, no. 1, pp. 274-278, 2007.
[69] A. Aramcharoen and P. T. Mativenga, "Critical factors in energy demand modelling for CNC milling and impact of toolpath strategy," *Journal of Cleaner Production,* vol. 78, pp. 63-74, 2014.
[70] M. T. Hagan, H. B. Demuth, and M. H. Beale, "Neural network design, PWS Pub," *Co., Boston,* vol. 3632, 1996.
[71] O. Adeoti, B. Oyewole, and T. Adegboyega, "Solar photovoltaic-based home electrification system for rural development in Nigeria: domestic load assessment," *Renewable energy,* vol. 24, no. 1, pp. 155-161, 2001.
[72] S. Shaahid and M. Elhadidy, "Economic analysis of hybrid photovoltaic–diesel–battery power systems for residential loads in hot regions—A step to clean future," *Renewable and Sustainable Energy Reviews,* vol. 12, no. 2, pp. 488-503, 2008.
[73] M. Millinger, T. Mårlind, and E. Ahlgren, "Evaluation of Indian rural solar electrification: a case study in Chhattisgarh,"

Energy for Sustainable Development, vol. 16, no. 4, pp. 486-492, 2012.

[74] E. Sreeraj, K. Chatterjee, and S. Bandyopadhyay, "Design of isolated renewable hybrid power systems," *Solar Energy,* vol. 84, no. 7, pp. 1124-1136, 2010.

[75] G. Bekele and G. Boneya, "Design of a photovoltaic-wind hybrid power generation system for Ethiopian remote area," *Energy Procedia,* vol. 14, pp. 1760-1765, 2012.

[76] J. G. Fantidis, D. Bandekas, C. Potolias, and N. Vordos, "The effect of the financial crisis on electricity cost for remote consumers: case study Samothrace (Greece)," *International Journal of Renewable Energy Research (IJRER),* vol. 1, no. 4, pp. 281-289, 2012.

[77] S. Rehman, M. M. Alam, J. P. Meyer, and L. M. Al-Hadhrami, "Feasibility study of a wind–pv–diesel hybrid power system for a village," *Renewable Energy,* vol. 38, no. 1, pp. 258-268, 2012.

[78] A. H. Khan, M. F. Khan, and R. Mostafa, "Solar PV as an effective alternative to oil based lamp in the rural Bangladesh," in *Developments in Renewable Energy Technology (ICDRET), 2012 2nd International Conference on the*, 2012, pp. 1-4: IEEE.

[79] A. Ellegård, A. Arvidson, M. Nordström, O. S. Kalumiana, and C. Mwanza, "Rural people pay for solar: experiences from the Zambia PV-ESCO project," *Renewable energy,* vol. 29, no. 8, pp. 1251-1263, 2004.

[80] M. Moner-Girona, R. Ghanadan, A. Jacobson, and D. M. Kammen, "Decreasing PV costs in Africa: Opportunities for rural electrification using solar PV in sub-Saharan Africa," *Refocus,* vol. 7, no. 1, pp. 40-45, 2006.

[81] K. T. Lee, "Design Guide and Cost Estimation of Micro Hydro-Solar-Wind Hybrid Renewable Energy System for Off-grid Villages," *Ph.D Thesis, Seoul National University,* 2014.

[82] M. Panteli and P. Mancarella, "The grid: Stronger, bigger, smarter?: Presenting a conceptual framework of power system resilience," *IEEE Power and Energy Magazine,* vol. 13, no. 3, pp. 58-66, 2015.

[83] Y. Yan, Y. Qian, H. Sharif, and D. Tipper, "A survey on smart grid communication infrastructures: Motivations, requirements and challenges," *IEEE communications surveys & tutorials,* vol. 15, no. 1, pp. 5-20, 2013.

[84] G. Bayrak and M. Cebeci, "Monitoring a grid connected PV power generation system with labview," in *Renewable Energy Research and Applications (ICRERA), 2013 International Conference on*, 2013, pp. 562-567: IEEE.

[85] J. Aghaei and M.-I. Alizadeh, "Demand response in smart electricity grids equipped with renewable energy sources: A review," *Renewable and Sustainable Energy Reviews,* vol. 18, pp. 64-72, 2013.
[86] A. Drews *et al.*, "Monitoring and remote failure detection of grid-connected PV systems based on satellite observations," *Solar Energy,* vol. 81, no. 4, pp. 548-564, 2007.
[87] R. Teodorescu and F. Blaabjerg, "Flexible control of small wind turbines with grid failure detection operating in stand-alone and grid-connected mode," *IEEE transactions on power electronics,* vol. 19, no. 5, pp. 1323-1332, 2004.
[88] I. B. Askari and M. Ameri, "Techno-economic feasibility analysis of stand-alone renewable energy systems (PV/bat, Wind/bat and Hybrid PV/wind/bat) in Kerman, Iran," *Energy Sources, Part B: Economics, Planning, and Policy,* vol. 7, no. 1, pp. 45-60, 2012.
[89] G. Kamalapur and R. Udaykumar, "Electrification in rural areas of India and consideration of SHS," in *2010 5th International Conference on Industrial and Information Systems*, 2010, pp. 596-601: IEEE.
[90] A. Al-Karaghouli and L. Kazmerski, "Optimization and life-cycle cost of health clinic PV system for a rural area in southern Iraq using HOMER software," *Solar Energy,* vol. 84, no. 4, pp. 710-714, 2010.
[91] M. El Mnassri and A. S. Leger, "Stand alone photovoltaic solar power generation system: A case study for a remote location in Tunisia," in *IEEE PES General Meeting*, 2010, pp. 1-4: IEEE.
[92] N. Rapapate and Ö. Göl, "Use of photovoltaic systems for rural electrification in Thailand," in *Sevilla, Spain: International Conference on Renewable Energies and Power Quality*, 2007.
[93] S. Tselepis, "Electrification with solar powered mini-grids, a case study for the island of Kythnos," in *Photovoltaic Energy Conversion, 2003. Proceedings of 3rd World Conference on*, 2003, vol. 3, pp. 2314-2317: IEEE.
[94] P. Dalwadi, V. Shrinet, C. Mehta, and P. Shah, "Optimization of solar-wind hybrid system for distributed generation," in *2011 Nirma University International Conference on Engineering*, 2011, pp. 1-4: IEEE.
[95] M. Ashourian, S. Cherati, A. M. Zin, N. Niknam, A. Mokhtar, and M. Anwari, "Optimal green energy management for island resorts in Malaysia," *Renewable energy,* vol. 51, pp. 36-45, 2013.
[96] G. Panayiotou, S. Kalogirou, and S. Tassou, "Design and simulation of a PV and a PV–Wind standalone energy system to

power a household application," *Renewable Energy,* vol. 37, no. 1, pp. 355-363, 2012.
[97] H. Yang, Z. Wei, and L. Chengzhi, "Optimal design and techno-economic analysis of a hybrid solar-wind power generation system," *Applied Energy,* vol. 86, no. 2, pp. 163-169, 2009.
[98] S. K. Nandi and H. R. Ghosh, "Prospect of wind-PV-battery hybrid power system as an alternative to grid extension in Bangladesh," *Energy,* vol. 35, no. 7, pp. 3040-3047, 2010.
[99] A.-K. Daud and M. S. Ismail, "Design of isolated hybrid systems minimizing costs and pollutant emissions," *Renewable energy,* vol. 44, pp. 215-224, 2012.
[100] M. S. Ngan and C. W. Tan, "Assessment of economic viability for PV/wind/diesel hybrid energy system in southern Peninsular Malaysia," *Renewable and Sustainable Energy Reviews,* vol. 16, no. 1, pp. 634-647, 2012.
[101] G. Bekele and B. Palm, "Feasibility study for a standalone solar-wind-based hybrid energy system for application in Ethiopia," *Applied Energy,* vol. 87, no. 2, pp. 487-495, 2010.
[102] R. K. Akikur, R. Saidur, H. W. Ping, and K. R. Ullah, "Comparative study of stand-alone and hybrid solar energy systems suitable for off-grid rural electrification: a review," *Renewable and Sustainable Energy Reviews,* vol. 27, pp. 738-752, 2013.
[103] P. Thomson, R. Hope, and T. Foster, "GSM-enabled remote monitoring of rural handpumps: a proof-of-concept study," *Journal of Hydroinformatics,* vol. 14, no. 4, pp. 829-839, 2012.
[104] "Datasheet of TC1047/TC1047A, Percision Temperature-To-Voltage Converter, 2002, Microchip Technology Inc.."
[105] "Datasheet of Hall Effect Base Linear Current Sensor, 2010, Winson Corp.."

7 Abstract in Korean

Off-grid 신재생 에너지를 원격지에서 모니터링 및 제어할 수 있는 모니터링 플랫폼을 제작하였다. 제안된 플랫폼은 소형, 저가의 모니터링 장비에도 손쉽게 적용 가능하도록 자체 제작한 RTOS (Real-time Operating System)를 탑재하여 기본적인 Task management 기능을 수행한다. 개발된 플랫폼은 다양한 형태의 Off-grid System에 적용 가능하며, 인터넷이 불가능한 환경에서도 원격지에서 모니터링 가능하도록 SMS (Short Message Service)를 사용하여 데이터 수집 및 모니터링을 수행하였다. 또한 수집된 데이터를 Cloud에 DB로 구축하여 인터넷 환경에서 모니터링 가능하도록 모니터링 플랫폼을 구성하였다.

또한 모니터링 시스템으로부터 취득된 데이터를 기반으로 제조공정에 초점을 맞춘 Off-grid system의 모델링을 수행하였으며, 실제 Off-grid에서의 에너지 생산, 소비 패턴을 테스트 베드를 구축하여 실험을 통해 모델 검증을 수행하였다. 모델링 수행에 필요한 PV, Wind turbine, Battery 그리고 Manufacturing process 모델을 구축하였으며, 모델을 통합하여 Manufacturing system을 안정적으로 운영하기 위한 Off-grid renewable energy system의 규모에 따른 failure rate을 계산하였다.

구축된 모델링 결과를 검증하기 위해 본 연구에서 개발한 Monitoring platform을 사용하여 실제 off-grid 시스템을 모니터링 하였으며, 3D 프린터, 대형 선반, 밴드 톱 그리고 백신케리어 총 4가지 경우에 대한 실험을 수행하였다. 다양한 실험 결과로부터 제안된 모델을 활용하여 Off-grid 신재생 에너지 발전소의 안전성을 확인하였으며, 기존에 사용되던 통계모델 대비 동일한 안정성을 유지하면서 더 작은 규모의 신재생에너지 발전시스템 설계를 도출해 냈다.